SPREADING OF INITIALLY SPHERICAL VISCOUS DROPLETS

by

Sivaramakrishna Kotikalapudi

A Thesis

Submitted to the Faculty

of the

WORCESTER POLYTECHNIC INSTITUTE

in partial fulfillment of the requirements for the

Degree of Master of Science

in

Mechanical Engineering

by

August 2000

APPROVED:

Professor James C. Hermanson, Thesis Advisor

Professor Andreas N. Alexandrou, Thesis Co-Advisor

Professor David J. Olinger, Committee Member

Professor Mark W. Richman, Graduate Committee Representative

Abstract

The present work is a study of the low inertia spreading dynamics of initially spherical viscous droplets on a planar interface. The droplets are affected by gravity, surface tension and viscous forces and are modeled as two-dimensional axisymmetric bodies. The main focus of this study is the examination of the dependence of droplet stability, equilibrium shape and fluid motion within the drop on the relative magnitude of these forces. The dynamics are modeled using the unsteady, non-linear Navier-Stokes equations for an incompressible fluid. The spreading of a droplet on a solid surface is modeled with both a no-slip and a partial-slip boundary condition. In addition, the spreading of a droplet on another identical drop (two-drop problem) is modeled to study the problem without the contact point singularity. The governing equations are solved numerically using the Mixed Galerkin Finite Element formulation, augmented by the use of the Newton-Raphson iteration scheme to effectively treat the non-linearities of the problem. The Generalized Eulerian Lagrangian formulation is adopted for the treatment of the moving free surface of the droplet. Computations are performed for capillary numbers ranging from 0.01 to 100 and for Reynolds numbers from 0.005 to 50, where the velocity scale is based on the droplet radius and the gravitational acceleration. For the droplet spreading on a solid surface, three distinct behaviors are observed : for low Reynolds numbers and sufficiently high capillary numbers, droplets deform to a stable, equilibrium shape; for higher Reynolds numbers, an oscillatory droplet behavior occurs; at still higher Reynolds numbers, the droplets shatter. Very often, a recirculation is induced near the contact point just before the droplet shatters, which is also observed for the case of stable oscillating droplets. When a partial-slip boundary condition is applied, it is observed that the stability of the droplet and the rate at which the droplet attains the static contact angle depend strongly on the velocity of slip of the droplet with respect to the solid surface at the contact point. For the two-drop problem, only two distinct behaviors are observed: for low Reynolds numbers and high capillary numbers, the droplet retains a near-spherical shape and remains stable; while for higher Reynolds numbers, the droplet deforms to a high extent and becomes unstable.

Acknowledgements

I express my heartfelt gratitude and appreciation to my advisors, Professor James Hermanson and Professor Andreas Alexandrou for their constant guidance and invaluable advice throughout the course of this exciting study. I thank them for their unfailing support and phenomenal patience in helping me through difficult times and for their wisdom in challenging and encouraging me to discover new frontiers, at the most appropriate times. I will forever be indebted to them.

I would also like to express my gratitude to Professor Vladimir Entov of the Institute for Problems in Mechanics of the Russian Academy of Sciences for his time for valuable discussions that helped in a deeper understanding of the concepts involved in this work and for his generous faith in me.

I am very grateful to Professor David Olinger, both for his inspiring lectures and his willingness to serve as a member of my thesis committee. I am also grateful to Professor Mark Richman for graciously accepting to represent the Graduate Committee, inspite of a demanding schedule.

I also wish to express my appreciation to all my teachers and mentors at WPI, who have helped make my stay here a memorable and rich learning experience. I would like to acknowledge the Department of Mechanical Engineering for funding me through a Teaching Assistantship for the entire duration of my studies.

I thank all my friends at WPI for making life here a lot of fun and worth all the toil. A special thanks to Anand, Mrunal, Praveen, Ketki, Pete, Gana, Badri, Vamsi and many others who, though not mentioned here, are definitely remembered for being there and for just being themselves!

I would like to specially thank my friends Philippe and Rosti at the SSMPL, both for helping me at the oddest hours and for challenging my ability to learn new languages. I also thank Mr. Sia Najafi for helping me with the computer facilities

and for retrieving many a lost file.

I would like to thank Ms. Barbara Edilberti, Ms. Pam St. Louis, Ms. Janice Dresser and Ms. Barbara Furhman for sharing their smiles with me and helping with anything administrative.

I would like to say a very special thanks to my family on both sides of the world, for helping me realize my dreams and for welcoming me home anytime I needed warmth and comfort.

Last, but by no means the least, I thank God for getting me where I am today.

Contents

List of Figures

List of Tables

Chapter 1

Introduction

The dynamics of viscous droplets is a fundamental problem in fluid mechanics and has been the focus of intense study. This problem represents a point of convergence for many important physical phenomena and of several theoretical principles that are the foundations for modern fluid mechanics. The behavior of droplets has been investigated in several forms and under various influencing conditions, due to its profound significance in multiple engineering disciplines. For instance, the same mechanism that drastically affects aircraft in flight through the impact of liquid droplets can be used in the effective atomization of liquid propellents in rockets. Furthermore, the behavior of viscous droplets has important applications in many scientific fields such as material processing, processing of pharmaceutical products, printing, coating, near-net-shape manufacturing and atomization processes. While the study of droplet dynamics is far-ranging both in terms of phenomena and applications, a very common and fascinating study is the interaction of drops with solid surfaces, which in itself encompasses a broad range of research. The present work focusses on the latter class of problems and the variations therein.

The motion of liquid droplets on a surface constitutes a problem of considerable difficulty both in modeling and solution. In addition to the difficulty involved in the solution of a moving boundary, such as the droplet free surface, the behavior of the fluid in the vicinity of the fluid-fluid-solid interface (contact line) presents further complications. If a no-slip boundary condition is assumed at the contact line, a non-integrable force singularity appears in the Navier-Stokes equations. Moreover, experimental studies have shown that the dynamic change of the contact angle is a complex function of the contact line speed and necessiates the inclusion of a functional relationship in the analysis of the problem [1]. Several studies were made to model this relationship and have resulted in various degrees of success [2], [3]. Most of these studies were based on the inclusion of a slip velocity of the fluid at the contact point, with respect to the solid surface, with the reason that when one fluid displaces another from the solid surface, both fluids move relative to the surface, for some finite time during the process [3].

The dynamics of free surfaces between two immiscible fluids are usually controlled by surface tension, gravity, viscous forces and the inertia of the system such that the degree and the rate of spreading depends upon the relative importance of these three factors, in addition to possible heat transfer. Currently, there is a plethora of analytical [3], experimental [4] and computational studies [5] dealing with the spreading of viscous droplets, with the movement of the contact line (the fluid-fluid interface along a solid surface) being the focal point of such studies. Due to the importance of the contact line, the general spreading of liquid sublayers (the viscous liquid region between top point of the droplet and the solid surface), be it a deforming droplet on a solid surface, or a moving coat of film on a solid substrate, has become synonymous to the motion of the contact line. This equivalence is based on the established influence of the conditions at the contact line on the general stability and manner of spreading of the liquid layers on solid substrates.

1.1 Objectives and Approach

The main objective of this work is the study of the dynamics of the fluid in droplets spreading on a solid substrate and their dependence on different influencing parameters (specifically, gravity, surface tension, viscosity and droplet size) under isothermal conditions of both the fluid and the solid surface. In addition to this, the problem of two droplets spreading on each other under specific conditions is also investigated to offer a better understanding of fluid motion in the absence of any external surfaces. This study is based on the simulations achieved from a numerical analysis of the problem.

Since the droplet is identical in any plane perpendicular to the surface on which it spreads, it is modeled as a two-dimensional axisymmetric body. Moreover, in each of these planes, the droplet is symmetric about a center line through the top point. Hence, only one half of the droplet is considered in the analysis. As a tool to model the problem and efficiently investigate its sensitivity to variations in conditions, the fluid flow is represented using the conservation equations and appropriate boundary conditions to balance the physical attributes of velocity and pressure. These equations are solved numerically using a classical Finite Element Method and a suitable solver to handle the resulting algebraic equations. Since our interest is in the dynamics of motion, a transient analysis is adopted for the model and the simulations are obtained, from which the relevant inferences are drawn.

The historical background and the results of previous studies are presented in Chapter 2, while the physical model and the mathematical formulation of the problem is discussed in Chapter 3. The solution methodology that has been employed to solve this problem is discussed in Chapter 4 and the results that were obtained are presented and discussed in Chapter 5. Finally, the conclusions which can be drawn from this study and the possible advances which can be made to enhance the research are documented in Chapter 6.

Chapter 2

Literature Review

As mentioned in the previous chapter, the spreading of viscous droplets is a very fascinating and highly consequential problem which has received a great deal of attention for over a century. Many of the early studies involved attempts at analytical solutions of the governing equations in pursuit of unique mathematical expressions for velocity of the liquid inside and the shape of the droplet. These studies were succeeded by a class of investigations, both experimental and computational, into the dynamics of droplets impacting on solid surfaces. However, since in these cases the inertial forces dominate the effects of surface tension, gravity and viscosity, the contact line dynamics for slow droplet spreading was considered separately and several models were proposed. These models were valid within the range of the assumptions which were made but did not provide any form of global solution for the problem of contact line motion.

2.1 Historical Perspective

One of the earliest studies into the dynamics of droplets was conducted by Lamb in his paper on oscillating viscous "spheroids" in 1881 [6]. In this paper, he presented his theoretical analysis on the gravitational oscillations of a spherical mass of liquid based on a series solution of the Helmholtz equation describing the velocity of the fluid in the droplet. The solution for velocity was expressed as a weighted infinite sum of several solid harmonics, such that the weights satisfy certain equations. Several combinations of these weights are possible that give different possible solutions, but which belong to a finite set of solutions. All these solutions however, give a unique expression for the frequency of the oscillations of the droplet and the viscous decay rate. Lamb presented expressions for these two quantities for the extreme cases in which either gravity or surface tension were important. The influence of the contact point on the spreading dynamics, however, was not considered.

Many of the later studies were concerned with the dynamics of droplets at very high impact velocities where the inertia of the droplets obscured the viscous, gravity and surface tension effects during most of the process (Trapaga & Szekely in 1991 [7], Trapaga et. al. in 1992 [8], Westhoff et. al. in 1992 [9]). Trapaga & Szekeley [7] solved a fluid dynamic model of droplet deformation using a numerical approach to simulate the case of impacting droplets. The scheme that was employed used an equivalent pressure to replace the stress balances on the free surface. In this isothermal model, the time variation of the “splat“ radius was reported for liquid metal droplets impinging on a flat surface. The results showed the increase of the splat radius till it reached a maximum value, at which it subsequently remained, due to the assumption that fluid spreading was irreversible. Solidification was not considered in this model. Since the recoiling of the droplet from the surface was not considered, the computed maximum splat radii were larger than the expected wetting radius of the equilibrium sessile state. These calculations were, however, considered good approximations of the modeling of impacting droplets.

Soon after this study, Fukai *et al.* [10] came up with an experimental and theoretical study of the collision of droplets and their subsequent deformation. The theoretical model which they used accounted for the presence of contact-angle hysteresis in addition to the effects of inertia, gravity, surface tension and viscosity. Also, in this work the initial shape of the droplet, as it collides with the solid surface, was assumed to be spherical, unlike preceding studies. When compared to experimental results of the impingement of the droplets on a solid surface, the effects of recoiling and oscillation of the droplet were well predicted by the numerical model. In addition, the prediction of the formation of the ring structure around the splat and its height also agreed well with experimental results.

However, there is a large number of applications where the effects of gravity, surface tension and viscosity are much stronger than that of inertia. These generally constitute the low velocity spreading of liquid droplets. In these cases, the above mentioned forces themselves account for the driving and restoring action. The modeling of this class of problems is rendered difficult by the presence of the contact point singularity mentioned earlier, for which various remedial methods were proposed [2].

For instance, Hocking & Rivers [11], considered a small drop spreading on a horizontal surface, where the dynamics were affected only by surface tension and not by gravity. To avoid the force singularity that appears in the governing equations with a no-slip boundary condition, in the vicinity of the moving contact line, it was assumed that the slip is proportional to the local velocity gradient. They developed an equation that related the rate of spreading of the drop to the contact radius, for a given initial configuration, assuming a constant contact angle. The proposed theory was compared to experimental data obtained from observations of molten glass drops on a platinum plate, with appropriate control of surface wetting to avoid sticking. A sufficiently good agreement was achieved between experimental results and the theoretical predictions based on the hypotheses presented, even though the slip coefficient was not determined accurately.

A similar problem was investigated by Haley & Miksis [2] using lubrication theory to develop a model for the motion of the free surface. This model includes both the effect of slip, and the dependence of the contact angle on slip velocity. The model that was developed by Greenspan [12] was used to determine the spreading rate as a function of capillary and Bond numbers. This model was obtained by assuming that the height of the droplet is much smaller than its radius and the resulting equation was a nonlinear partial differential equation, first order in time and fourth order in space. This nonlinear partial differential equation was solved using the Chebychev collocation method. It was concluded in this paper that the proper form of the relationship needs to be determined by an analysis in the neighborhood of the contact line. Thus the modeling of the contact line is crucial to this problem.

The objective of the current work is twofold; first, to study the underlining physics of a spreading droplet under different rheological and process parameters, such that both gravity and capillary effects are important, and second, to determine the effect of the slip models on the spreading of impacting droplets under different model parameters.

Dussan & Davis [13], in what is now considered a classic paper in this area, used a continuum based model in which they proposed a contact line motion which is characterized as “rolling”. The basic assumption of the proposed motion is that fluid particles arrive or leave the contact line in a finite amount of time. This is in contrast to stagnation point flow where the fluid particles take an infinite amount of time to arrive at the stagnation point. The implication of the two different flow situations is that the stagnation point flow the velocity field is analytic whereas in the case of the rolling contact line the velocity field is multi-valued. The derivation of the contact line singularity by Dussan & Davis was independent of surface tension, surface viscosity or elasticity and other interfacial parameters and was obtained by using the conservation of mass and the no-slip boundary condition. They showed that any slip coefficient at the contact line is sufficient to remove the singularity. They also showed that the moving of the contact angle was kinematically compatible with the no-slip boundary condition.

Prior to the work of Dussan & Davis, Huh & Scriven [3] theoretically attempted to treat the singularity at the contact line by simplifying the geometry of the fluid-fluid interface as a planar surface and by assuming Stokes flow. For this flow situation they attempted to get an analytic solution for the region near the contact line. They were unable to satisfy the continuity of the stress across the interface. The resulting flow field implied an infinite force exerted on the fluid particles at the point of contact.

Following the work of Dussan & Davis most theoretical, computational and experimental studies have either verified their conclusions or have based their work on their recommendations. In general there are two fundamental issues in modeling contact problems: (a) the nature of the slip velocity, V_{slip} and (b) the dynamic contact angle θ. The most prevailing approach to relate these two quantities and the static contact angle θ_s, is a "power-law" type relation [2],

$$V_{slip} = \beta \left(\theta - \theta_s\right)^m \tag{2.1}$$

where β, and m are appropriately chosen coefficients. Under steady state and static conditions, this relation guarantees that the contact angle is equal to θ_s. Moreover, this proposed model has been verified experimentally [13]. Unfortunately, however, while the form of Eq. 2.1 seems consistent with experiment, the values of the constants are unclear. Greenspan [12] used the constitutive relation (Eq. 2.1) and lubrication theory to study the motion of small viscous droplets. In the same study he considered the effects of surface contamination on the motion and distortion of the droplets. Hocking & Rivers [11] removed the force singularity at the point of contact by introducing a slip velocity proportional to the tangential component of the shear stress. They obtained solutions for a spreading droplet using matched asymptotic solutions by considering an inner (rim) solution, an intermediate solution and an outer solution. In their study they fixed the apparent contact angle at its static value. They supported their assumptions and solutions by experiments using molten glass droplets. Haley & Miksis [2] evaluated the relative effect of various parameters in constitutive relations for the motion of the contact point and the slip velocity, on the spreading of an initially elliptic droplet. Ehrhard & Davis [14] using the "power-law" constitutive relation in Eq. 2.1 studied the non-isothermal spreading of liquid drops. They presented results both for isothermal as well non-isothermal spreading under various conditions. More recently, Hocking [15] considered the two seemingly rival approaches in handling the apparent dynamic contact angle; one that modifies the static angle according to the above relation and the other where the dynamic contact angle is fixed at its static value. He concluded that ".. some form of slip at the contact line and a static contact angle provide acceptable basis for the conditions to be imposed at the contact line".

2.2 Present Work

The above definitive studies invoked the assumptions of lubrication theory which among other simplifications neglect the effects of inertia. Many of these studies also neglect the effects of gravity. Moreover, the initial shape of the droplets under study was assumed to be elliptical, with the point of contact ahead of the bulk of the fluid. The problem we are considering here is different from the above representative studies in the following respects : (a) the droplet has an initial spherical shape with the point of contact beneath the bulk of the fluid, and therefore, influenced by the dynamics of the bulk flow and, (b) the spreading and deformation of the droplet is dominated by viscous, capillary and gravity forces. Under such conditions the apparent motion of the point of contact is more complex than the spreading dominated by capillary forces alone. During the early stages of deformation, the point of contact is affected by the growing "inner" shear sublayer and the "outer" mostly potential downward gravity-driven flow of the bulk flow. At the later stages of deformation, the influence of the outer flow diminishes while the capillary and shear effects become more important. Therefore, under these conditions, it is unlikely that a single set of parameters β and m will be sufficient to describe the whole range of deformation. Nevertheless, in the absence of more definitive theories for this flow situation, in this work we will rely upon the theoretical and experimental work of the previous investigators and we will again assume that the contact point has a finite slip velocity described by the same "power law" model proposed by most of the previous studies. Additionally though, we will assume that the free surface undergoes a rolling motion thus allowing particles on the free surface to come in contact with the solid surface (similar to the assumptions made by Dussan & Davis [13]). Under these assumptions the apparent motion of the point of contact (which in reality is not always the same material point) is due to the combined effect of slipping and rolling. Due to the initial geometry of the droplet it is unlikely that during the entire spreading process the contact angle remains equal to the static conduct angle. Therefore, we are not considering Hocking's proposed approach, although at the microscopic level his postulate may be true for this problem as well.

Chapter 3

Problem Formulation

3.1 Physical Model

A liquid droplet, when gently released onto a plane solid surface, spreads under the action of gravity as the free surface advances into contact with the solid. The dynamics of this phenomenon are affected by the properties of the liquid in the droplet, those of the ambient fluid and the surface properties of the solid. The spreading is characterized by the movement of the contact point due to the progressive increase in the contact area and the nature of the relation between the liquid and the solid surface at this point is crucial for this problem.

A consideration of this relation leads to two distinct possibilities; one, with a continuous liquid-liquid interface, across which there is no change in fluid properties and the other, a liquid-solid interface across which the both physical state and the material itself differ. In the former case, all points on the contact line move with the bulk of the liquid, while in the latter, only the contact point advances. These cases simulate, respectively, the spreading of a liquid droplet for : (a) liquid droplet spreading after the impact of two identical droplets and (b) liquid droplet spreading on a solid substrate. The first case represents a physically hypothetical situation in which gravity acts towards the contact line for *both* droplets (Fig. 3.1(a)). As mentioned earlier, this case helps study the problem of droplet spreading while eliminating the contact point singularity. The second case, however, represents the more realistic case of a droplet spreading on a plane solid surface (Fig. 3.1(b)). In the latter case, the spreading is further affected by the nature of motion of the contact point relative to the surface, which is quantified in terms of a slip coefficient, β. The effect of this slip coefficient is discussed in greater detail in Chapters 4 and 5.

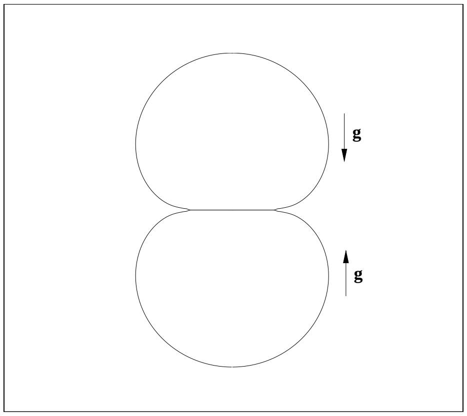

(a)

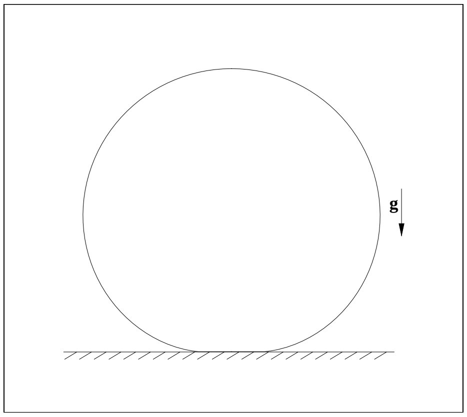

(b)

Figure 3.1: Cases of droplet spreading : (a) mutual spreading of two droplets (b) spreading of a droplet onto a plane solid surface.

3.2 Mathematical Formulation

A mathematical model was formulated for the two cases of droplet spreading described above. The simulations were initiated at the instant when the droplet was released onto the surface (of another droplet or of a plane solid, as the case may be) and were carried out until the droplet came to rest, attained steady state, or became unstable (either physically or numerically). At all times during the simulation, the general conservation laws of fluid dynamics apply to the fluid within the droplet.

In general, any problem involving fluid flow can be described using one of two approaches, viz. Eulerian and Lagrangian, which differ in the focus of their reference frames. The Eulerian approach is based on a reference frame fixed at a point in space, while the Lagrangian approach is based on a reference frame that moves with a given fluid element. When using a computational Eulerian approach, the values of fluid properties are determined at fixed grid points of a given mesh. The advantage of such a description is the ability of retaining accuracy even as the free surface of the droplet undergoes large distortions. However, when using a finite element analysis as a solution tool, this description requires the generation of new finite element discretizations as the fluid surface deforms and, good resolution is difficult to achieve. When using a Lagrangian approach, fluid properties are determined only for a finite number of particles that characterize the movement the fluid. This approach has the advantages of the accurate modeling of *small* free surface motion and easy modification for multimaterial flow (not relevant to the current problem) and the inclusion of surface tension effects. However, with this description, the accuracy can break down at large free surface distortions.

Thus, to accurately simulate the motion of the deforming free surface, the Generalized Eulerian Lagrangian (GEL) formulation was adopted [29] & [30], in which a reference frame was introduced, which is neither constrained to move with the material velocity (Lagrangian) nor required to remain stationary (Eulerian) at all times. The GEL formulation includes the pure Lagrangian and Eulerian descriptions as limiting cases. The process is implemented in two phases by combining both of these computing approaches. The first phase is that of a Lagrangian computation, which involves the hydrodynamic time-dependent calculations to model the dynamic deformation of the free surface. And the second phase is that of an Eulerian computation, in which remeshing takes place, as prescribed by the velocity of the reference frame in order to prevent large distortions in the fluid domain. In the latter phase, no time change occurs of the velocities associated with the fluid, while the convective flux calculations are performed to be consistent with the fluid motion. These two phases are repeated in tandem for the required period of time. An appropriate choice of the velocity of the reference system can exploit the advantages of both these descriptions (as described above).

This method has been used in a number of different problems as discussed by Ramaswamy [29], and Alexandrou & Ahmed [30]. The following is the derivation of the transformation of the governing laws to GEL coordinates.

3.2.1 General Approach for the GEL formulation

Let us consider an arbitrary moving control volume, V_c. At time $t = 0$, the control volume V_c coincides with a system of material particles with constant mass. Applying the conservation law of an arbitrary function f_s we can write,

$$\frac{D}{Dt}\int_{V_c} f_s \, dV_c = \int_{V_c} q_s \, dV_c, \tag{3.1}$$

where $\dfrac{D}{Dt}$ represents the material (Lagrangian) derivative and the right hand side term, q_s of the conservation equation corresponds to the net influx of the conserved quantity, f_s. For instance, when $q_s = 0$ and f_s is the mass density, we obtain the law of conservation of mass. If the boundary of the control volume is now allowed to move and deform with arbitrary velocity $\mathbf{W}$, at any time t, Eq. 3.1 can be expressed as

$$\frac{d}{dt}\int_{V_c(t)} f_s\, dV_c + \int_{S_c(t)} f_s(\mathbf{V}-\mathbf{W})\cdot\mathbf{n}\, dS = \int_{V_c(t)} q_s\, dV_c, \tag{3.2}$$

where, $V_c(t)$ is the control volume at time t, $\mathbf{V}$ is the fluid velocity, $\mathbf{W}$ is the velocity of the reference system (grid points) and $\mathbf{n}$ is the unit vector normal to the control surface, $S_c(t)$. The derivative d/dt is the rate of change of properties in the control volume, V_c, relative to an observer moving with velocity, $\mathbf{W}$. Here, the absolute volume of the control volume is fixed, while the change in the shape of the volume is brought about by the deforming control surface, $S_c(t)$. The velocity $\mathbf{W}$ varies in both space and time and the method of its evaluation is discussed in section 4.5.

Using the Gauss Divergence Theorem and principles of continuum mechanics, Eq. 3.2 reduces to :

$$\int_{V_c}\left[\frac{df_s}{dt} + f_s\nabla\cdot\mathbf{W}\right] dV_c + \int_{V_c}\nabla\cdot f_s(\mathbf{V}-\mathbf{W})\, dV_c = \int_{V_c} q_s\, dV_c. \tag{3.3}$$

When the control volume is reduced to a mathematical point, Eq. 3.3 can be simplified as the following differential equation,

$$\frac{df_s}{dt} + (\mathbf{V}-\mathbf{W})\cdot\nabla f_s = q_s. \tag{3.4}$$

In the following section Eq. 3.4 is used to obtain the appropriate governing equations and constitutive relations for the deformation of a spreading droplet.

3.2.2 Governing Equations

Figure 3.2 shows the simplified computational domain for an initially unperturbed droplet in contact with a surface, using the assumption that the droplet is modeled as a two-dimensional body. The following derivation of the governing equations holds for both cases of droplet spreading mentioned previously. The essential difference between the two problems lies in the boundary conditions, described further in this chapter. Since the drop spreads on the surface under the influence of gravity alone, it is symmetric in any plane perpendicular to the surface. Due to this symmetry, the drop is treated as an axisymmetric body, and only half of the domain is considered in the analysis.

The fluid flow in the drop is modeled using the Navier-Stokes equations of the conservation of mass and momentum for an incompressible fluid. The governing equations are, therefore :

$$\nabla \cdot \mathbf{u} = 0 \qquad (mass), \tag{3.5}$$

$$\rho \left[\frac{\partial \mathbf{u}}{\partial t} + (\mathbf{u} - \mathbf{u_m}) \cdot \nabla \mathbf{u} \right] = \nabla \cdot \mathbf{T} + \rho \mathbf{g} \qquad (momentum), \tag{3.6}$$

where $\mathbf{u}$ is the velocity vector of the fluid, $\mathbf{u_m}$ is the velocity vector of the reference frame, ρ is the density of the fluid, $\mathbf{T}$ is the total stress tensor, and $\mathbf{g}$ is the acceleration due to gravity.

Using the constitutive relation for a Newtonian fluid, we get

$$\mathbf{T} = -P\mathbf{I} + 2\mu\mathbf{D} = -P\mathbf{I} + \mu \left[\nabla \mathbf{u} + (\nabla \mathbf{u})^T \right], \tag{3.7}$$

where P is the hydrostatic pressure, $\mathbf{I}$ is the identity matrix, and $\mathbf{D}$ is the rate of strain tensor.

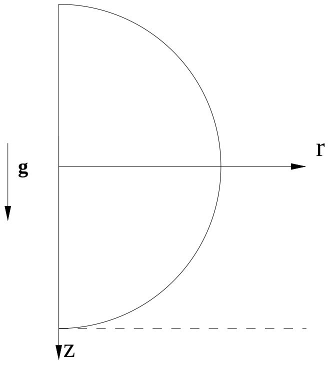

Figure 3.2: The problem domain.

3.2.3 Boundary Conditions

The computational domain is bounded by three distinct types of surfaces :

(i) Lagrangian, which corresponds to the free surface of the drop

(ii) Symmetry, which corresponds to the plane of symmetry of the drop

(iii) The base of the droplet, which is either Eulerian or the interface between two similar fluids, depending on the case being modeled.

The approach taken for each boundary condition is as follows :

- The Lagrangian boundaries are material surfaces moving with the local fluid velocity. By considering the pressure balance across the droplet free surface and the effects of surface tension σ, the traction vector $\mathbf{n} \cdot \mathbf{T}$ is defined as

$$\mathbf{n} \cdot \mathbf{T} = (2\kappa)\, \sigma \mathbf{n}, \tag{3.8}$$

  where $\mathbf{n}$ is the outward unit normal vector along the free surface and κ is the mean curvature of the surface given by

$$2\kappa = \kappa_1 + \kappa_2 = \frac{1}{R_1} + \frac{1}{R_2}.$$

Here R_1 and R_2 are the local radii along two mutually perpendicular axes (see Fig. 3.3). From vector calculus,

$$\kappa_1 = \frac{r_{zz}}{[1 + r_z^2]^{\frac{3}{2}}}, \qquad \kappa_2 = -\frac{1}{r\sqrt{1 + r_z^2}},$$

where

$$r_{zz} = \frac{\partial^2 r}{\partial z^2}, \qquad r_z = \frac{\partial r}{\partial z}.$$

Here r is displacement in the direction perpendicular to the axis of symmetry of the droplet and z is displacement along the axis of symmetry of the droplet (as shown in Fig. 3.2).

For our case, since the problem is modeled in two dimensions, we have $R_2 = \infty$, along an axis perpendicular to the rz plane, which implies that $\kappa_2 = 0$. For the finite element implementation, and for convenience in applying the boundary conditions, $\kappa_1 \mathbf{n}$ is re-written as

$$\kappa_1 \mathbf{n} = \frac{d\mathbf{t}}{dS}. \tag{3.9}$$

where $\mathbf{t}$ is the unit tangent vector in the counterclockwise direction along the surface in the rz plane. The advantage of the above substitution is the elimination of the need to evaluate the second order derivative, r_{zz}.

- At the symmetry line, since there is no flow across it, $u_r = 0$. Also, since there is no shear stress in a plane perpendicular to that of the domain being considered, $T_{rz} = 0$, at this symmetry line.

- At the base of the droplet, the specification of the boundary condition depends on the case which is being modeled :

  For the case of the droplet spreading on a solid surface, the Eulerian surfaces are those which, at a particular time during the deformation are in contact with the solid surface; once part of the free surface comes in contact with the wall, the nodes at those boundaries are reclassified as Eulerian with $\mathbf{u} = \mathbf{0}$. Only the contact point is allowed to slip along the surface, in which case the boundary condition reduces to :

$$u_r = \beta \left(\theta - \theta_s\right)^m , \qquad u_z = 0. \tag{3.10}$$

  For the two droplet case, at the interface between the two colliding drops, there is no flow across the contact line, so that $u_z = 0$. Also, there is no shear stress in the contact plane of the two drops and hence, $T_{zr} = 0$.

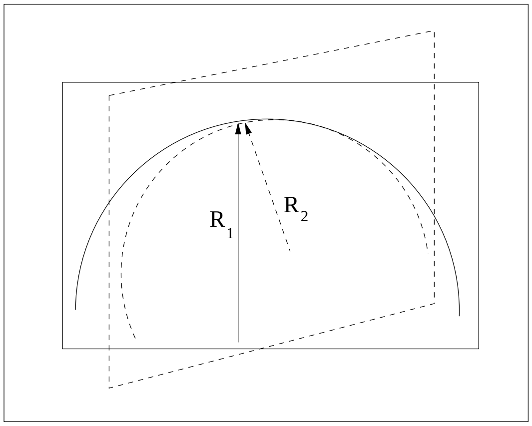

Figure 3.3: Measurement of radii of curvature in two perpendicular planes.

3.2.4 Non-dimensionalization and application of the GEL formulation

The governing equations, Eq. 3.5 and Eq. 3.6, and the constitutive relation, Eq. 3.7, are non-dimensionalized using appropriate characteristic physical quantities to obtain the following dimensionless groups :

$$r^* = \frac{r}{R}; \qquad z^* = \frac{z}{R};$$

$$t^* = \frac{t}{R/\sqrt{2gR}};$$

$$\mathbf{u}^* = \frac{\mathbf{u}}{\sqrt{2gR}}; \qquad P^* = \frac{P}{\mu\sqrt{2gR}/R}; \tag{3.11}$$

where R is the initial radius of the drop and μ is the dynamic viscosity of the Newtonian fluid.

Now, after applying the GEL formulation, the non-dimensional conservation laws of mass and momentum to be solved for the velocity field $\mathbf{u}^*$ and pressure P^*, are obtained as :

$$\nabla \cdot \mathbf{u}^* = 0, \tag{3.12}$$

$$Re\left[\frac{d\mathbf{u}^*}{dt^*} + (\mathbf{u}^* - \mathbf{u}^*_\mathbf{m}) \cdot \nabla\mathbf{u}^*\right] = \nabla \cdot \mathbf{T}^* + St\mathbf{g}^*, \tag{3.13}$$

where $\mathbf{u}^*_\mathbf{m}$ is the non-dimensional velocity vector of the reference frame, and Re is the Reynolds number defined as $Re \equiv \frac{\sqrt{2gR}R}{\nu}$ (where ν is the kinematic viscosity of the fluid). ∇ is the gradient operator with respect to the non-dimensional spatial variables, r^* and z^*.

Here $\frac{d\mathbf{u}^*}{dt^*}$ is the rate of change of the fluid velocity, $\mathbf{u}^*$, as seen by an observer moving with constant velocity, $\mathbf{u}^*_\mathbf{m}$. $\mathbf{T}^*$ is the dimensionless stress tensor given by $\mathbf{T}^* = \frac{\mathbf{T}}{\mu\sqrt{2gR}/R}$.

St is the Stokes number defined as $St \equiv Re\frac{gR}{V^2}$, where V is the characteristic velocity defined as $V = \sqrt{2gR}$ and g is the acceleration due to gravity (due to the non-dimensionalization employed here, $St \equiv 0.5Re$). With the magnitude of gravity absorbed into the Stokes number, $\mathbf{g}^*$ is the non-dimensional gravity vector, given by $\mathbf{g}^* = g_z\mathbf{e_z} + g_r\mathbf{e_r}$, where $g_z = 1$ and $g_r = 0$ and $\mathbf{e_z}$ and $\mathbf{e_r}$ are unit vectors along the positive z and r directions, respectively. In this problem, the gravity vector is taken to be always in the positive z-direction (Fig. 3.2).

The non-dimensional constitutive relation is obtained as

$$\mathbf{T}^* = -P^*\mathbf{I} + 2\mathbf{D}^* \tag{3.14}$$

where the non-dimensional rate of strain tensor is

$$\mathbf{D}^* = 0.5\left[\nabla\mathbf{u}^* + (\nabla\mathbf{u}^*)^T\right] \tag{3.15}$$

After non-dimensionalization, the boundary conditions reduce to :

- The Lagrangian boundaries :

$$\mathbf{n}\cdot\mathbf{T}^* = \frac{2\kappa^*}{Ca}\mathbf{n} \tag{3.16}$$

  where Ca is the capillary number defined as $Ca = \frac{\mu\sqrt{2gR}}{\sigma}$ and κ^* is the non-dimensional mean curvature given by $\kappa^* = \kappa R$.

The corresponding definitions and relations of curvature reduce to :

$$2\kappa^* = \kappa_1^* + \kappa_2^* = \frac{{r^*}_{zz}}{[1+{r^*}_z^2]^{\frac{3}{2}}} - \frac{1}{r^*\sqrt{1+{r^*}_z^2}} \tag{3.17}$$

Also, Eq. 3.9 reduces to :

$$\kappa_1^*\mathbf{n} = \frac{d\mathbf{t}}{dS^*}, \tag{3.18}$$

where κ_1^* is the non-dimensional curvature in the rz plane ($\kappa_1^* = \kappa_1 R$) and dS^* is the incremental non-dimensional arc length ($dS^* = dS/R$).

- The symmetry line :

$$u_r^* = 0 \quad \text{and} \quad T_{rz}^* = 0$$

- The base of the droplet :

  For the Eulerian surfaces :

$$\mathbf{u}^* = \mathbf{0}$$

  When the contact point slips,

$$u_r^* = \beta^*\left(\theta - \theta_s\right)^m, \qquad u_z^* = 0.$$

  For the interface between the two colliding drops :

$$u_z^* = 0 \quad \text{and} \quad T_{zr}^* = 0$$

Hereafter, for convenience, the asterix ($*$) will be dropped from the non-dimensional variables, and all physical quantities mentioned are dimensionless.

Chapter 4

Method of Solution

The governing equations and constitutive relations that were developed in the previous chapter were discretized and solved using the boundary conditions described therein by following the classical mixed Galerkin Finite Element Method. The axisymmetric flow domain was discretized into 6-noded triangular elements, as represented in Fig. 4.1. Gauss-Quadrature numerical integration was then applied and the resulting non-linear equations were solved using the Newton-Raphson iteration procedure.

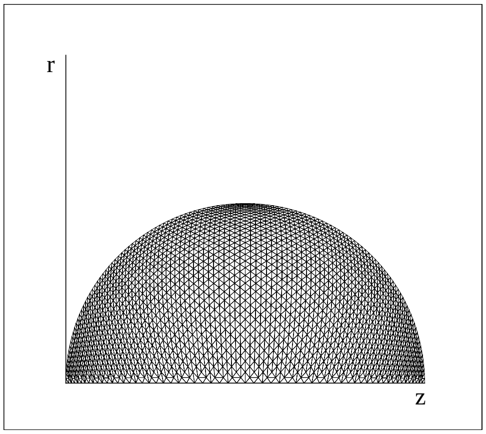

Figure 4.1: The computational domain and mesh.

4.1 Mixed Galerkin Finite Element Formulation

Figure 4.1 shows the triangulated computational domain with the axes located at the exact locations as actually applied in the model, such that the contact line is located at $z = 2 * R$ and the top point of the droplet is at $z = 0$. Consistent with the mixed formulation, the unknown components of the velocity vector, u_r and u_z, were represented using a set of bi-quadratic interpolating functions (ϕ_i), and the unknown pressure, P, using a set of bi-linear interpolating functions (ψ_i). The mathematical expressions for the above statement are given as :

$$u_z = \sum_{k=1}^{6} \phi_k u_k, \quad u_r = \sum_{k=1}^{6} \phi_k v_k, \quad P = \sum_{m=1}^{3} \psi_m P_m \tag{4.1}$$

where ϕ_k and ψ_k denote the basis functions associated with the k-th local node of the triangular element. The coefficients, u_k, v_k and P_m are the values of the unknown physical quantities at the nodes of the triangular elements.

By invoking the traditional finite element procedure and by using the axisymmetric assumption, the residual equations for the domain (shown in Fig. 3.2) were obtained as :

continuity equation :

$$R_c^i = \iint Q_i \left[\nabla \cdot \mathbf{u}\right] r \, dr \, dz \tag{4.2}$$

momentum equation :

$$R_m^i = \iint \left[Y_i \, Re \left(\frac{d\mathbf{u}}{dt} + (\mathbf{u} - \mathbf{u_m}) \cdot \nabla \mathbf{u} - 0.5\mathbf{g} \right) + \mathbf{T} \cdot \nabla Y_i \right] r \, dr \, dz - \int Y_i \, \mathbf{T} \cdot \mathbf{n} \, dS \tag{4.3}$$

The non-zero terms of the stress tensor $\mathbf{T}$, in the momentum equation are :

$$\mathbf{T} = \mathbf{e_r} \, \mathbf{e_r} \, T_{rr} + \mathbf{e_r} \, \mathbf{e_z} \, T_{rz} + \mathbf{e_z} \, \mathbf{e_r} \, T_{zr} + \mathbf{e_z} \, \mathbf{e_z} \, T_{zz} + \mathbf{e}_\theta \, \mathbf{e}_\theta \, T_{\theta\theta} \tag{4.4}$$

where $\mathbf{e_r}, \mathbf{e_z}, \mathbf{e}_\theta$ are unit vectors along the r,z and θ directions respectively.

Since the Galerkin finite element approach was used, the weighting functions Q_i and Y_i are respectively, the interpolating functions, ψ_i and ϕ_i, i.e.,

$$Q_i \equiv \psi_i \qquad Y_i \equiv \phi_i. \tag{4.5}$$

By expressing the above equations (Eq. 4.2 and Eq. 4.3) in terms of the orthogonal directions $\mathbf{i}, \mathbf{j}, \mathbf{k}$ and by appropriately accounting for the boundary terms, the residual equations are expressed as :

continuity equation :

$$R_c^i = \int\!\!\int \psi_i \left[\nabla \cdot \mathbf{u}\right] r\, dr\, dz \tag{4.6}$$

momentum equation in the z-direction :

$$R_{m_z}^i = \int\!\!\int \left[\phi_i\, Re \left(\frac{du}{dt} + (\mathbf{u} - \mathbf{u_m}) \cdot \nabla u - 0.5 g_z\right) + T_{zz}\, \phi_i\, z + T_{zr}\, \phi_i\, r\right] r\, dr\, dz$$

$$- \int \phi_i \frac{2\kappa}{Ca} \mathbf{n} \cdot \mathbf{k}\, dS \tag{4.7}$$

momentum equation in the r-direction :

$$R_{m_r}^i = \int\!\!\int \left[\phi_i\, Re \left(\frac{dv}{dt} + (\mathbf{u} - \mathbf{u_m}) \cdot \nabla v + \frac{T_{\theta\theta}}{r} - 0.5 g_r\right) + T_{zr}\, \phi_i\, z + T_{rr}\, \phi_i\, r\right] r\, dr\, dz$$

$$- \int \phi_i \frac{2\kappa}{Ca} \mathbf{n} \cdot \mathbf{j}\, dS \tag{4.8}$$

where $dS = r\, dS_a$, and dS_a is the (non-dimensional) arc length along the free surface, given by the relation $dS_a = \sqrt{dr^2 + dz^2}$.

4.2 Calculation of the local curvature

Since surface tension plays an important role in the spreading of the droplet, proper evaluation of this physical quantity has to be ensured. From a mathematical and numerical point of view, the consideration of surface tension occurs at the boundary of the computational domain (Fig. 4.1) for the Eulerian surfaces as discussed in section 3.2.3. This evaluation depends upon the calculation of the local curvature, the accuracy of which is critical for this problem. To ensure proper accuracy, the curvature was calculated and compared using two distinct methods :

(a) Using Eqs. 3.16, 3.17 and 3.18, the boundary integral corresponding to the traction vector due to surface tension can be written as

$$\int \phi_i \frac{2\kappa}{Ca} \mathbf{n} \, dS = \int \frac{\phi_i}{Ca} \left(\frac{d\mathbf{t}}{dS} - \frac{1}{r\sqrt{1+r_z^2}} \mathbf{n} \right) dS \tag{4.9}$$

Applying integration by parts, we get

$$\int \phi_i \frac{2\kappa}{Ca} \mathbf{n} \, dS = \phi_i \left. \frac{r\mathbf{t}}{Ca} \right|_2 - \phi_i \left. \frac{r\mathbf{t}}{Ca} \right|_1 - \int \frac{\mathbf{t}}{Ca} \frac{d\,(r\phi_i)}{dS} \, dS_a - \int \frac{\phi_i}{Ca\sqrt{1+r_z^2}} \mathbf{n} \, dS_a \tag{4.10}$$

where subscripts 1 and 2 refer to the endpoints of the boundary elements along the free surface of the droplet, in the counterclockwise direction. Now, the contribution of $(\phi_i \, r \, \mathbf{t}|_2 - \phi_i \, r \, \mathbf{t}|_1)/Ca$ vanishes everywhere *except* at the end points. If, at the end points, the liquid meets a solid surface then the tangent vector, $\mathbf{t}$ there, is related to the contact angle, θ.

(b) Alternatively, the local curvature was evaluated using the definitions of κ_1 and κ_2 at each point along the free surface : κ_1 is evaluated by prescribing a circle through the point of interest and its two adjacent neighboring points and κ_2 by calculating the distance to the axis of rotation (z-axis) along the normal direction

(Fig. 4.2). Note that Fig. 4.2 shows an enlarged picture for better clarity. In reality the difference between the actual and numerically calculated values is a very small percentage of the real value of R_2.

Both methods yield identical results in all cases except at higher Re numbers and whenever the curvature changed sign. The pointwise calculation of the components of the curvature (approach (b)) was consistently more accurate (determined through comparison with expected values at specific locations such as the top point of the droplet) both in magnitude and sign, during the entire spreading process. In the case of the spreading of a droplet on a solid surface, since the dynamic contact angle was a known value, approach (a) was used for the evaluation of the boundary integrals.

For the two droplet case, however, the surface tension at the contact point of the two droplets was evaluated using approach (b). The motion of this point poses some physical and mathematical issues which require careful handling. With a small radius of curvature in the plane of the geometry (R_1 in Fig. 4.2), the surface tension attains very high values at all times during the spreading, which causes high spreading velocities at the contact point. In addition to this, during the initial stages of the spreading, R_2 is very small (near-zero) since the droplet has a nearly spherical shape. As a result, the surface tension at the contact point tends to infinity and the contact point moves very quickly, decelerating as the surface tension falls to more reasonable values (as R_2 increases). This is an inherent physical aspect of the problem. Added to this, since we need to use discrete points to numerically model these physics, there is an implied cutoff point which then underestimates the motion of the contact point, since it assumes a value of R_2^* which is slightly higher than the actual value, R_2 (Fig. 4.2). The dynamics discussed here are in addition to the spreading of the droplet due to the motion of the neighboring fluid, which is discussed in section 5.1.

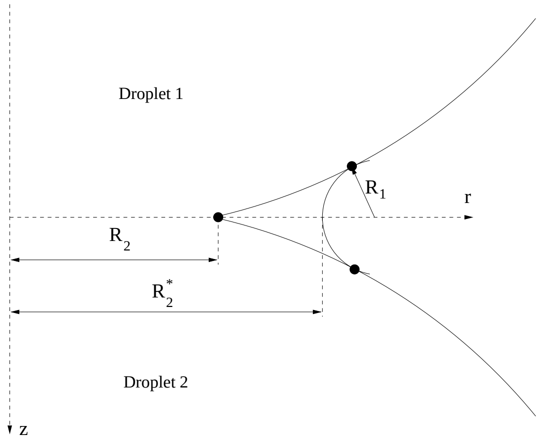

Figure 4.2: Evaluation of the local curvature.

4.3 The Dynamic Contact Angle

As mentioned in the previous chapter, the motion of the contact point is very crucial to the spreading of the droplet on a solid substrate. This motion is quantified in terms of a finite slip velocity, V_{slip}, which is assumed to depend upon the dynamic contact angle, according to the commonly used "power law" constitutive relation [2] :

$$V_{slip} = \beta \left(\theta - \theta_s\right)^m , \tag{4.11}$$

where θ is the dynamic contact angle (the angle that the droplet makes with the solid surface during spreading) and θ_s is the static contact angle (the angle when the contact point is at rest) (Fig. 4.3). Rewriting this equation, we get the expression for the dynamic contact angle as,

$$\theta = \left(\frac{V_{slip}}{\beta}\right)^{\frac{1}{m}} + \theta_s, \tag{4.12}$$

which was used to define the tangent vector, $\mathbf{t}$, according to Eq. 4.10. However, since the weak formulation of the Finite Element Method was used, this boundary condition, in the computations, could only be satisfied in an average sense. In view, however, of the importance of the motion of the contact point, Eq. 4.11 was enforced exactly within each iteration step.

At this point, it is appropriate to consider the manner in which the contact point is affected according to Eq. 4.11. To consistently predict the proper direction of the slip velocity, m must be an odd number. This is to avoid the use of two different equations to define the direction of slip velocity [2]. Customarily, a value of $m = 3$ is used [2]. Since Eq. 4.11 relates the slip velocity to the *difference* in the dynamic and static contact angles, the direction of this velocity depends on the relative magnitudes of the two angles. For instance, when the dynamic contact angle (θ) is greater than the static contact angle (θ_s), as shown in Fig. 4.3(a), the velocity of the contact point is positive, pointing outwards from the center of the contact area. Consequently, the contact point moves forward on the surface and the local profile of the droplet tends to an angle closer to the fixed value of θ_s. Similarly, when θ_s is smaller than θ (Fig. 4.3(b)), the vice versa occurs and the contact point tends to move backward and *towards* the center of the contact area. This dynamic change of the contact angle occurs, until the droplet reaches a static condition when the contact angle, θ becomes equal to the static angle, θ_s. At this point, the contact velocity, according to Eq. 4.11, becomes zero and the fluid within the droplet eventually comes to rest.

It is worth noting that, only the forward-most point in contact with the solid surface slips, while those already in contact with the surface and completely inside the contact region stay with the solid surface. This is consistent with the concept of the slip of the contact point [13].

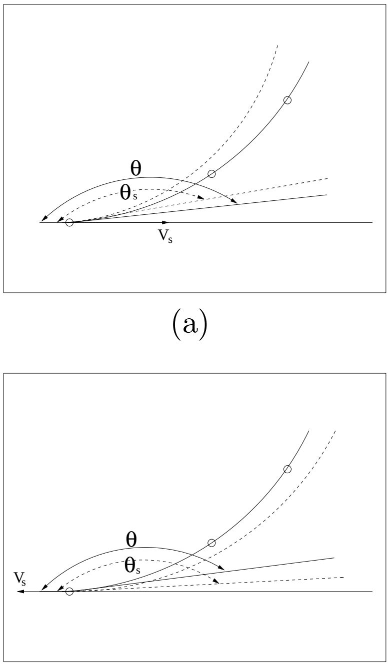

(a)

(b)

Figure 4.3: Motion of the contact point for : (a) Positive slip velocity (b) Negative slip velocity. Here, solid lines indicate the shape of the droplet at the current instant of time and the dashed lines indicate the final shape of the droplet which makes the predefined angle (θ_s) with the solid surface.

4.4 The Newton-Raphson Iteration Procedure

After the classical isoparametric transformation to area coordinates and an appropriate Gauss-Quadrature numerical integration of the governing equations in each element, the resulting system of nonlinear algebraic equations was solved using the Newton-Raphson iteration procedure. This scheme is mathematically expressed as :

$$\mathbf{J}\left(\mathbf{q}^{(\mathbf{n+1})} - \mathbf{q}^{(\mathbf{n})}\right) = -\mathbf{R}\left(\mathbf{q}^{(\mathbf{n})}\right) \tag{4.13}$$

Here, $\mathbf{R}$ is the vector of the weighted residuals, $\mathbf{q}$ is the vector of the unknowns, $\mathbf{q} = \{u_1, v_1, P_1, ...u_N, v_N, P_N\}$, and $\mathbf{J}$ is the Jacobian of $\mathbf{R}$ with respect to the nodal unknowns $\mathbf{q}$. Thus all the nodal unknowns of the velocity components and pressure are evaluated simultaneously. The free surface is calculated automatically by properly assigning the velocity of the nodes along the free surface to reflect the fact that the free surface is a material surface. All time derivatives were evaluated using a fully implicit finite difference scheme.

For the Newton-Raphson iteration scheme, the Jacobian assumes the following form :

$$\mathbf{J} = \begin{bmatrix} \frac{\partial R^i_{m_z}}{\partial u_j} & \frac{\partial R^i_{m_z}}{\partial v_j} & \frac{\partial R^i_{m_z}}{\partial P_j} & \cdots \\ \frac{\partial R^i_{m_r}}{\partial u_j} & \frac{\partial R^i_{m_r}}{\partial v_j} & \frac{\partial R^i_{m_r}}{\partial P_j} & \cdots \\ \frac{\partial R^i_{c}}{\partial u_j} & \frac{\partial R^i_{c}}{\partial v_j} & \frac{\partial R^i_{c}}{\partial P_j} & \cdots \\ \vdots & \vdots & \vdots & \ddots \end{bmatrix} \tag{4.14}$$

In the above matrix, the derivatives with respect to the unknowns are given by :

$$\frac{\partial R^i_c}{\partial u_j} = \iint \psi_i \frac{\partial \phi_j}{\partial z} r\, dr\, dz, \quad \frac{\partial R^i_c}{\partial v_j} = \iint \psi_i \frac{\partial \phi_j}{\partial r} r\, dr\, dz, \quad \frac{\partial R^i_c}{\partial P} = 0 \tag{4.15}$$

and, if the velocity vector of the reference frame can be written as :

$$\mathbf{u_m} = u_{m_z}\mathbf{e_z} + u_{m_r}\mathbf{e_r},$$

as :

$$\begin{aligned} \frac{\partial R^i_{m_z}}{\partial u_j} &= \iint \phi_i\, Re \left(\phi_j \frac{\partial u_z}{\partial z} + (u_z - u_{m_z}) \frac{\partial \phi_j}{\partial z} + (u_r - u_{m_r}) \frac{\partial \phi_j}{\partial r} \right) r\, dr\, dz \\ &+ \iint \left(\phi_{i}z \frac{\partial T_{zz}}{\partial u_j} + \phi_{i}r \frac{\partial T_{zr}}{\partial u_j} \right) r\, dr\, dz \end{aligned} \tag{4.16}$$

$$\frac{\partial R^i_{m_z}}{\partial v_j} = \iint \left[\phi_i\, Re \phi_j \frac{\partial u_z}{\partial r} + \left(\phi_{i}z \frac{\partial T_{zz}}{\partial v_j} + \phi_{i}r \frac{\partial T_{zr}}{\partial v_j} \right) \right] r\, dr\, dz \tag{4.17}$$

$$\frac{\partial R^i_{m_z}}{\partial P_j} = -\iint \psi_j \, \frac{\partial \phi_i}{\partial z} \, r \, dr \, dz \tag{4.18}$$

$$\frac{\partial R^i_{m_r}}{\partial u_j} = \iint \left[\phi_i \, Re \left(\phi_j \, \frac{\partial u_r}{\partial z} + \frac{1}{r} \, \frac{\partial T_{\theta\theta}}{\partial u_j} \right) + \left(\phi_i z \, \frac{\partial T_{zr}}{\partial u_j} + \phi_i r \, \frac{\partial T_{rr}}{\partial u_j} \right) \right] r \, dr \, dz \tag{4.19}$$

$$\begin{aligned} \frac{\partial R^i_{m_r}}{\partial v_j} &= \iint \phi_i \, Re \left((u_z - u_{m_z}) \, \frac{\partial \phi_j}{\partial z} + \phi_j \, \frac{\partial u_r}{\partial r} + (u_r - u_{m_r}) \, \frac{\partial \phi_j}{\partial r} + \frac{1}{r} \, \frac{\partial T_{\theta\theta}}{\partial v_j} \right) r \, dr \, dz \\ &\quad + \int \left(\phi_i z \, \frac{\partial T_{zr}}{\partial v_j} + \phi_i r \, \frac{\partial T_{rr}}{\partial v_j} \right) r \, dr \, dz \end{aligned} \tag{4.20}$$

$$\frac{\partial R^i_{m_r}}{\partial P_j} = -\iint \psi_j \, \frac{\partial \phi_i}{\partial r} \, r \, dr \, dz \tag{4.21}$$

Using the constitutive relations from Eqs. 3.14 and 3.15, and the finite element formulation from Eq. 4.1, the derivatives of the stress components can be obtained as :

$$\begin{aligned} &\frac{\partial T_{zz}}{\partial u_j} = 2 \, \frac{\partial \phi_j}{\partial z}, \quad \frac{\partial T_{zr}}{\partial u_j} = \frac{\partial \phi_j}{\partial r}, \quad \frac{\partial T_{rr}}{\partial u_j} = 0; \\ &\frac{\partial T_{zz}}{\partial v_j} = 0, \quad \frac{\partial T_{zr}}{\partial v_j} = \frac{\partial \phi_j}{\partial z}, \quad \frac{\partial T_{rr}}{\partial v_j} = 2 \, \frac{\partial \phi_j}{\partial r}; \end{aligned} \tag{4.22}$$

The resulting equations from the Newton-Raphson iterative procedure are of the form :

$$\mathbf{J \Delta q} = -\mathbf{R}.$$

where the Jacobian $\mathbf{J}$ is the global coefficient matrix, which is formed by the assembly of the element matrices and is stored as a banded matrix. $\mathbf{R}$ is the right hand side vector, which is formed from the individual element right-hand side vectors, after appropriate modifications and accounting for the boundary conditions (as discussed in section 4.2). The vector of unknowns, $\mathbf{q}$, which we are solving for is obtained from the above equation using a direct solver based on the Gauss Elimination Method, using partial pivoting.

4.5 Mesh construction and control

An important step in the process of a numerical solution is the construction of the computational grid. In the context of the method used here, this issue is vital, due to the approach of the Generalized Eulerian Lagrangian Formulation, which requires frequent remeshing of the problem domain.

The initial mesh was constructed by mapping the semi-circle of the computational domain in Fig. 4.1, into a square of unit length (Fig. 4.4). The coordinates of the vertices of the triangular elements used in the Finite Element analysis were obtained using the Laplacian function, $\nabla^{\mathbf{2}}\mathbf{r} = 0$ and $\nabla^{\mathbf{2}}\mathbf{z} = 0$, where ∇, was defined with respect to the coordinates of the unit square. This initial mesh was improved by using the Delaunay triangulation and consequently, a bandwidth reduction renumbering scheme was employed to minimize the bandwidth of the algebraic system.

During deformation, the mesh deforms according to the GEL formulation; the nodes classified as Lagrangian move with the fluid velocity, while all other nodes move with the prescribed velocities of the reference frame. After numerous experimental schemes, the simplest and most effective scheme to move the "general nodes" was found to be one in which the vertices of the finite element mesh moved with the fluid velocity and the middle nodes moved with the average velocity of the neighboring points. In other words, the material points on the free surface move with the fluid as the droplet deforms, while the internal points move with the reference frame velocity, $\mathbf{W}$ which is calculated as the average of the velocity of the neighboring nodes using the Laplacian function, $\nabla^2\mathbf{W} = 0$. This captures the distinct advantage of the GEL formulation in that, the mesh deforms consistent with the dynamics of the control volume, while preventing large distortions in the fluid domain. Every M time steps, the entire domain was remeshed by relocating each node at the average distance between its neighbors and the Finite Element interpolating functions (ϕ_i and ψ_i) were used to interpolate the field variables of the new mesh.

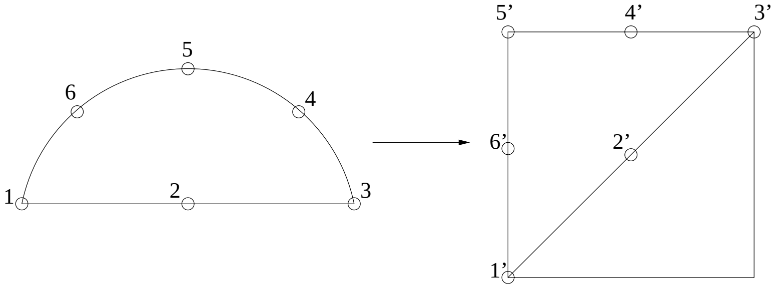

Figure 4.4: The mapping between the semi-circle and a square.

Chapter 5

Results and Discussion

The results presented in this chapter were obtained for the two cases introduced in Chapter 3: that of a droplet spreading after the impact of two identical droplets and that of a droplet spreading on a solid substrate. As mentioned previously, the problem in both situations is axisymmetric as well as symmetric in any plane perpendicular to the surface on which the droplet spreads. Hence, without loss of generality, it is modeled as a two-dimensional droplet and only one half of the domain was considered (Fig. 3.2). This domain was discretized using 900, 6-noded triangular elements and 1891 nodes. The important parameters during spreading are the acceleration due to gravity, the viscosity of the fluid, the surface tension of the interface and the radius of the droplet. These parameters are expressed using the dimensionless Reynolds (Re), capillary (Ca) and Stokes (St) numbers. However, due to the particular non-dimensionalization used here, the Stokes number reduces to $St \equiv 0.5Re$. Hence, all results are classified and discussed based on Ca and Re.

The simulations were performed for two cases : (a) *two identical droplets colliding* and (b) *a droplet spreading on a plane solid surface.* The results reveal the dynamics of spreading as a function of the physical parameters mentioned previously. In the following sections, we discuss the spreading phenomena that were observed during the study of the above mentioned cases and their dependence on several factors such as physical properties of the liquid, influencing forces and the boundary conditions. In addition, the stability of the droplet and the dynamic change in its external profile, as time progresses are discussed. To better understand the phenomena observed, the bulk motion of the fluid within, the development of instabilities and the emergence of recirculating zones are also discussed.

The numerical results reported here are effectively independent of spatial and temporal discretizations. Figure 5.1 demonstrates the independence of the results with respect to the spatial discretizations. These figures plot the variation of the velocity of the top point (non-dimensional) with respect to non-dimensional time, for the case of a droplet spreading on a plane solid surface. The coarse mesh was obtained through a discretization consisting of 392, 6-noded triangular elements and 841 nodes, while the fine mesh consisted of 900, 6-noded triangular elements and 1891 nodes. As can be observed, the two lines trace a very similar trend in all cases ((a)$Ca = 2.0, Re = 1.0$; (b)$Ca = 1.0, Re = 1.0$; (c)$Ca = 0.2, Re = 0.5$; (d)$Ca = 0.1, Re = 0.01$). In Fig. 5.1(d), however, the difference is more noticeable, but acceptable, based on the time taken to attain equilibrium and the difference in values, relative to the amplitude scale. This case corresponds to $Ca = 0.1$ and $Re = 0.01$. While the results obtained matched very well for both meshes over most of the range of Ca and Re, for very low values of both parameters, a slight difference (as mentioned above) was noticed. Similarly, Fig. 5.2 shows the independence of the results with respect to the temporal discretizations. As can be observed, by halving the size of the time step, there is no detectable change in the trend of the top point velocity, for a droplet spreading on a plane surface (with $Ca = 1.0$ and $Re = 1.0$). The results were reproducible over the entire range of Ca and Re, regardless of the time step. Whenever possible, the results were compared with exact analytic solutions; during the first time step, and prior to spreading, the calculated fluid pressure was the exact pressure predicted by the analytic solution, $P = 2/Ca$, (within the computational accuracy). Furthermore, the initial acceleration of the fluid due to gravity was also predicted exactly.

5.1 Two identical droplets colliding

In this case, two identical droplets, initially at rest, spread due to the action of gravity (acting in opposite directions and towards the contact line on both droplets). This case simulates the behavior of two viscous droplets in a hypothetical situation, where gravity forces both drops *towards* each other, after a collision, in which the inertia of the droplets is very low and comparable to the effects of surface tension and viscosity. This case may be appropriate for the simulation of micromanufacturing, in which the interaction of two liquid droplets is important.

Unlike the case of a droplet spreading on a solid surface, no singularity at the contact point is caused by a no-slip boundary condition, in this case. The absence of singularity and its effects allows the study of spreading dynamics that are free of mathematical complexities. In addition, since the only surfaces in contact are fluid surfaces and there is no interference of any external surfaces, the two droplets can physically reach steady state. However, the manner in which they spread and the extent to which they deform, depend on the relative strength of surface tension, gravity and viscous forces. As mentioned in section 4.2, the evaluation of the mean curvature at the contact point at the early stages of the simulation is approximated by the numerical discreteness of the solution. However, the affect of this limitation on the results of this study is negligible.

For this case, we observed two distinct behaviors that depend on the Reynolds and capillary numbers. The first behavior is that of a stable oscillating droplet which eventually reaches steady state. During the oscillations, the droplet retains its near-spherical shape. The second behavior is that of a droplet which becomes unstable, and eventually disintegrates. Due to the symmetry about the contact line, results are shown only for a single droplet.

The behavior of the two droplet spreading is mapped in Fig. 5.3 with the inverse of the capillary number on abscissa and the Reynolds number on the ordinate. The parameter $1/Ca$ indicates directly the effects of surface tension for a fixed value of viscosity. This map indicates the ranges of Ca and Re for which the droplet exhibits the behaviors mentioned above. The circles (•) in this map show the cases where the droplet oscillates, and reaches a stable state after a sufficiently long time. The squares (■) in the map show the cases where the droplet becomes unstable, and eventually disintegrates. In this case, due to relatively higher energy and a weaker dissipative mechanism, the droplet deforms to an extent greater than can be held by the surface tension and hence, breaks up before it can reach a stable steady state. The hollow circle (○) and square (□)) symbols on this map represent the two cases for which the behaviors are discussed, in detail, in the following sections. An estimated boundary between these different behaviors has been sketched in to demarcate the ranges of Re and Ca to which the behaviors correspond. In the discussion, case 1 refers to the stable behavior of the droplets, while case 2 refers to the unstable behavior. In contrast to the spreading of a droplet on a solid surface, a non-oscillatory behavior is not noticed for the two droplet case, since the contact line separates two fluid domains and the fluid flow in each droplet causes the droplets to oscillate.

Figure 5.4 shows a similar map, but in this case, the abscissa represents the effect of surface tension alone, and the ordinate represents the effect of viscosity and gravity. As can be observed, as the viscosity in the drop decreases and the effect of gravity increases (moving upwards along the ordinate), the droplet becomes unstable and changes behavior from an oscillatory to a disintegrating state. Similarly, as the surface tension increases (moving along the abscissa), the ability of the droplet to deform decreases and it disintegrates sooner than if the surface tension were lower.

Figure 5.5 shows the effect of varying gravity on the stability of the droplet. While the abscissa contains terms pertaining to surface tension and viscosity, the ordinate contains terms pertaining to gravity. Thus, moving along the ordinate would imply changing the value of gravity while keeping the rest of the influencing parameters constant. As can be seen from the figure, when gravity increases in value, the droplet behavior changes from stable to unstable, which is expected. The boundary point which corresponds to a capillary number of 1.0 and a Reynolds number of 0.1 exhibits a border-line behavior, leaning closer to an unstable behavior.

Stable behavior

Figure 5.6 shows a typical stable behavior for the two colliding droplets (case 1). Due to the action of surface tension, the droplet develops an oscillatory motion. These oscillations are gradually damped out by the viscosity of the fluid, and the two drops attain a near-steady state, where the change in velocities is very small, while the two droplets maintain contact. This figure depicts the external profile of the droplet and the velocity field of the fluid within, at different times during the spreading process. As can be noticed, in this mode, the droplet retains a near-spherical shape at all times without substantial deformation. This behavior occurs in droplets with relatively high viscosity (i.e., higher viscous forces) and low gravity effects (low Re) and also for droplets with lower surface tension (high Ca). In other words, since gravity, being the deforming force, is weaker here than in case 2, where the droplet becomes unstable, the shape of the droplet remains more or less spherical. And since the restoring force (surface tension) is also weaker, compared to the viscous forces, the droplet tends to oscillate. This is evident especially near the line of contact of the two drops. When a droplet attains equilibrium, the rate of spreading is very low, and the velocity field within the drop and its external profile do not undergo any significant change over a sufficiently long period of time.

Figure 5.7 illustrates a typical behavior of fluid motion in the vicinity of the the contact line. The four pictures in this figure correspond to the same times as the previous figure and the hollow rectangle in the inset indicates the region enlarged in each frame. Figure 5.7(a) shows the velocity field near the contact line at an early instant of time as the droplets spread outward and towards each other. At a subsequent instant in time (Fig. 5.7(b)), due to the oscillations, the velocity at the contact line evidently reverses direction, while the fluid inside the drops continues to move towards the contact line. This appears to induce a recirculation of the fluid near the contact line. As the droplets spread further under the action of gravity, the velocity field returns to its original direction of outward motion (Fig. 5.7(c)). The oscillations repeat, causing the velocity to alternate direction (Fig. 5.7(d)). This sequence repeats itself and eventually the droplets attain a state, in which the spreading rate is near-zero. This behavior is limited only to a certain range of Re and Ca, outside which an unstable behavior is observed, as is discussed below.

Unstable behavior

Figure 5.8 shows a typical spreading behavior, where, unlike the steady oscillating case, the colliding droplets disintegrate (case 2). Due to the excessive deformation, the simulations break down before the two droplets merge into a single larger drop. And because of higher surface tension than in case 1 which tends to restore the droplet to its original shape and low viscosity, the fluid does not have an effective dissipative mechanism to hold the drop together. Figure 5.8 shows the drop shape and the velocity field of the fluid inside, at progressive instants of the spreading. With a stronger effect of gravity, the droplet deforms much more than in the previous case. However, the strong surface tension forces resist this deformation and under the action of these opposing forces, the droplet disintegrates. Figure 5.8 shows the extent of deformation that the droplets progressively undergo. This figure also shows that the magnitude of the velocity field inside the droplets is higher than that of the earlier case. This is especially evident in the region near the contact line, which is discussed in more detail below.

Similar to the previous case, Fig. 5.9 depicts the contact line motion in greater detail for an unstable droplet. Here too, the four pictures in the figure correspond to the same times as Fig. 5.8 and the hollow rectangles in the inset indicate the enlarged region which is shown in each frame. Figure 5.9(a) depicts the velocity field near the contact line as the drops spread outward and towards each other. Due to the strong effect gravity, the velocities reach high magnitudes. With the contact line being a fluid-fluid interface, all points on it have finite velocities and participate in the spreading process. As the spreading continues, the drops begin to deform and the velocities near the contact point grow in magnitude (Figs. 5.9(b) and 5.9(c)). Eventually, this deformation becomes substantial and the velocity near the contact point reaches very high values, as can be seen in Fig. 5.9(d). At this point, the fluid near the contact line has much greater velocities than that in the remaining part of the droplets. Hence, the drops cannot hold together any longer and they break up.

Figure 5.10 illustrates the effect of the capillary number on droplet spreading in the two-droplet case. The figure shows the shape of the droplet at a fixed Reynolds number ($Re = 30.0$), but variable capillary numbers. As can be noticed, the effects of capillary number are more pronounced near the contact area; as expected, the droplets spread further with increasing Ca, i.e., with decreasing surface tension.

A similar, but more significant difference, is observed when the capillary number is kept constant, and the Reynolds number is varied (Fig. 5.11). For instance, Fig. 5.11(d) shows a distinct difference in the profiles of the droplet as the Reynolds number increases from a value of 0.5 to 5.0, and then to 30.0. The innermost profile corresponds to the lowest Re (higher fluid viscosity), while the outermost corresponds to the highest Re (lower fluid viscosity). This too, agrees well with the expected behavior where, for a more pronounced effect of gravity relative to viscous forces, the drop deforms to a greater extent. A close look at the profiles and the corresponding Reynolds numbers reveals that the extent of deformation of the droplet varies non-linearly with the Reynolds number. While the change in the shapes is significant when the Reynolds number changes ten-fold from a value of $Re = 0.5$ to $Re = 5.0$, the change in shape is barely noticeable for a six-fold increase of the Reynolds number from a value of $Re = 5.0$ to $Re = 30.0$.

5.2 Spreading of a drop on a solid surface

These results correspond to a spherical droplet initially at rest and in contact with a plane solid surface. At time, $t = 0$, the droplet is released and allowed to spread on to the surface under the combined influence of gravity, viscosity and surface tension.

For this situation, the results were obtained using : (a) the no-slip boundary condition and (b) a finite slip condition at the contact point. In the case of the no-slip condition (a), it is assumed that any point that comes in contact with the solid surface comes to rest, relative to the surface, and all other points in the droplet move with the velocity of the fluid. In addition, it is also assumed that the spreading of the fluid is fully reversible, so that during sustained oscillations, the material points already in contact with the solid surface can leave the surface as shown in Fig. 5.12(a). However, when the case of irreversible fluid spreading was considered, there was no noticeable difference in the behavior of the droplet and the modes of spreading were identical with those of reversible spreading in exactly the same ranges of Reynolds and capillary numbers. As discussed earlier, it is assumed that the liquid and solid surfaces are chemically "related", i.e., under equilibrium conditions, the static contact angle, between the liquid free surface and the plane solid surface is *a priori* known, and is a property of the liquid-fluid-surface system. In this case, however, it is assumed that the forward-most point on the liquid free surface (the contact point) moves with a velocity relative to the surface and the difference in these velocities is expressed in terms of a slip coefficient, β, while all other points which are in contact with the surface do not slip. In other words, the movement of the contact point occurs due to the cumulative effect of a slip velocity and the motion of the material points near the point of contact (Fig. 5.12(b)). Also, the droplet spreading in this case was considered to be non-wetting, such that the contact angle always remained above 90°. When a wetting case was attempted, the droplet underwent severe deformation and the automatic mesh generator could not handle such high distortion, causing the code to diverge. In the following pages, the results for both cases are discussed and compared for different values of the slip coefficient, β and the dimensionless control parameters, Re and Ca.

5.2.1 No-slip boundary condition

Dynamics of Spreading

The results presented here are discussed for the case where there is no relative motion between the contact point and the solid surface, i.e., $\beta = 0$. In contrast to the case of the spreading of one droplet on another (discussed in the previous section), in this case, the no-slip boundary condition leads to a mathematical singularity at the contact point. Consistent with the expectation that the dynamics of droplet spreading are predominantly effected by viscous, gravity and capillary forces, the dependence of the spreading on capillary and Reynolds numbers was investigated. As a result, it has been found that the relative magnitude of these two non-dimensional numbers relates to the droplet spreading in one of three distinct manners, in this case: stable, oscillatory and splashing (or disintegrating). As the top point of the droplet is the farthest from the surface, the variation of the velocity at this point is indicative of the fluid in the bulk of the drop. Thus, to determine and classify the manner in which the drop spreads on the solid surface, the velocity of the top point of the droplet is used to illustrate the trend of the velocity field at all points inside the droplet. Figure 5.13 shows the variation of this velocity for the three behaviors mentioned above. Here, positive velocity represents motion of the droplet towards the solid surface and negative velocity represents motion away from the surface.

For the two droplet case, the focus of the study was the motion of the contact point and hence the results were classified based on the droplet behavior, which was governed by the contact line motion. However, in the case of a droplet spreading on a plane surface, with no slip, since the velocity of the contact point is zero, the behavior of the droplet is classified based on the motion of the top point, which is more appropriate, as explained above.

When the droplet spreads on a plane surface in a stable manner, it typically spreads downward (towards the surface) due to the action of gravity, and quickly reaches equilibrium. In contrast to this behavior, when the droplet spreads in an oscillatory manner, with a greater effect of surface tension and gravity relative to the viscous forces, it oscillates for some time before eventually attaining a state of equilibrium. If the relative magnitude of surface tension and gravity are further increased, the droplet spreads in the third manner, where it disintegrates or splashes onto the solid surface. These three cases are shown in Fig. 5.13.

When compared to the spreading behavior in the two-drop case, it is observed that a droplet spreading on a solid surface at low Reynolds number and high capillary numbers usually attains equilibrium *without* oscillating. This accounts for the third manner of droplet spreading in this case. This behavior, as expected, results from the no slip boundary condition at the contact point, which tends to bring the fluid in the droplet to rest in a shorter time. Moreover, when low energy droplets, with high viscosity (low Re) collide, they tend to merge into a single bigger drop and one does not expect to see the behavior mentioned above.

An observation worth noting here is that, since the contact angle is not fixed, in the case of the no-slip boundary condition, the droplet never reaches a perfect steady state, where the velocity of the fluid within the drop comes to a complete rest. Rather, it attains a rate of spreading which is very slow, and the velocity of the fluid within the drop is negligible compared to its initial values. This is similar to the behavior that was observed in the two-droplet case, as well.

The Stability Map

Similar to the case of the colliding droplets, the ranges of capillary and Reynolds numbers, for which the drop behaves in the manners discussed above, are graphically shown on a "stability map" in Fig. 5.14. Unlike the two-drop case, however, in this case, *three* different manners of spreading were observed, as discussed above. This map is plotted with the inverse of the capillary number on the abscissa and the Reynolds number on the ordinate, such that the parameter, $1/Ca$, indicates, directly, the effects of surface tension. In the map, the upward pointing triangles (▲) represent the first type of behavior, where the droplet spreads in a stable manner, and quickly attains equilibrium. The circles (●) in the map refer to the second behavior where the droplet oscillates, damping gradually before attaining a state of near-equilibrium. The squares (■) correspond to the cases of the third behavior, in which the droplet splashes on to the surface due to a relatively weaker dissipative mechanism. An interesting behavior which constitutes the fourth type is that of a droplet which rebounds from the solid surface and achieves a greater magnitude of velocity *away* from the surface than towards it. This behavior is indicated by the downward pointing triangles in the map and is discussed in more detail later in this section. The diamonds (♦) on the map represent cases which border between stable and oscillatory modes of spreading. These cases exhibit a predominantly stable behavior, while a velocity away from the surface is also observed. The amplitude of this velocity, however, is several orders of magnitude smaller than that towards the surface. The hollow symbols ($\triangle$, $\circ$, $\square$ and $\triangledown$) in this map represent the cases for which the behaviors are discussed in the following sections. The estimated boundaries between these different behaviors have been sketched in to demarcate the ranges of Re and Ca to which the behaviors correspond.

Since the dynamics of the fluid near the contact line are different for the two situations of droplet spreading, the behaviors exhibited by the droplet and the corresponding ranges of Reynolds and capillary numbers differ for the two cases. This is evident from an examination of the stability maps shown in Figs. 5.3 and 5.14.

Figure 5.15 shows a similar map of the distribution of these cases as a function of Reynolds and capillary numbers. In this map, however, the abscissa represents the effect of surface tension alone, while the ordinate represents the effect of gravity and viscosity on the stability of a drop spreading on a plane solid surface. It can be observed that, as the relative effect of surface tension increases (moving along the abscissa), the behavior of the drop changes from stable to oscillatory. This is expected, since, for a relatively higher effect of surface tension, the restoring force is greater and the droplet tends to oscillate before reaching a state of near-equilibrium. Similarly, as the effect of gravity increases (moving along the ordinate), relative to the viscous forces, the droplet changes behavior first, from stable to oscillatory and then, on to a disintegrating droplet. This is also expected, for, a relatively higher gravity and weaker dissipation help the drop retain more energy and either oscillate or splash on to the surface.

Figure 5.16 illustrates the effect of gravity on the stability of the droplet spreading on a solid surface. While the abscissa shows the effect of surface tension and viscosity, the ordinate shows the effect of gravity and viscosity. Thus, moving along the ordinate implies a changing value of gravity while all other influencing parameters are kept constant. From this figure, it can be deduced that the behavior of the droplet depends on the surface tension and viscosity of the droplet. When surface tension is low, as gravity becomes stronger, the droplet changes behavior from an oscillating droplet to a stable droplet. On the other hand, when surface tension is high, for stronger gravity the droplet changes behavior from oscillatory to splashing. This behavior is expected since, in the latter case, the restoring force of capillarity is stronger than in the former case.

These behaviors of a droplet spreading on a solid surface agree well with those observed experimentally by Matson, Rolland & Flemings [4] of an aluminum-copper alloy impinging onto a thermally conditioned substrate. In their study, Matson *et. al.* considered a solidifying droplet and mapped the behaviors based on Weber number ($We \equiv ReCa$) and a freezing number. The ranges in which the respective behaviors were observed computationally in our analysis correspond to those observed experimentally by Matson *et. al.*.

Fukai *et. al.* [10] studied the spreading behavior of droplets impinging on a solid surface, such that they start with an initial spherical shape and deform into a splat due to the high inertia of collision. The results that they obtained are similar to those presented in this work, in the initial stages of the collision, such that the contact angle never falls below 90°.

A more detailed discussion of these behaviors is below. The figures used in the following discussion depict the velocity field in the droplet at different instances of spreading. The inset in the top left corner of each frame shows an enlarged and clearer view of the velocity field inside the droplet in the region which is marked by the hollow black square on the droplet. The inset in the bottom right corner represents the variation of the velocity of the top point and the small (solid) black square indicates the instant in time to which the velocity field corresponds.

Stable spreading

Figure 5.13(a) shows the velocity of the top point, as a function of the non-dimensional time, for a droplet which spreads in a stable manner. As can be observed, the velocity of the top point towards the surface increases to a maximum value and then gradually decreases to a value of zero relative to the surface. It can also be noticed that the peak velocity of $V_{max} = 0.08$ towards the surface occurs at time, $t = 0.264$. As mentioned before, since the top point of the droplet is the farthest from the surface, its behavior is indicative of that of the fluid in the bulk of the drop. Thus, the drop reaches a state of equilibrium within a relatively short time and remains stable. Similar to the spreading in the two-drop case, equilibrium here corresponds to a state where the velocity field within the drop and its shape do not undergo any significant change over a sufficiently long period of time.

As the stability map (Fig. 5.14) shows, the droplet exhibits this stable behavior for a range of Reynolds and capillary numbers. The values of the peak top point velocity and the times at which they occur are shown in Fig. 5.17, for a fixed capillary number ($Ca = 1.0$) and a range of Reynolds numbers from $Re = 0.01$ to $Re = 0.2$. It can be inferred from this figure that, the maximum droplet velocity increases with the Reynolds number. Figure 5.18(a) illustrates this point more effectively and also gives the relation of the maximum droplet velocity to the Reynolds number as $V_{peak} = 0.35471 Re^{0.49897}$. In addition, Fig. 5.18(b) shows that the time that the droplet takes to reach the peak velocity also increases with the Reynolds number. This agrees with the expectation that, for relatively larger gravity and lower viscous forces, the droplet accelerates more and it takes longer to attain stable equilibrium due to reduced dissipation. The inset shows the interior region because it illustrates the bulk fluid motion better than the flow near the top point.

In this mode, since gravity and surface tension are relatively smaller (low Re and high Ca) than the viscous forces, the droplet spreads and reaches a near-equilibrium state at a relatively short time. Figure 5.19 shows the typical behavior of a droplet spreading in a stable manner. Since the forces which affect the free surface of the drop are relatively smaller in magnitude than the viscous dissipation, the drop remains close to spherical in shape throughout the process of spreading and the deformation is very little.

Figure 5.19(a) shows the velocity field in the droplet at an early instant in time as the drop spreads towards the surface under the influence of gravity. At a later instant in time (Fig. 5.19(b)), the fluid velocity towards the surface increases in magnitude till it reaches a maximum. Thereafter, the velocity of the fluid begins to decrease in magnitude even as the droplet continues to spread towards the surface (Fig. 5.19(c)). Soon after (Fig. 5.19(d)), the velocity of the fluid inside the droplet decreases to a very low value (near-zero) and the droplet attains a state of equilibrium.

When the droplet spreads in a stable manner, the fluid in the region near the contact line moves downward at all times and hence, no recirculation is observed. Rather, the fluid continues to spread downward on the surface till the droplet attains a state of stable equilibrium.

A significant observation in Fig. 5.19 is that all points in the flow field show velocities pointed towards the surface at all times. This is typical and characteristic of a droplet spreading in the stable mode, where no point in the flow field ever moves away from the solid surface. This behavior is in contrast to the oscillatory manner of spreading, discussed in the following section.

Oscillatory spreading

An interesting mode of spreading of the liquid droplet is when it oscillates before reaching a state of equilibrium. In this mode of spreading, with relatively stronger gravity and capillary forces, the droplet possesses higher energy and a weaker dissipative mechanism. As a result, the drop oscillates and the gradual damping of these oscillations eventually brings it to a state of equilibrium. This behavior of the top point of the droplet can be seen in Fig. 5.13(b), which is an indication of a similar behavior in the bulk of the fluid. As can be observed, the top point velocity reverses direction, in contrast to the stable mode, and oscillates several times as the viscosity of the fluid damps it down in magnitude. In this case, since the contact angle is not fixed, the droplet continues to oscillate for a very long time, but after a sufficiently long initial period, the amplitude of these oscillations decreases to a value much smaller than that of the initial oscillations. When the droplet reaches this state, it is very close to stable equilibrium.

Figure 5.20 shows the typical behavior of an oscillating droplet. Similar to the case of a stable droplet, this figure shows a sequence of velocity field in the droplet at different instants of time during the spreading. With a stronger effect of gravity and surface tension on the droplet, the deformation of the free surface is greater. Even though the droplet remains close to spherical in shape, the deformation is noticeably greater than in the stable mode. This deformation in turn has an effect on the manner of spreading, as explained below.

Figure 5.20(a) depicts the velocity field in the droplet at an early instant of time when the fluid inside the droplet moves towards the solid surface as it begins to deform and spread on the surface. At this point, the effect of gravity is stronger (higher Re) than that of surface tension and the damping mechanism is weaker (again, higher Re) than before. But as the droplet deforms more, surface tension become stronger and tends to restore the drop to its original shape. As a result, the bulk of the drop begins to move *away* from the surface (Fig. 5.20(b)) in an attempt to regain its original spherical shape. As this progresses, and the droplet begins to regain its original shape, surface tension becomes weaker and the velocity in the bulk of the droplet decreases, still pointing away from the surface (Fig. 5.20(c)). Soon, the relative magnitude of gravity becomes higher and it tends to move the drop back toward the surface and the velocity changes direction yet again, causing the drop to spread downward (Fig. 5.20(d)). This pattern repeats itself, as the opposing effects of gravity and surface tension drive the droplet back and forth until the amplitude of velocity fluctuations diminishes to a very small value due to viscous dissipation. Thereafter, the velocity field of the fluid inside the droplet and its outward profile do not undergo any significant changes and the droplet approaches a near-equilibrium state.

For an oscillating droplet, with opposing motion of the fluid near the contact line, a slight recirculation occurs in the region close to the solid surface. In several of the cases, this recirculation disappears after an initial time, like in the case discussed above. A very small amount of recirculation in Fig. 5.20(a) appears near the contact point at time, $t = 0.9874$, which soon disappears and does not affect the stability of the droplet. However, in a few cases of an oscillating droplet, this recirculation re-appears several times, but it does not prevent the droplet from attaining a state of near-equilibrium.

Figure 5.21 shows the logarithmic decrement of the amplitude of the top point velocity for the case discussed above. The velocity in this case decreases exponentially as $V_{top} = 0.24775 * exp(-0.40347t)$ with time, and the dominant (dimensionless) frequency of the damping oscillations is 0.5445. This is similar to the trend of the displacement of a spring-mass-damper system, the amplitude of which also falls exponentially.

As mentioned earlier, Lamb [6] obtained analytical expressions for the frequency of oscillations for a viscous droplet. The expressions were reported for the cases when the droplet is affected by either gravity or surface tension alone. These expressions are presented below :
with gravity alone :

$$f = \frac{1}{2\pi}\sqrt{\frac{2n\,(n-1)}{2n+1}\frac{g}{R}} \tag{5.1}$$

with surface tension alone :

$$f = \frac{1}{2\pi}\sqrt{\frac{n\,(n-1)\,(n+2)\,\sigma}{\rho R^3}} \tag{5.2}$$

where f is the frequency of oscillation, n the frequency mode, R the radius of the droplet, g the acceleration due to gravity, ρ the density of the liquid and σ the surface tension.

After appropriate non-dimensionalization, these equations give a frequency of $f = 0.1007$ for gravity alone and $f = 8.94$ for surface tension alone. When similar conditions were simulated in our work, the frequencies obtained were $f = 0.103$ for gravity alone ($Re = 15$ & $Ca = 2$) and $f = 13.6$ for surface tension alone ($Re = 0.005$ & $Ca = 0.01$). While the value for the former case agrees well with Lamb's prediction, that of the latter case differs slightly, which can be attributed to the fact that even at $Ca = 0.01$, the effect of gravity has not been completely eliminated. It is worth noting here, that the frequency of $f = 0.5445$, computed for the case presented above, lies in the range predicted by Lamb in his analytical study.

Similar to the two droplet case discussed previously, the profile of the droplet when it attains a near-equilibrium state depends on the relative magnitude of gravity and surface tension. These profiles are compared for several Reynolds and capillary numbers in Fig. 5.22. The first column of figures shows the effect of varying Re (with Ca held constant). In other words, surface tension is fixed while the effect of changing gravity is considered. These figures show that as Re is increased, the drop deforms to a greater extent. This agrees with the expectation that a stronger effect of gravity leads to a greater drop deformation.

The second column of figures (in Fig. 5.22) tells a similar story, but here, the Reynolds number is kept constant while the capillary number is varied to consider the effects of surface tension on the near-equilibrium position of an oscillating droplet. Here again the figures demonstrate that the drop deforms more when the surface tension is lesser in magnitude (given by the inverse variation in value of the capillary number). This too, conforms to the expectation that with lesser surface tension, the restoring force of the droplet is smaller and hence the deformation greater. In contrast to the two droplet case, however, the effect of varying *Re* and *Ca* on the shape of the droplet is more comparable.

These figures are similar to the comparisons made in the two-droplet case. However, the profiles of the droplet here correspond only to the equilibrium shapes which are attained after a sufficiently long time. While the trends in both situations remain the same, since the influencing factors have not changed, the extent of spread and the contact angle are noticeably different. Also, the difference in profiles for varying Reynolds and capillary numbers is more pronounced for the droplet spreading on a surface. This is due to the difference in the boundary condition at the contact point. In the former case, the motion of the contact point is not restricted and hence the spreading occurs unhindered, while in the latter case, the no-slip boundary condition affects the final shapes that the droplet attains.

The significant difference between a droplet spreading in a stable manner and one spreading in the oscillatory manner, discussed here, is the alternating reversal of velocity in the latter mode. The essential cause for this behavior is a higher energy in the system which is damped out by viscosity in a manner very similar to that of a spring-mass-damper system. If the energy in the system increases beyond what the dissipation mechanism can handle, the drop disintegrates and splashes on to the surface, as is discussed in the following section.

Splashing

Figure 5.13(c) shows the variation of the velocity of the top point for a droplet which spreads in the splashing mode. It is evident from the figure that, in this case, the top point does not come close to rest relative to the solid surface. Instead, the droplet goes unstable and disintegrates. For this case, the amplitude of the velocity fluctuations of the top point is an order of magnitude higher than for the previous cases. The "nick" in the plot of the top point velocity at time, $t \approx 3.3$, is not physical, but a numerical artifact due to the numerical instability that occurs because of very high deformation of the droplet free surface, close to when it breaks up.

Figure 5.23 shows the shape and the velocity field of the fluid in the droplet as it spreads in this mode. Here, since gravity is much stronger than the viscous forces, the droplet deforms into the shape of a flat disc (Fig. 5.23(c)) and beyond (Fig. 5.23(d)) as it spreads onto the surface. With greater deformation, the surface tension increases in magnitude and tends to restore the droplet to its original spherical shape, even as gravity continues to deform the droplet. This causes strong opposing forces in the drop and it eventually shatters.

Figure 5.23(a) shows the velocity field in the droplet as it begins to spread on the surface under the effect of gravity. With relatively weaker surface tension and stronger gravity (higher Re), the droplet deforms to a greater extent and the velocity of the fluid attains larger values (Fig. 5.23(b)) and reaches a maximum. In this mode, since the dissipative mechanism is relatively much weaker than for the previous modes (higher Re), the drop retains its energy for a longer period of time. As the droplet continues to deform, the surface tension (restoring force) increases in value and the velocity then begins to decrease (Fig. 5.23(c)). While the velocity in the upper part of the droplet decreases further and then reverses direction, the fluid in the rest of the droplet continues to spread in the downward direction. This opposite movement of the fluid in the droplet eventually becomes very strong and the droplet tears apart, resulting in splashing immediately after the instant shown in Fig. 5.23(d).

A very significant phenomenon, in this case, is the recirculation near the contact point of the droplet which occurs to a much higher degree than for the oscillatory mode of spreading. Figure 5.24 shows an enlarged view of the recirculation that develops at the contact line just before (t=2.8) the droplet disintegrates. The streamlines show that the motion of the fluid inside the droplet is forced downward at the contact point, which causes the recirculation. At a subsequent time, when the upper part of the droplet begins to move away from the surface, this downward motion at the contact point opposes the upward motion and as a result, the droplet disintegrates.

The above case demonstrates the relation between the recirculation and the stability of the droplet. Another such case, in which the recirculation is more pronounced, is that of the formation of a crown, discussed below.

Splashing with "crown" (as a special case)

When a droplet splashes onto a solid surface, it deforms into a shape in which it cannot hold together as a single entity. One of the shapes that it briefly attains is that of a crown, which has been observed with several fluids [31]. In this case, the values of capillary and Reynolds numbers are different, but the manner of spreading is similar to that of a splashing droplet discussed above. Figure 5.25 shows the velocity of the top point of the droplet as it spreads into the shape of a crown. Unlike the previous example, this droplet goes through a complete cycle of oscillation before it disintegrates. Also, in contrast to the instability observed near the top point in the previous example, the instability for this droplet occurs closer to the contact point.

Figure 5.26 illustrates the manner in which the droplet deforms into a crown and disintegrates. In this case, the capillary number is lower ($Ca = 0.1$) than for the previous example ($Ca = 0.2$, Fig. 5.23) and hence, surface tension is higher, for fixed velocity and viscosity. In other words, since the restoring force is greater, the droplet has a better ability to return to its original spherical shape. However, gravity still dominates and there is not enough viscosity in the fluid to dissipate the energy. Thus, the droplet deforms into the shape of a flat disc (Fig. 5.26(b)), then regains a shape closer to spherical, even as it continues to spread along the surface (Fig. 5.26(c)), and then briefly attains the shape of crown (Fig. 5.26(d)) before shattering.

Figure 5.26(a) corresponds to an early instant in time when the velocity of the top point towards the surface is at its maximum. At this point, as the droplet continues to deform and surface tension effects become stronger. As a result, the velocity of the fluid inside the droplet decreases in magnitude and then reverses direction, such that the droplet begins to move away from the surface (Fig. 5.26(b)). As the droplet begins to regain its original shape, surface tension weakens and the velocity of the fluid away from the surface decreases in magnitude, even as it continues to move away from the surface (Fig. 5.26(c)). After a while, gravity takes over, forcing the droplet towards the surface again. At this point, the fluid near the contact line is still moving away from the surface. As a result of these two opposing motions *towards* each other, the fluid spreads out from the side and forms a crown (Fig. 5.26(d)).

As with the previous example, this case too, displays the presence of recirculation which is related to the droplet disintegration. Figure 5.27 shows the recirculation of the fluid inside the droplet near the contact point. The streamlines show the fluid flow inside the droplet at an instant before it forms into the shape of a crown. As can be observed, the recirculation causes the fluid near the contact point to move *away* from the surface. At a subsequent time, the fluid from the upper part of the drop starts moving towards the surface. When it interacts with this recirculation, the fluid is pushed outward from the droplet's side, as shown in Figure 5.28. This figure corresponds to an instant in time when the crown forms. The streamlines in this figure demonstrate the fluid movement in the manner discussed above.

Spreading dynamics for microgravity conditions

As the values of capillary and Reynolds numbers were varied, the droplet displayed one of the three distinct behaviors discussed above. However, at extremely low values for both parameters, an unusual and unexpected behavior was observed, where stable behavior was expected. Figure 5.29 shows the velocity of the top point of the droplet as it spreads in this mode. As can be observed, the droplet initially appears to recoil from the surface, while still in contact with it (since the contact point remains with the surface), and the fluid begins to move away from the surface. This velocity (away from the surface) increases until the effect of gravity is felt and then decreases in magnitude and then reverses direction towards the surface and quickly reaches a state of near-equilibrium. While the figure shows that the velocity of the top point is pointed away from the surface right from time, $t = 0$, the inset makes it clear that the droplet does, indeed, move towards the surface initially before bouncing back. Another interesting observation is that the amplitude of the velocity away from the surface is greater than that towards the surface. This indicates that the restoring force has a stronger effect than gravity, on the spreading dynamics of the droplet.

Since this behavior of the droplet is not very different from that of stable spreading, except for the initial reversal of velocity, the droplet retains a shape almost spherical throughout the spreading process (Fig. 5.30). This is expected, since the magnitudes of surface tension and viscous forces are much higher than that of gravity, which causes the deformation.

Figure 5.30 shows the sequence of velocity field of the droplet as it exhibits this behavior. Figure 5.30(a) shows the velocity field at an early instant in time after the drop bounces back from the surface. The velocity of the fluid inside the drop is pointed away from the surface and is maximum in magnitude. A little later

(Fig. 5.30(b)), the velocity of the fluid is still pointed away from the surface but the magnitude begins to decrease until it reverses direction and spreads towards the solid surface (Fig. 5.30(c)). The velocity of the fluid increases towards the surface, reaches a maximum and then decreases gradually (Fig. 5.30(d)) as the droplet attains equilibrium.

Similar to the case of the stable droplet, no recirculation occurs in this case and the drop remains in stable equilibrium. This is because of the relatively smaller magnitudes of velocity and a more gradual reversal of the velocity of the fluid within the droplet.

For this case, the values of capillary and Reynolds numbers are $Ca = 0.1$ and $Re = 0.0005$. At these low values, the expected behavior was that of a stable droplet. But since the relative effect of gravity is very low and the effect of surface tension fairly high, the droplet bounces back under the effect of relatively greater surface tension. For this very low Reynolds number, the droplet behavior simulates that which would be observed under low-gravity conditions.

The values of gravity, g (in m/s^2) that this case corresponds to ($Re = 0.0005$) are tabulated in Table 5.1, for different liquid droplets of varying size :

Liquid	*Size of the droplet (cm)*					
	0.1	0.5	1.0	2.0	3.0	5.0
Water	1.25x10^{-9}	1.01x10^{-11}	1.25x10^{-12}	1.57x10^{-13}	4.65x10^{-14}	1.01x10^{-14}
Glycerin	1.42x10^{-3}	1.13x10^{-5}	1.42x10^{-6}	1.77x10^{-7}	5.25x10^{-8}	1.13x10^{-8}
SAE 30 oil	1.76x10^{-4}	1.41x10^{-6}	1.76x10^{-7}	2.2x10^{-8}	6.53x10^{-9}	1.41x10^{-9}

Table 5.1: Physical values of gravity for various liquid droplets

It can be seen from the table that microgravity conditions can be easily realized for droplets in this flow regime. The size of the droplet which corresponds to a gravity of $g = 9.81 m/s^2$ for each of the above liquids is given in table 5.2 below :

Liquid	*Size of the droplet (cm)*
Water	5.04x10^{-5}
Glycerin	5.25x10^{-3}
SAE 30 oil	2.62x10^{-3}

Table 5.2: Droplet sizes which correspond to $g = 9.81 m/s^2$

The properties of these liquids at room temperature are given in Table 5.3 below :

Liquid	*Temperature* $(°C)$	*Density* (kg/m^3)	*Dynamic viscosity* $(kg/m{\cdot}s)$	*Kinematic viscosity* (m^2/s)
Water	15.6	999	1.12x10^{-3}	1.12x10^{-6}
Glycerin	20	1260	1.5	1.19x10^{-3}
SAE 30 oil	15.6	912	3.8x10^{-1}	4.2x10^{-4}

Table 5.3: Physical properties of liquids considered above

5.2.2 Motion of the contact point

The results discussed so far correspond to the cases in which the contact point remains attached to the plane surface, so that there is no slip between the contact point and the surface on which the droplet spreads. However, experimental observations indicate that, in some cases, there appears to be a finite slip velocity of the contact point, relative to the solid surface [12]. In other words, as the droplet spreads on the plane surface, the contact point moves with the fluid, in addition to more points coming into contact with the solid. Hence, a more realistic approach would dictate the inclusion of a slip velocity at the contact point. For this purpose, a slip coefficient, β is defined and the slip velocity is assumed to obey the following empirical power law [2] :

$$V_{slip} = \beta \left(\theta - \theta_s\right)^m \tag{5.3}$$

where θ is the dynamic contact angle and θ_s is the static contact angle, the latter of which is *a priori* known. In the above equation (Eq. 5.3), the slip coefficient, β, is an empirical value which needs to be determined experimentally. Since the slip coefficient is defined such that the slip velocity varies as a power of the difference in the contact angles, the value of this coefficient cannot be determined based on any theoretical or physical arguments (since the dynamic contact angle cannot be predicted through any physical or mathematical model); however, it is critical to the simulation since the dynamic contact angle is determined using the value of β in Eq. 4.12.

In the following results, we investigate the motion of the contact point by varying the magnitude of the slip coefficient, β, while fixing the static contact angle at $\theta_s = 160^\circ$. These results, similar to those obtained for the no-slip boundary condition, correspond to a spherical droplet initially at rest and in contact with a plane solid surface, with $Ca = 1.0$ and $Re = 5.0$. Results are shown for (a) $\beta = 0.1$, (b) $\beta = 0.5$ and (c) $\beta = 1.0$. These results are compared to those with the no-slip ($\beta = 0$) boundary condition.

Figure 5.31 shows the behavior of an oscillating droplet, with $Ca = 1.0$ and $Re = 5.0$ and a no-slip boundary condition at the contact point, i.e., $\beta = 0$. This is taken to be the baseline behavior against which the results of the finite-slip cases are compared. Similar to the case discussed earlier in Fig. 5.20 (for a droplet with $Ca = 0.1$ and $Re = 1.0$), this droplet oscillates as it spreads onto the solid surface. Figure 5.31 shows a sequence of the velocity field of the fluid in the droplet as it moves towards the surface and then away from it before attaining a near-equilibrium position. The insets in each frame show the variation of the velocity of the top point and the small black square in them indicates the instant in time to which the velocity field in the frame corresponds. Figure 5.31(a) corresponds to an early instant in time when the droplet deforms and spreads towards the surface with increasing velocity. This velocity reaches a peak value, decreases in magnitude (Fig. 5.31(b)) and then reverses direction (Fig. 5.31(c)). Soon thereafter, the droplet attains a state of near-equilibrium (Fig. 5.31(d)). The contact point in this case, remains with the surface at all times and tends to bring the fluid in the neighboring region to rest relative to the solid surface.

However, with a finite slip at the contact point, the spreading dynamics of the fluid are affected locally, depending on the amount of slip, the details of which are presented below. For the following discussion, the static contact angle was fixed at 160° and the exponent in Eq. 5.3 at $m = 3$. This value of the exponent takes into account the direction of the velocity of the contact point, depending on the value of the dynamic contact angle relative to the static angle (as explained in page 29). Also, the values of the non-dimensional control parameters were fixed at $Ca = 1.0$

and $Re = 5.0$. The figures in the following discussion show the velocity field of the fluid near the contact point at different instants of spreading. The inset in the top left corner of each frame depicts the shape of the entire droplet to which the enlarged view corresponds, while the inset in the opposite corner illustrates streamlines relating to this flow.

Figure 5.32 shows the spreading behavior of the droplet on a solid plane surface, for a slip coefficient of $\beta = 0.1$. It can be noticed from this figure that the general manner of spreading remains unchanged and the droplet oscillates as it spreads on to the surface, similar to the case where $\beta = 0$. However, in contrast to the no-slip case, with a fixed contact angle and a finite slip velocity, the droplet eventually attains perfect equilibrium, as the contact point moves (slowly, in this case) to meet the condition where the dynamic contact angle (θ) becomes equal to the static contact angle (θ_s). The relative magnitude of the slip velocity at the contact point determines the rate at which the droplet reaches steady state conditions.

Figure 5.32(a) shows the velocity field of the fluid near the contact point at time $t = 2.5$ as the droplet deforms while spreading onto the surface. At a subsequent time, $t = 7.5$, a recirculation is induced at the contact point as the slip velocity affects the local flow conditions (Fig. 5.32(b)). This recirculation is seen for all tested values of β, including the no-slip case ($\beta = 0$). The effect of the slip velocity in the contact region persists even as the droplet begins to move away from the surface (Fig. 5.32(c) at time, $t = 9.5$) and also, as it spreads back towards the surface at a later time (Fig. 5.32(d) at $t = 13.0$). The streamline patterns in the pictures illustrate the effect of the finite slip in causing motion near the contact point which is different from that of the fluid in the rest of the droplet. It can be concluded, from this example, that a slip coefficient of $\beta = 0.1$ is too low for a droplet (with $Ca = 1.0$ and $Re = 5.0$) to attain a static contact angle of 160°. In this case, an angle of approximately 156° was reached.

Figure 5.33 illustrates the effect of a higher slip coefficient ($\beta = 1.0$) on the spreading of the droplet. Similar to the previous case, the overall dynamics of spreading remain unchanged while the flow field near the contact point shows distinct differences. Figure 5.33(a), which corresponds to time, $t = 2.0$, shows the velocity field of the droplet as it initially spreads onto the solid surface. The higher slip coefficient causes a greater outward slip velocity at the contact point. A recirculation, similar to the previous case, occurs in the neighborhood as the droplet begins to oscillate and reverses the direction of velocity (Fig. 5.33(b)). However, instead of diminishing and eventually disappearing, the recirculation region increases in extent due to a stronger slip at the contact point, even as the droplet spreads back towards the surface (Fig. 5.33(c)). Soon, an instability begins to form in the droplet and the recirculation affects larger parts of the drop (Fig. 5.33(d) at time $t = 11.5$). The streamline patterns in the figure show a clear evidence of the formation of the instability and erratic recirculation which causes the near-steady-state flow in the upper part of the droplet to become unstable as well. Eventually, the instability can be observed near the top point of the droplet, as is apparent from Fig. 5.34, which shows the variation of the velocity of the top point with time. The arrow in the figure the indicates the point where the fluid at the top point becomes unstable. This instability is due to the unrealistic physics that is being forced by the high value of β and is not an artifact of the numerical simulation.

The extreme behavior of the droplet in the above two cases suggests an intermediate figure to be a more appropriate value for the slip coefficient. Thus, the case of $\beta = 0.5$ was investigated and the results are presented below.

Figure 5.35 shows a sequence of velocity fields of the resulting manner of spreading of a droplet with a slip coefficient of $\beta = 0.5$. Here, too, the general mode of spreading is not affected, while the appropriateness of an intermediate value of the slip coefficient is apparent, both in terms of stable velocity fields and values of θ being closer to θ_s. Figure 5.35(a) shows an enlarged view of the flow field near the contact point as the droplet begins to spread towards the surface at time, $t = 3.5$. At a later time ($t = 5.5$), the now-familiar stable recirculation appears at the contact point (Fig. 5.35(b)). Even as the motion of the droplet towards the surface slows down, the local motion of the contact point affects the flow field in the neighboring region and the free surface continues to move outwards, aiding the spreading process. Figure 5.35(c) corresponds to an instant when the droplet reverses the direction of its velocity at time, $t = 9.5$. Interestingly, at this point, the fluid everywhere in the droplet moves away from the surface and there is no unusual movement near the contact point, unlike in the previous cases. The stability of the drop is retained and the velocity of the contact point matches in order of magnitude, to that of the fluid in the rest of the droplet (Fig. 5.35(d)). In this case, the streamlines of the fluid indicate a more uniform and stable flow pattern in the droplet, which we believe to be more physical than for the previous values of β. The recirculation near the contact point in frame (d) is stable and occurs due to velocity reversal in the local region, as can be deduced from a quick look at frame (c).

Stronger evidence of the effect of the varying slip coefficient on the motion of the contact point and its effect on the local dynamics can be obtained by examining the trend of the dynamic contact angle shown in Fig. 5.36, which corresponds to $\beta = 0.1$, $\beta = 1.0$ and $\beta = 0.5$, as indicated in the figure. The irregularity in the initial stages is due to the dynamic change of the contact point, as frequent computational points come in contact with the surface. The velocity of the contact point varies as the droplet deforms, affecting the dynamic contact angle, which in turn prescribes the slip velocity. After a sufficiently long time, the droplet begins to attain the prescribed static contact angle, θ_s, but only for a value of $\beta = 0.5$.

The rate at which the droplet attains the static contact angle depends on the value of the slip coefficient. In the case of $\beta = 0.1$, since the slip velocity is very small, the process is very slow and takes a long time. However, for a much larger value of the slip coefficient ($\beta = 1.0$), as discussed earlier, an instability begins to appear which results in very high values of the slip velocity and the dynamic contact angle, θ. In this case, the dynamic contact angle attains unrealistic values of up to 180° as the droplet goes unstable, as indicated by the spikes in the figure after a sufficiently long time. Finally, for a value of $\beta = 0.5$ for the slip coefficient, as can be seen from Fig. 5.36, the change in the slip velocity and the dynamic contact angle is stable and more regular than for the previous cases, as can be noticed from a comparison of the three plots in the figure.

Figure 5.37 shows the effect of β on the overall shape of the droplet as it spreads on the solid surface. At early instances in time (Figs. 5.37(a), (b) and (c)), the difference in shapes between $\beta = 0.5$ and all other values ($\beta = 0$, $\beta = 0.1$, $\beta = 1.0$) is very significant while at later instances, as the droplet spreads more on the solid surface, the droplet shapes are more comparable. These figures suggest that when $\beta = 0.5$, the effect of the slip velocity is better felt in the bulk of the fluid and is not localized near the contact point, like in the other cases. This ensures that the droplet attains the prescribed static contact angle effectively, without any instability or unnatural local variations in the velocity of the fluid in the droplet.

This suggests that $\beta = 0.5$ is a reasonable value for the slip coefficient, even though the attainment of equilibrium is not very much faster than when β was equal to a value of 0.1. The exact value, though, will have to be determined experimentally, for lack of a definite mathematical manner of quantifying the amount of slip between a liquid and a solid substrate.

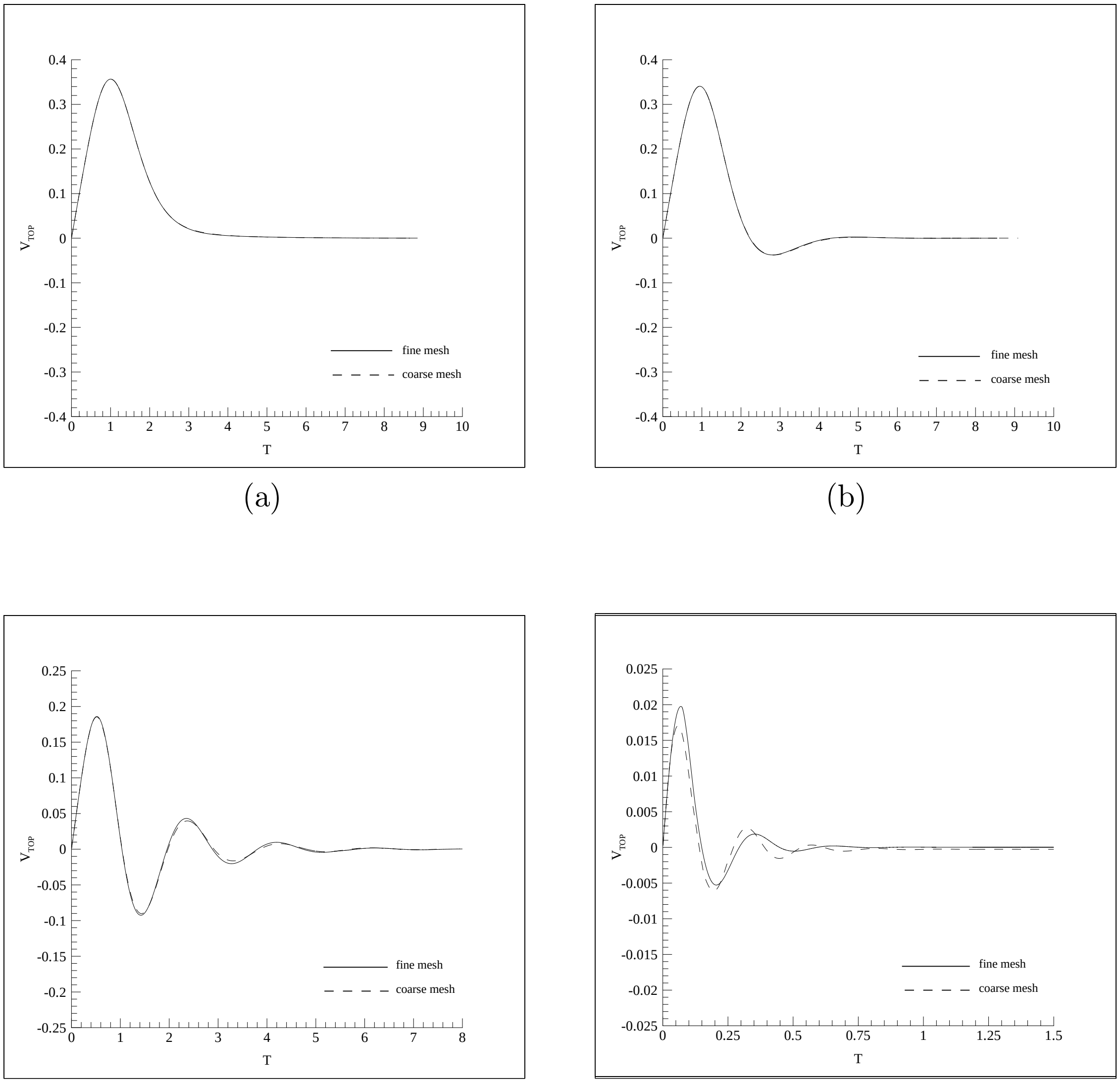

(a) (b)

(c) (d)

Figure 5.1: Demonstration of the independence of the results of spatial discretization : comparison of the velocity of the top point (for droplet spreading on a plane surface) using the coarse and fine meshes for : (a)$Ca = 2.0$ & $Re = 1.0$, (b)$Ca = 1.0$ & $Re = 1.0$, (c)$Ca = 0.2$ & $Re = 0.5$, (d)$Ca = 0.1$ & $Re = 0.01$. The solid line corresponds to the fine mesh, while the dashed line refers to the coarse mesh.

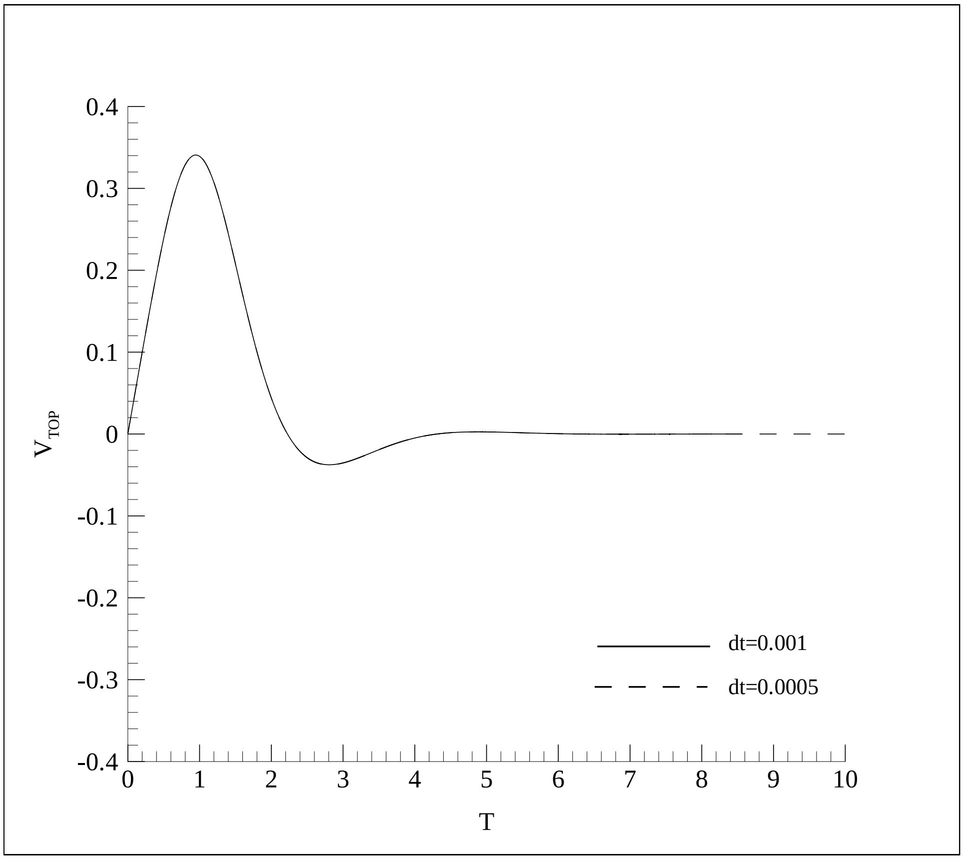

Figure 5.2: Demonstration of the independence of the results of temporal discretization : comparison of the velocity of the top point (for droplet spreading on a plane surface) for time steps of $dt = 0.001$ and $dt = 0.0005$, with $Ca = 1.0$ and $Re = 1.0$. The solid line corresponds to the larger time step, while the dashed line corresponds to the smaller time step.

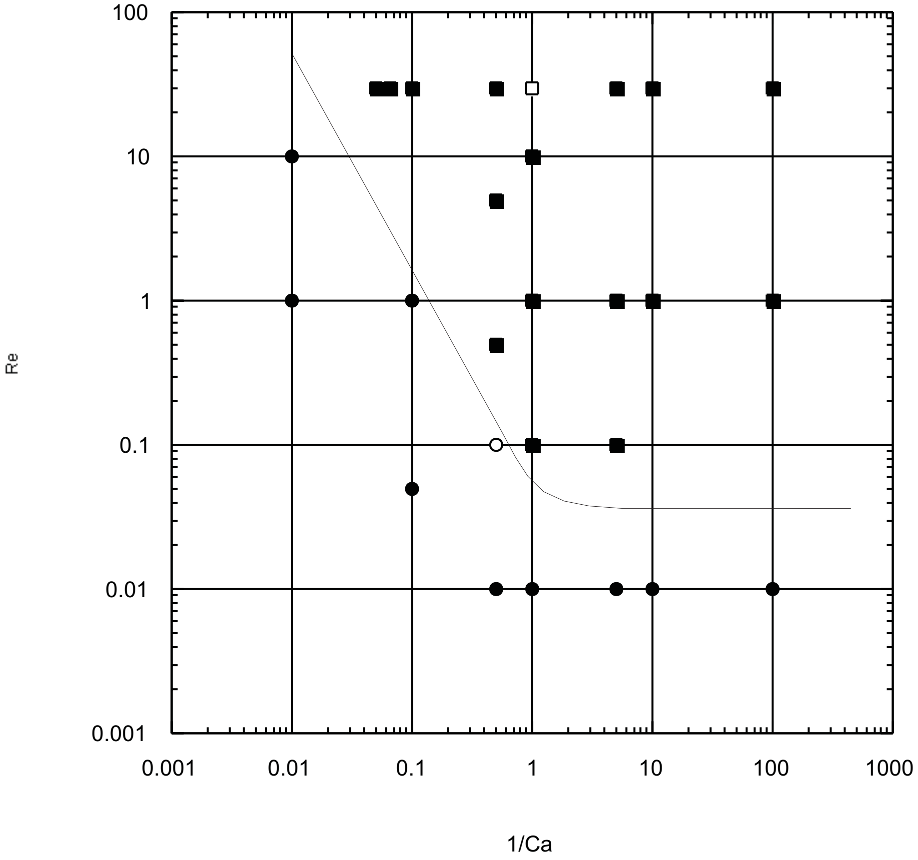

Figure 5.3: Stability map for the two-drop case : with *Re* and *Ca* as control parameters. ●-stable behavior; ■-unstable behavior. The hollow symbols (○ and □) represent the cases discussed in detail. The solid line is the estimated boundary between the different regimes.

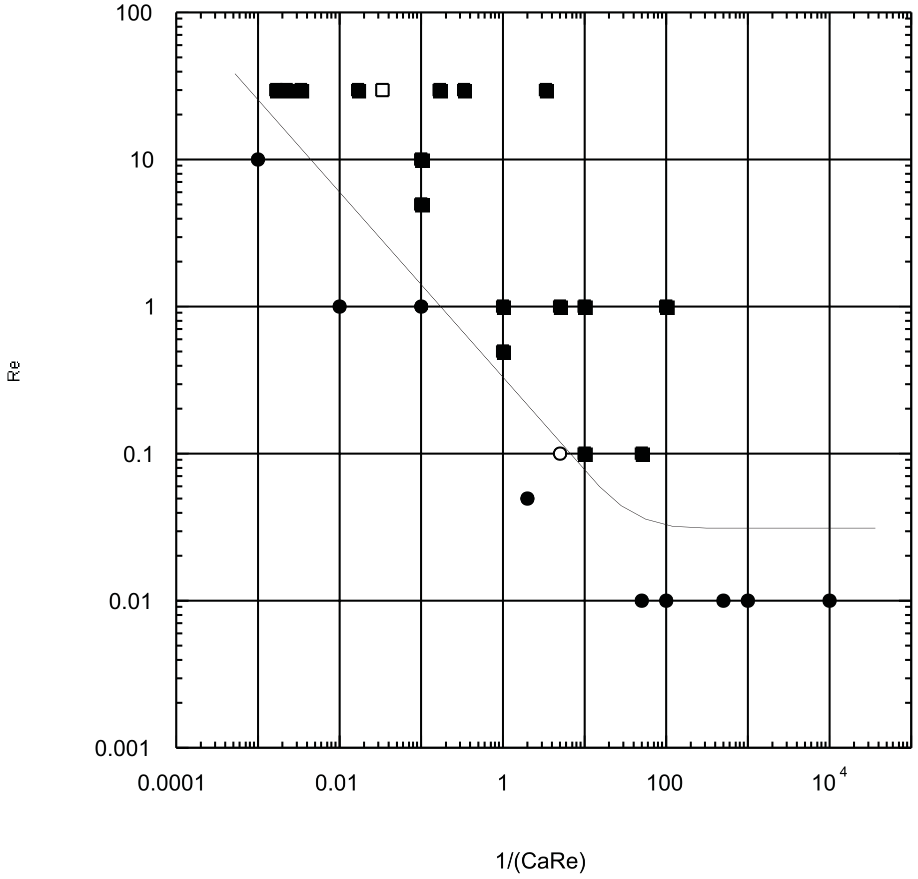

Figure 5.4: Stability map for the two-drop case showing the effect of surface tension on the abscissa and that of viscosity on the ordinate. ●-stable behavior; ■-unstable behavior. The hollow symbols (○ and □) represent the cases discussed in detail. The solid line is the estimated boundary between the different regimes.

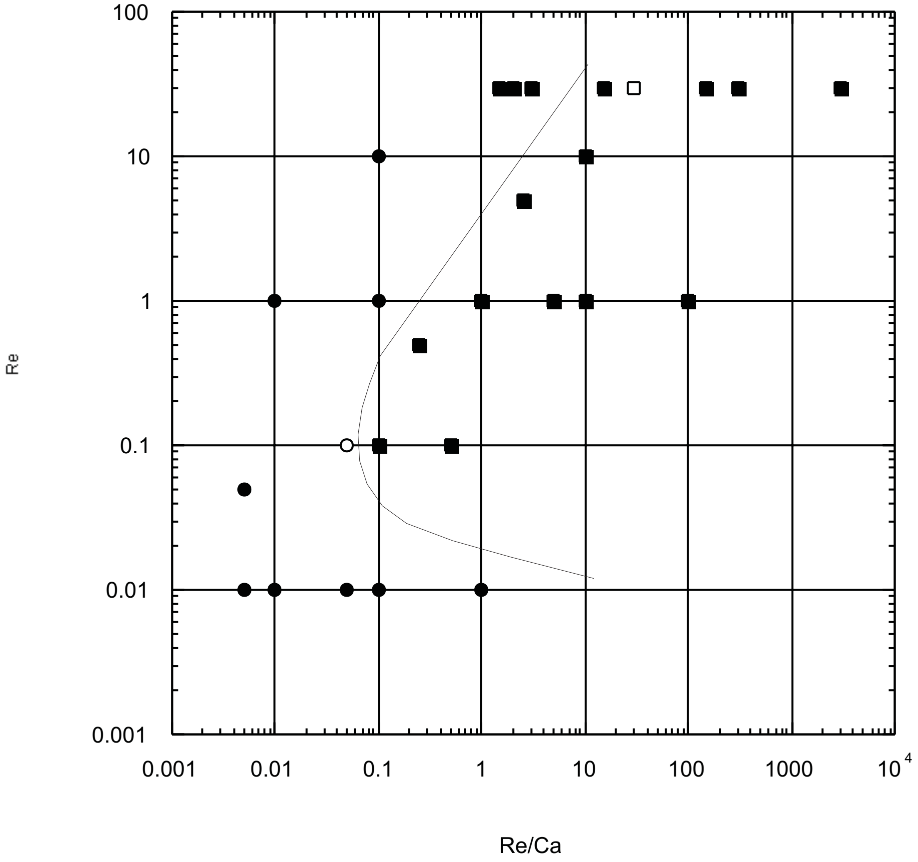

Figure 5.5: Stability map for the two-drop case showing the effect of surface tension on the abscissa and that of gravity on the ordinate. ●-stable behavior; ■-unstable behavior. The hollow symbols (○ and □) represent the cases discussed in detail. The solid line is the estimated boundary between the different regimes.

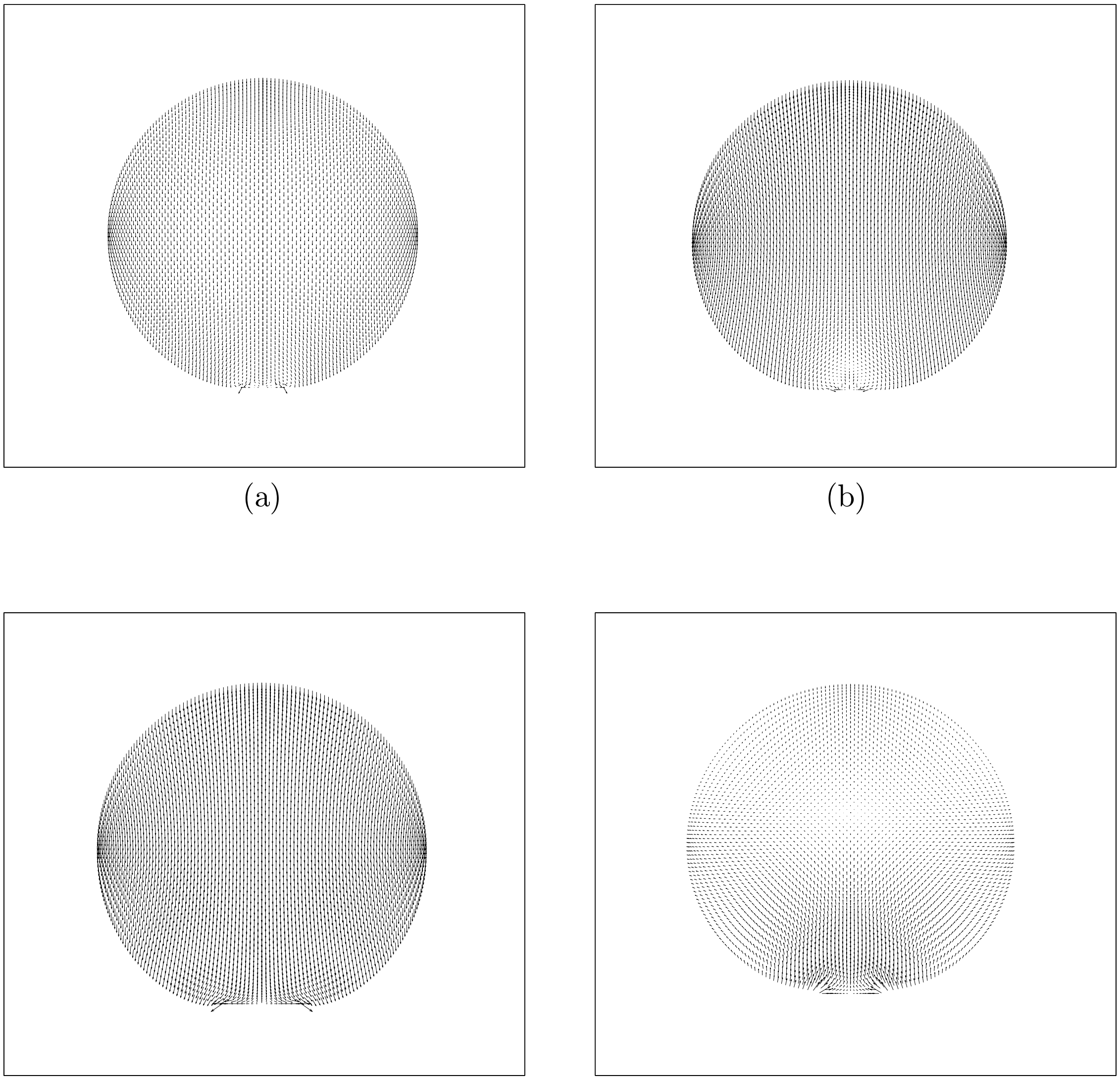

(a) (b) (c) (d)

Figure 5.6: Typical behavior of a stable droplet, for the two-drop case, with $Ca = 2.0$ & $Re = 0.1$, at progressive instances of (non-dimensional) time : (a) t=0.075, (b) t=0.325, (c) t=0.575 and (d) t=1.29757. Note : The vectors in this figure have their tail at the node location.

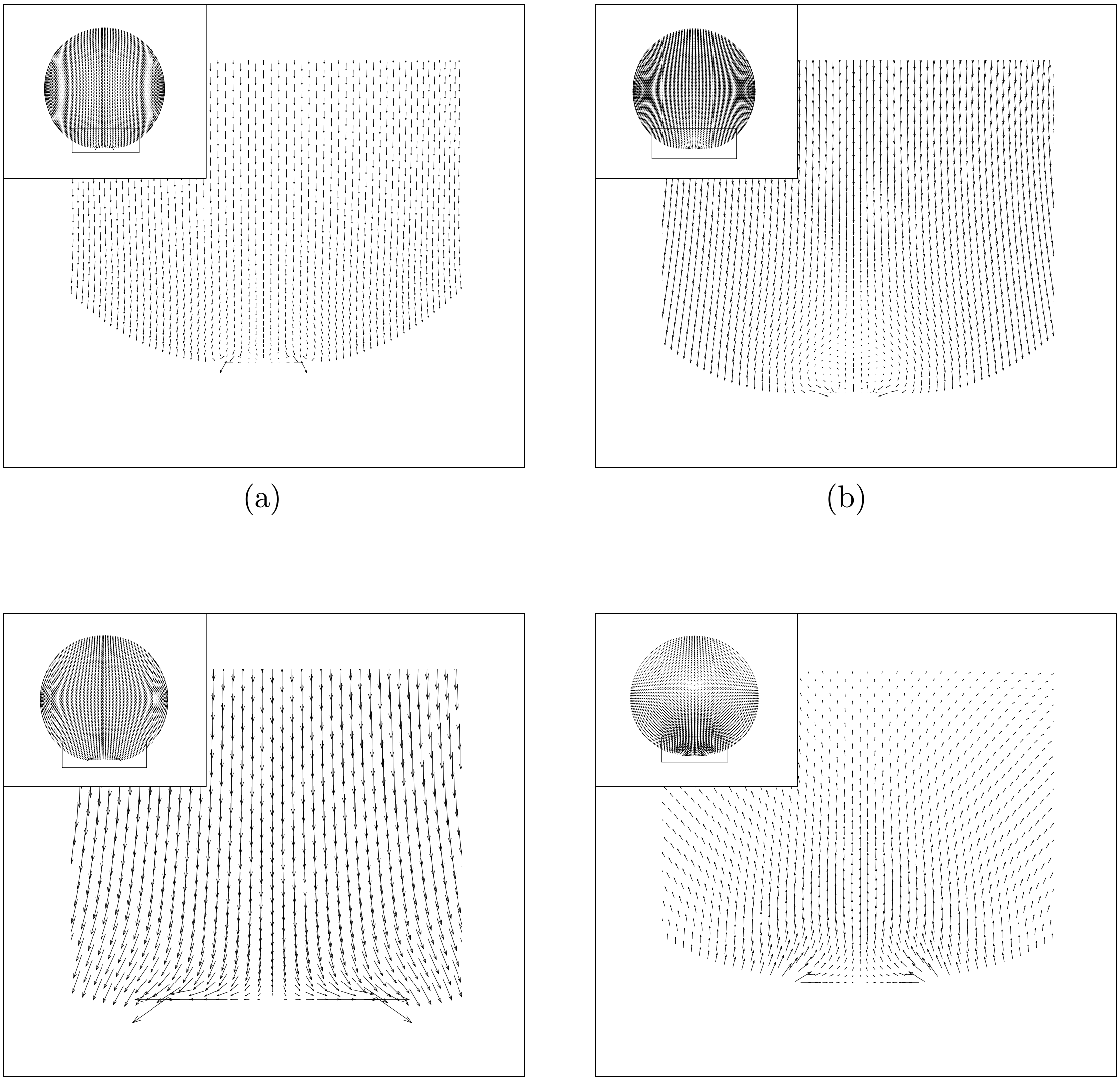
(a)
(b)
(c)
(d)

Figure 5.7: Contact point motion of the stable droplet, for the two-drop case, with $Ca = 2.0$ & $Re = 0.1$, at progressive instances of (non-dimensional) time : (a) t=0.075, (b) t=0.325, (c) t=0.575 and (d) t=1.29757.

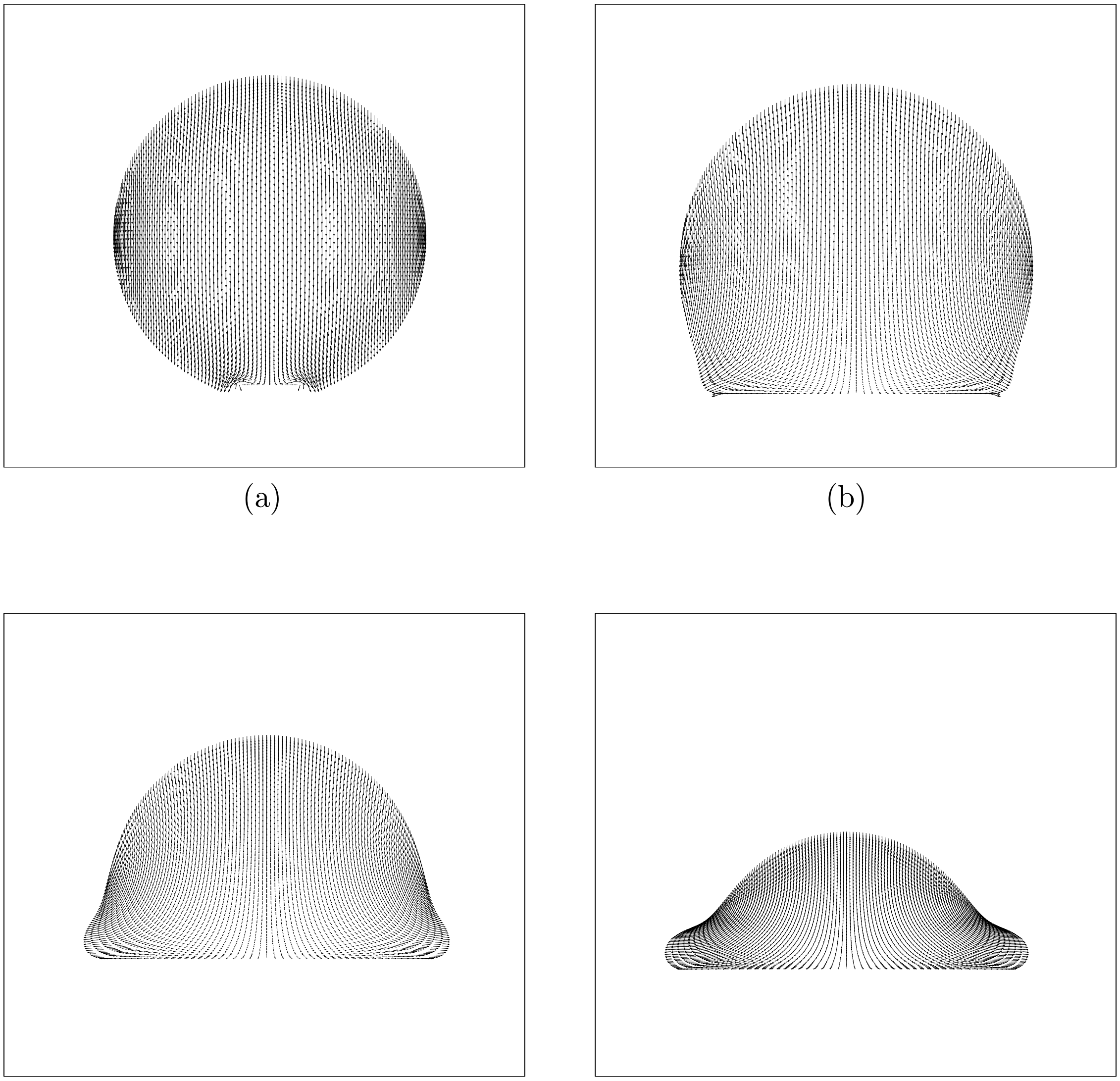

(a) (b)

(c) (d)

Figure 5.8: Typical behavior of the unstable droplet, for the two-drop case, with $Ca = 1.0$ & $Re = 30.0$, at progressive instances of (non-dimensional) time : (a) t=0.23973, (b) t=0.95973, (c) t= 1.43973 and (d) t=1.89775.

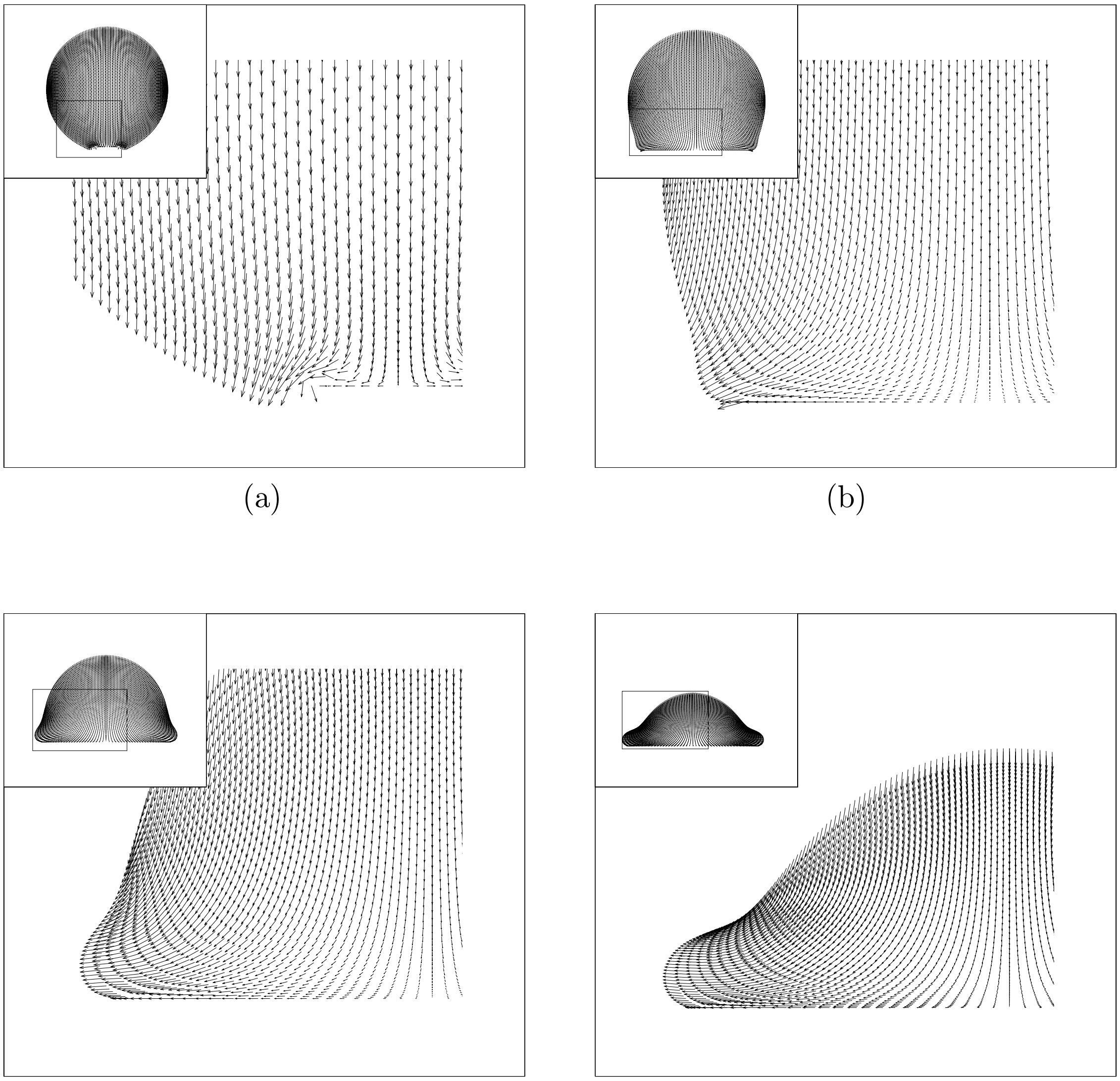

(a) (b)

(c) (d)

Figure 5.9: Contact point motion of the unstable droplet, for the two-drop case, with Ca = 1.0 & Re = 30.0, at progressive instances of (non-dimensional) time : (a) t=0.23973, (b) t=0.95973, (c) t= 1.43973 and (d) t=1.89775.

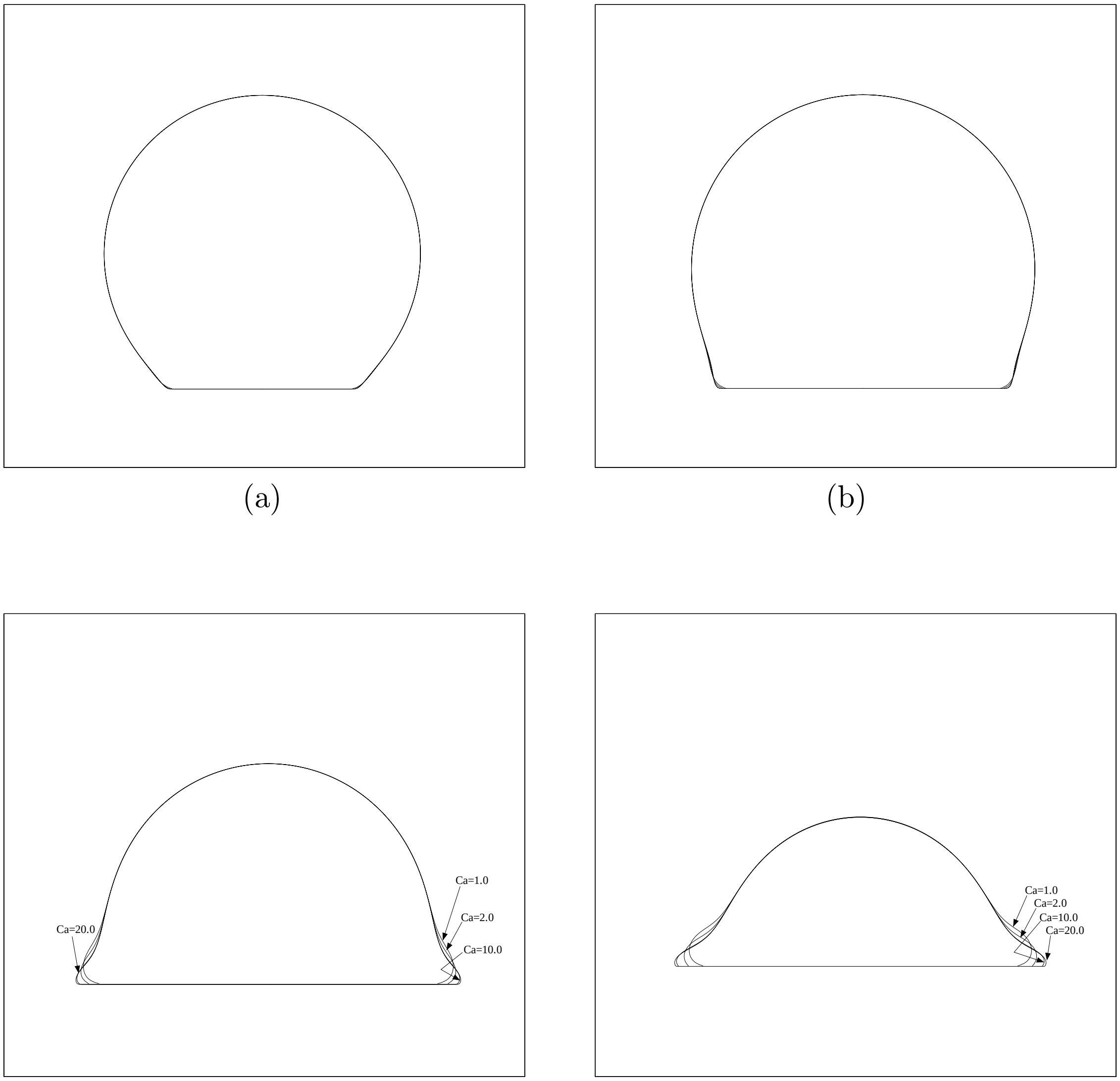

(a) (b)

(c) (d)

Figure 5.10: Comparison of droplet shapes, for the two-drop case, with fixed Reynolds number ($Re = 30.0$) and variable capillary number ($Ca = 1.0, 2.0, 10.0, 20.0$) at different (non-dimensional) times : (a) t=0.75, (b) t=1.05, (c) t=1.5 and (d) t=1.8.

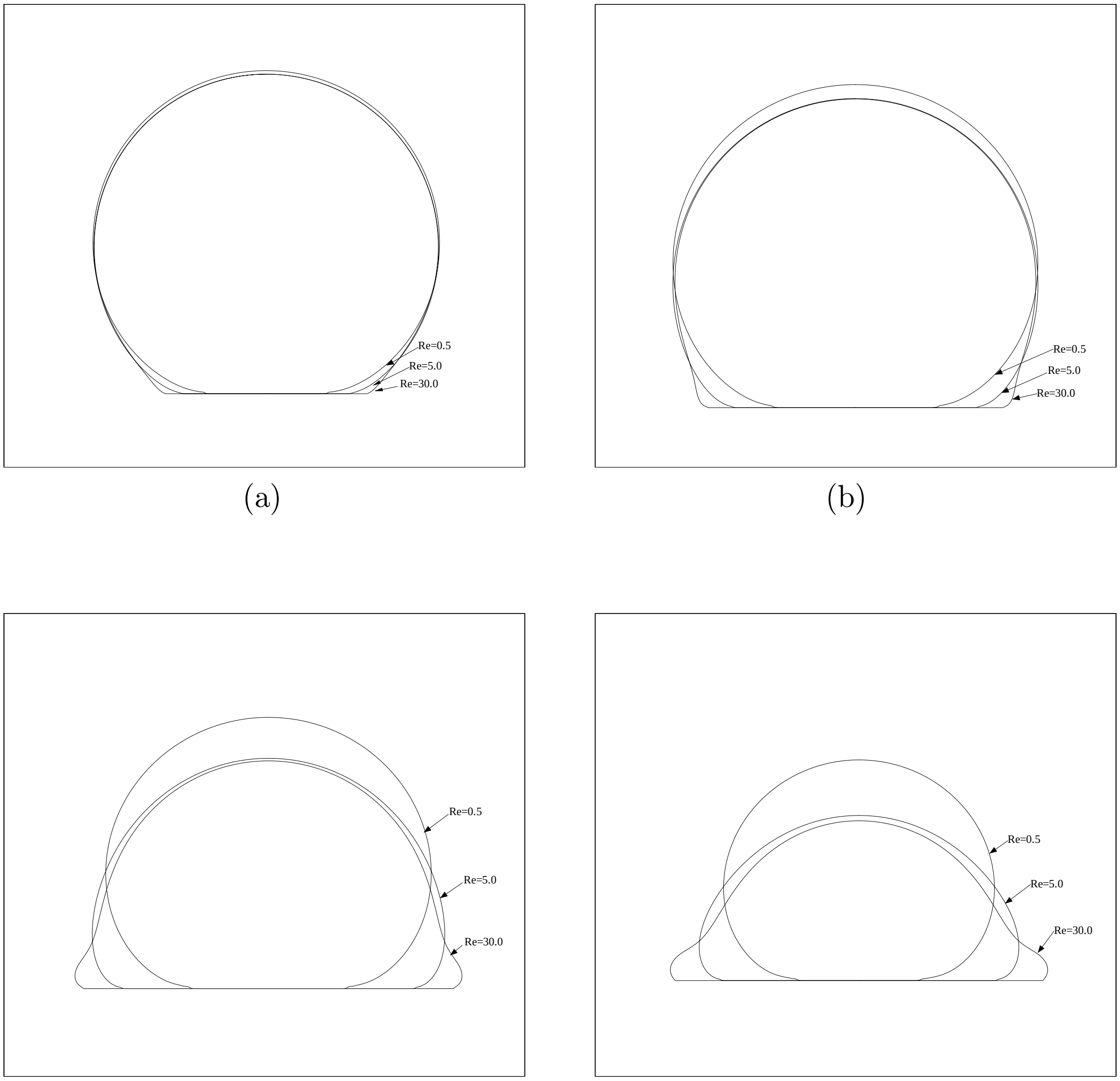

(a) (b)

(c) (d)

Figure 5.11: Comparison of droplet shapes, for the two-drop case, with fixed capillary number ($Ca = 2.0$) and variable Reynolds number ($Re = 0.5, 5.0, 30.0$) at different (non-dimensional) times : (a) t=0.75, (b) t=1.05, (c) t=1.5 and (d) t=1.8.

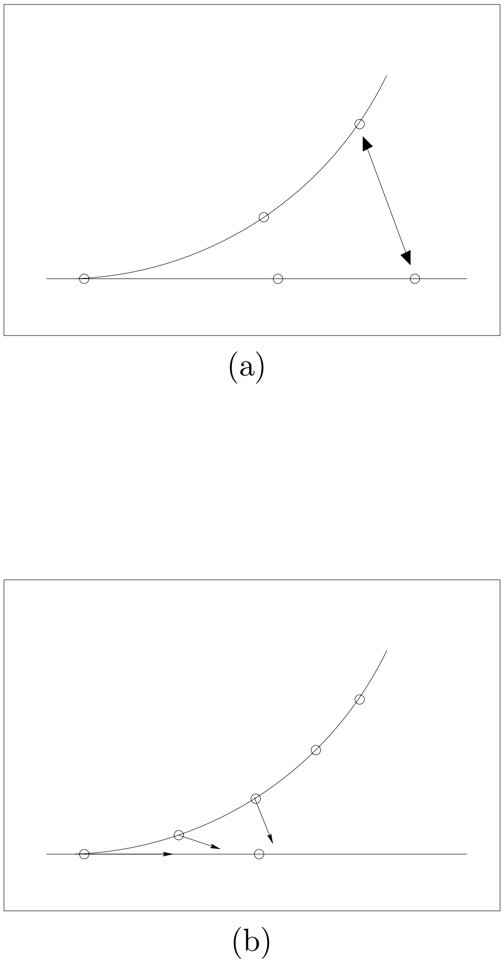

Figure 5.12: Assumptions in the modeling of a droplet spreading on a solid surface : (a) reversibility of fluid spreading (b) contact point motion due to the combined effect of the slip velocity and the motion of the neighboring material points.

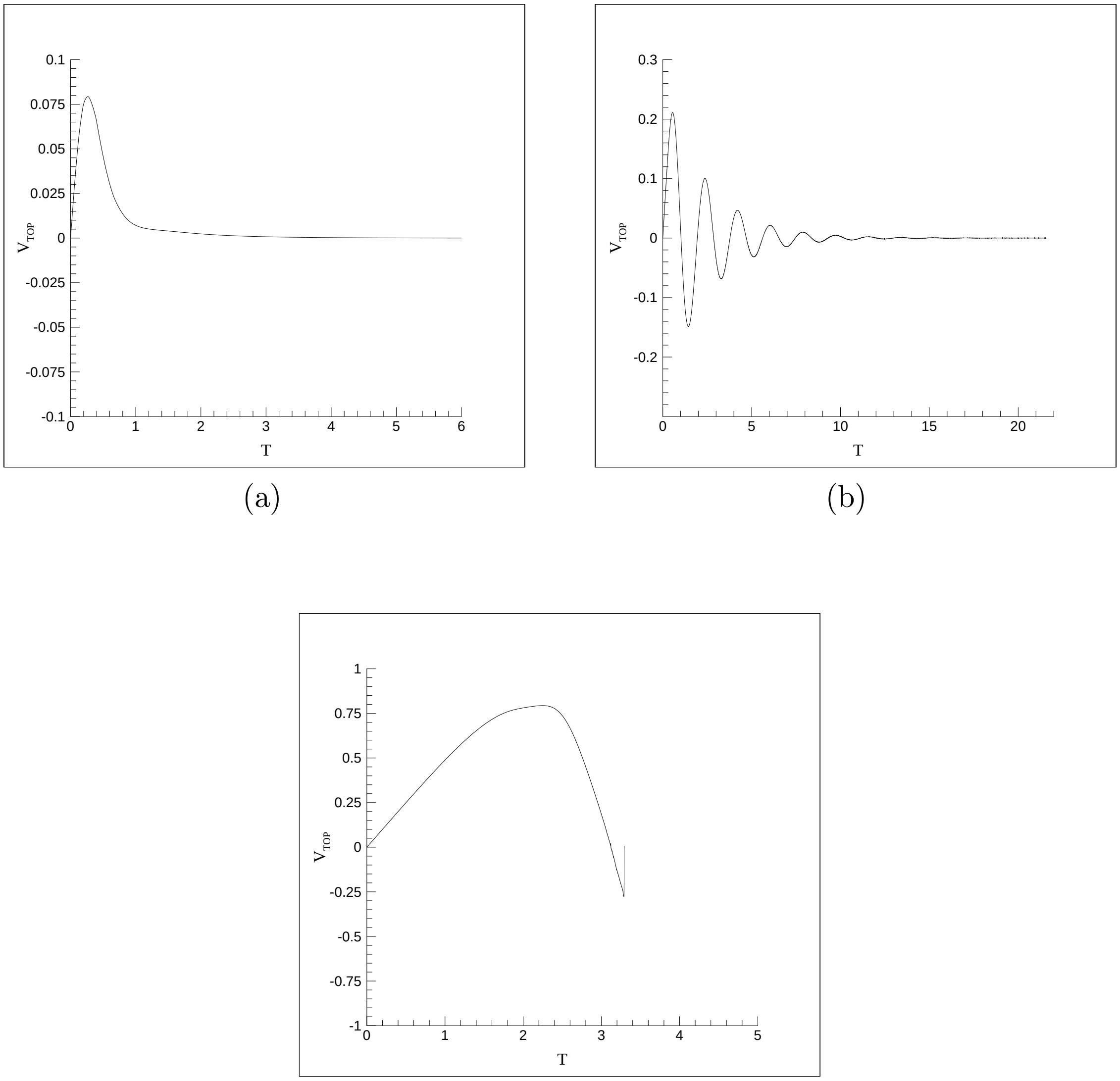

(a) (b)

(c)

Figure 5.13: Variation, with time, of the velocity of the top point, of a droplet spreading on a solid surface for (a) stable (b) oscillatory and (c) splashing behaviors (positive velocity represents motion of the droplet towards the surface).

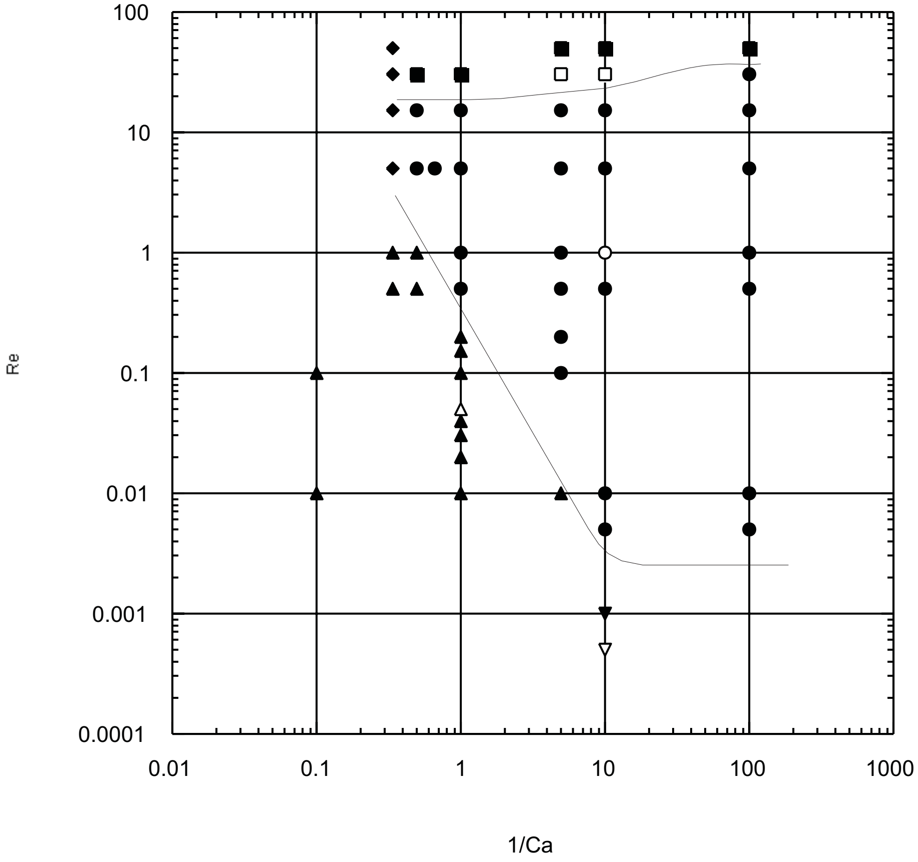

Figure 5.14: Stability map for a drop spreading on a solid surface, with no slip : with Re and Ca as the control parameters. ▲-stable spreading; •-oscillatory spreading; ■-splash; ▼-microgravity; ⧫-border between stable and oscillatory behaviors. The hollow symbols (△, ◦, □ and ▽) represent the cases discussed in detail. The curves represent the estimated boundaries between the different behaviors.

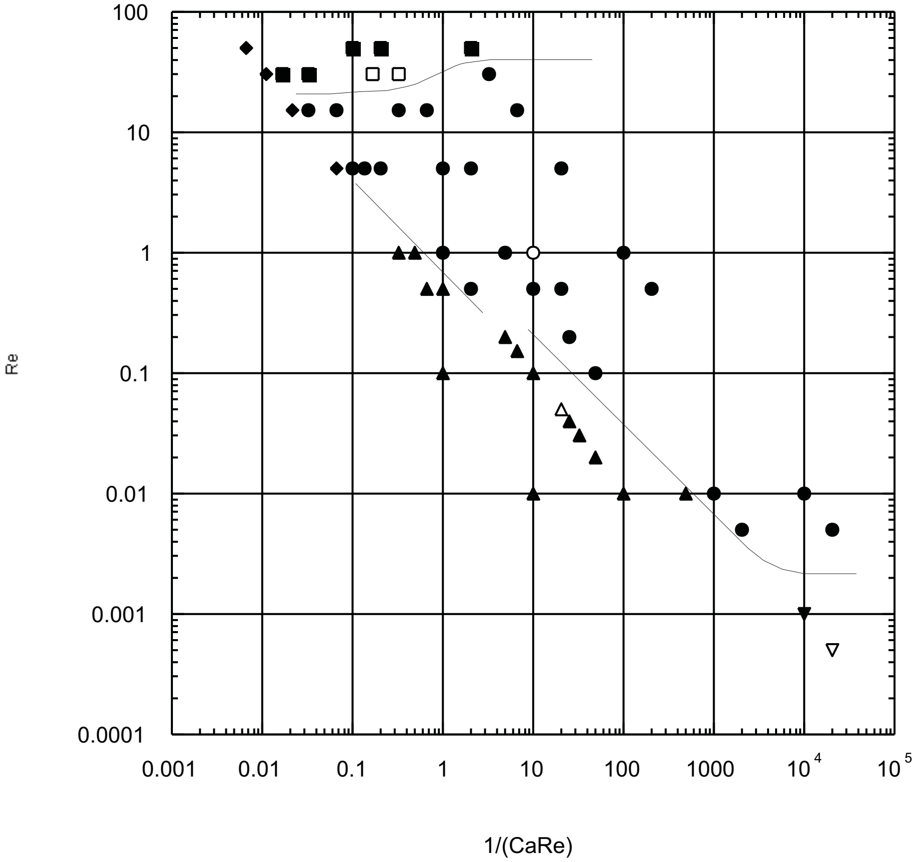

Figure 5.15: Stability map for a drop spreading on a solid surface showing the effect of surface tension on the abscissa and that of viscosity on the ordinate. ▲-stable spreading; ●-oscillatory spreading; ■-splash; ▼-microgravity; ◆-border between stable and oscillatory behaviors. The hollow symbols (△, ○, □ and ▽) represent the cases discussed in detail. The curves represent the estimated boundaries between the different behaviors.

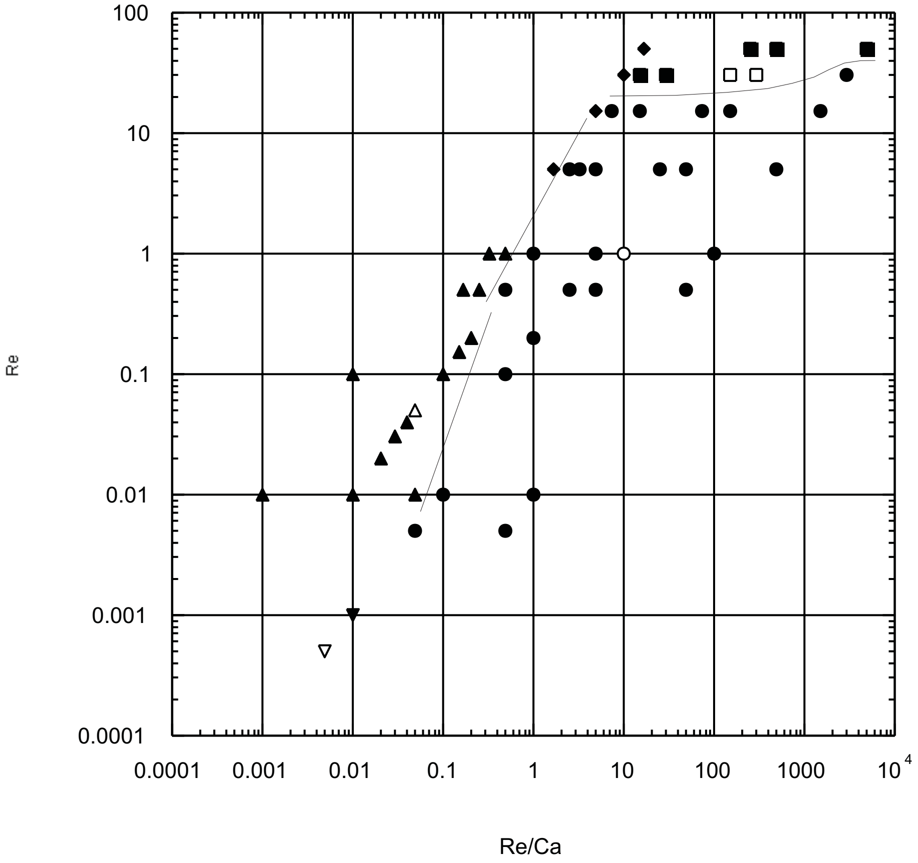

Figure 5.16: Stability map for a drop spreading on a solid surface showing the effect of surface tension on the abscissa and that of gravity on the ordinate. ▲-stable spreading; ●-oscillatory spreading; ■-splash; ▼-microgravity; ◆-border between stable and oscillatory behaviors. The hollow symbols (△, ○, □ and ▽) represent the cases discussed in detail. The curves represent the estimated boundaries between the different behaviors.

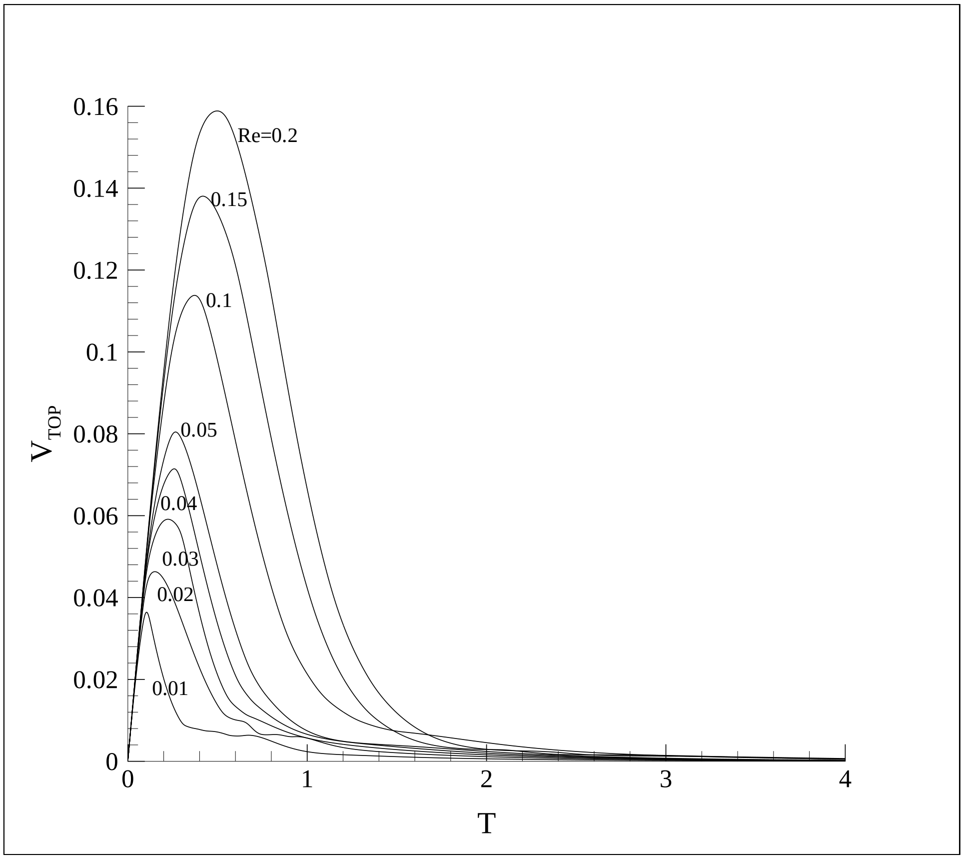

Figure 5.17: Time dependence of the velocity of the top point, of a stable droplet for a fixed capillary number ($Ca = 1.0$) and various Reynolds numbers ($Re = 0.01, 0.02, 0.03, 0.04, 0.05, 0.1, 0.15, 0.2$).

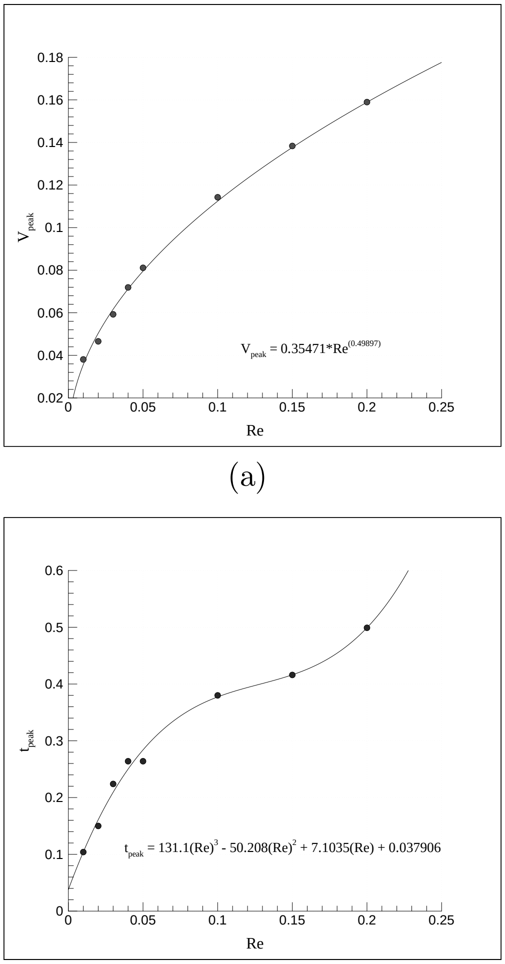

(a)

(b)

Figure 5.18: Variation of the (a) peak velocity and (b) peak time, with Re, for a droplet spreading in a stable manner, with capillary number fixed at $Ca = 1.0$. This figure refers to the results obtained in Fig. 5.17.

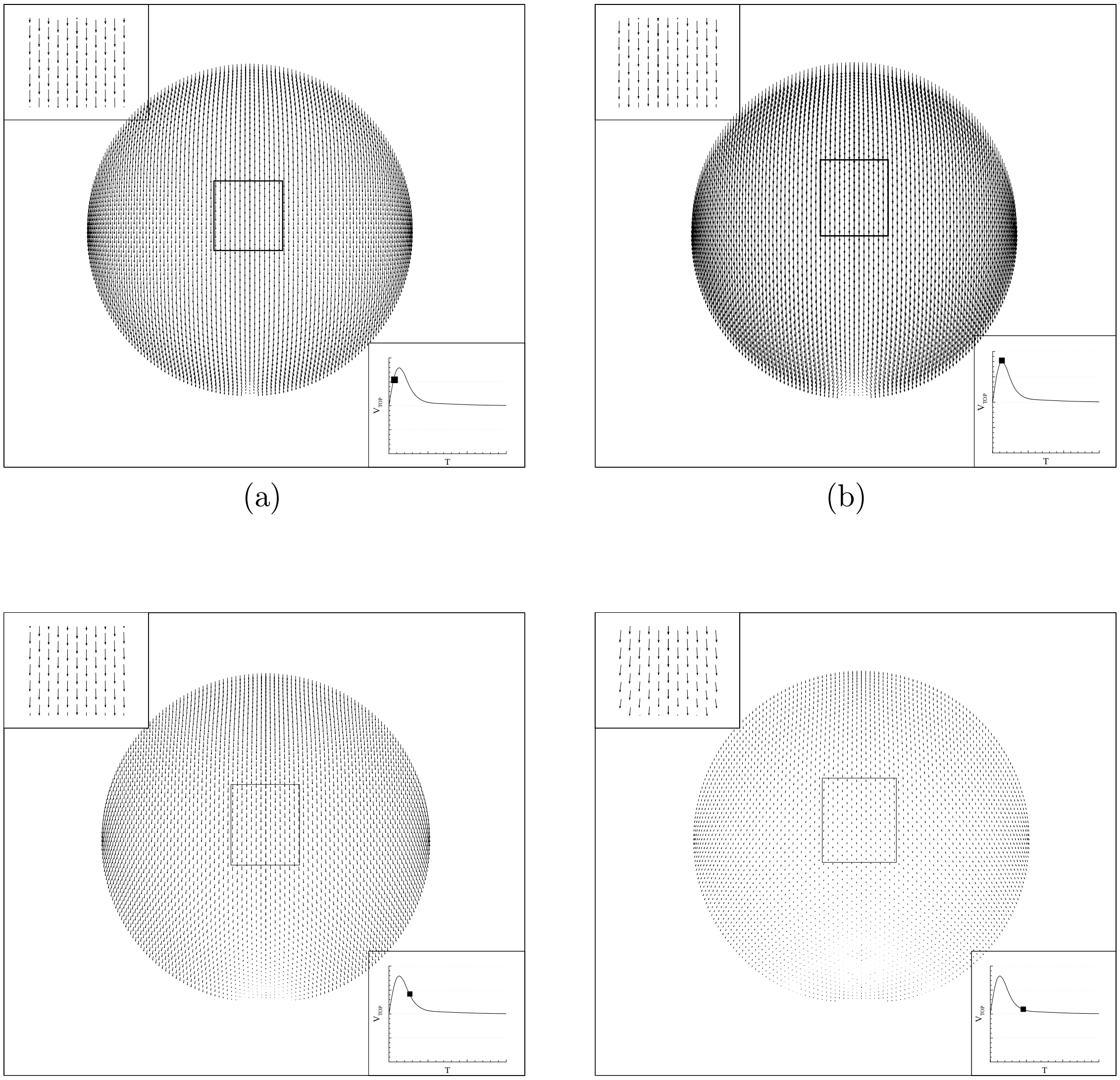

(a) (b) (c) (d)

Figure 5.19: Typical behavior of a stable droplet (spreading on a solid surface), with $Ca = 1.0$ & $Re = 0.05$ at progressive instances of (non-dimensional) time : (a) t=0.1, (b) t=0.25, (c) t=0.6 and (d)t=1.0. The inset in the top corner shows an enlarged view of the velocity field which corresponds to the hollow rectangle (in the middle of the droplet) while the inset in the bottom corner shows the variation of the top point velocity.

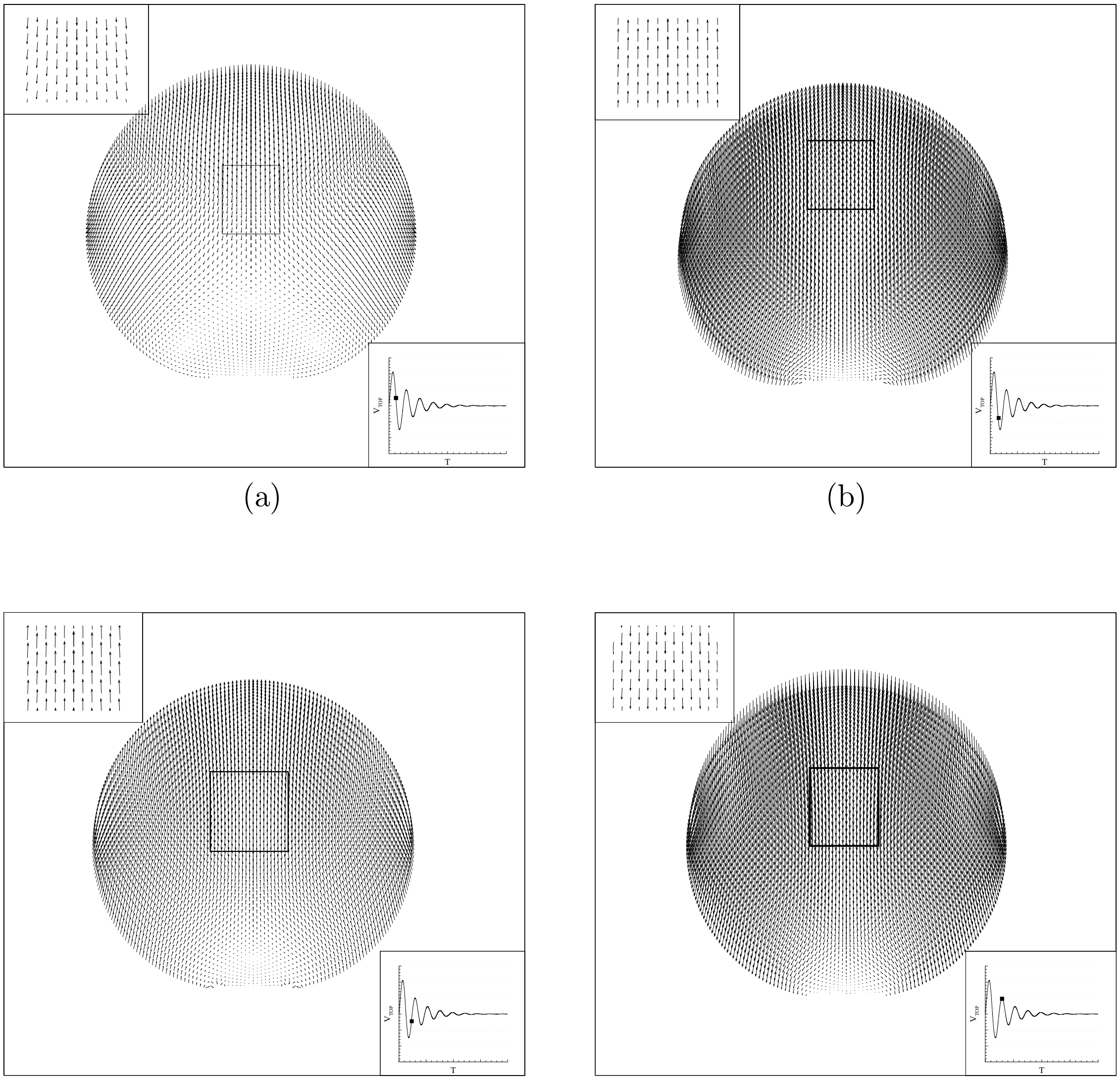

(a) (b)

(c) (d)

Figure 5.20: Typical behavior of an oscillating droplet (spreading on a solid surface), with $Ca = 0.1$ & $Re = 1.0$ at progressive instances of (non-dimensional) time : (a) t=0.9874, (b) t=1.247, (c) t=1.8364 and (d) t=2.3383. The inset in the top corner shows an enlarged view of the velocity field which corresponds to the hollow rectangle (in the middle of the droplet) while the inset in the bottom corner shows the variation of the top point velocity.

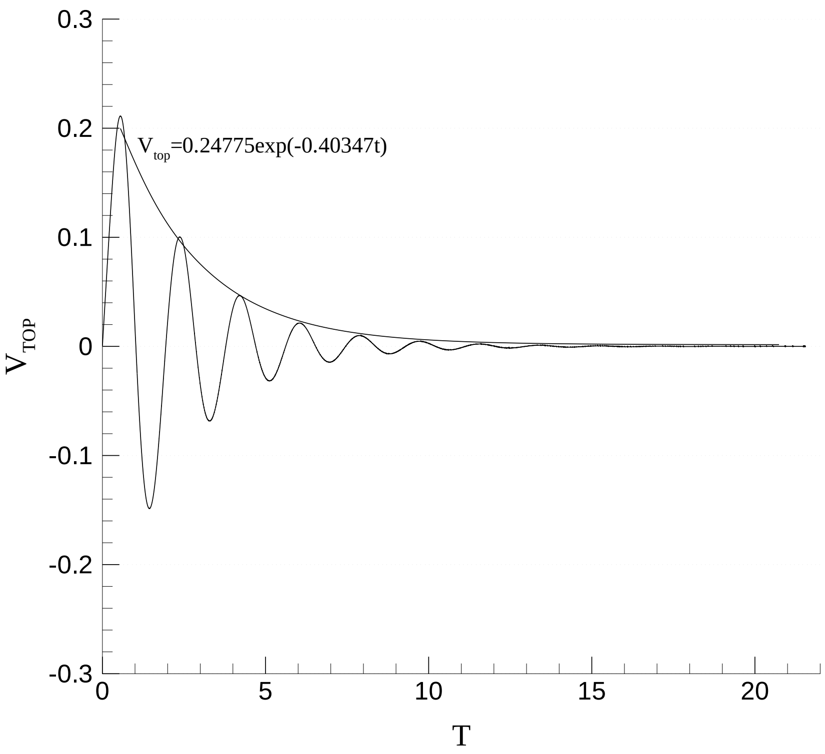

Figure 5.21: Exponential decay of the velocity of the top point for the oscillating droplet with $Ca = 0.1$ & $Re = 1.0$

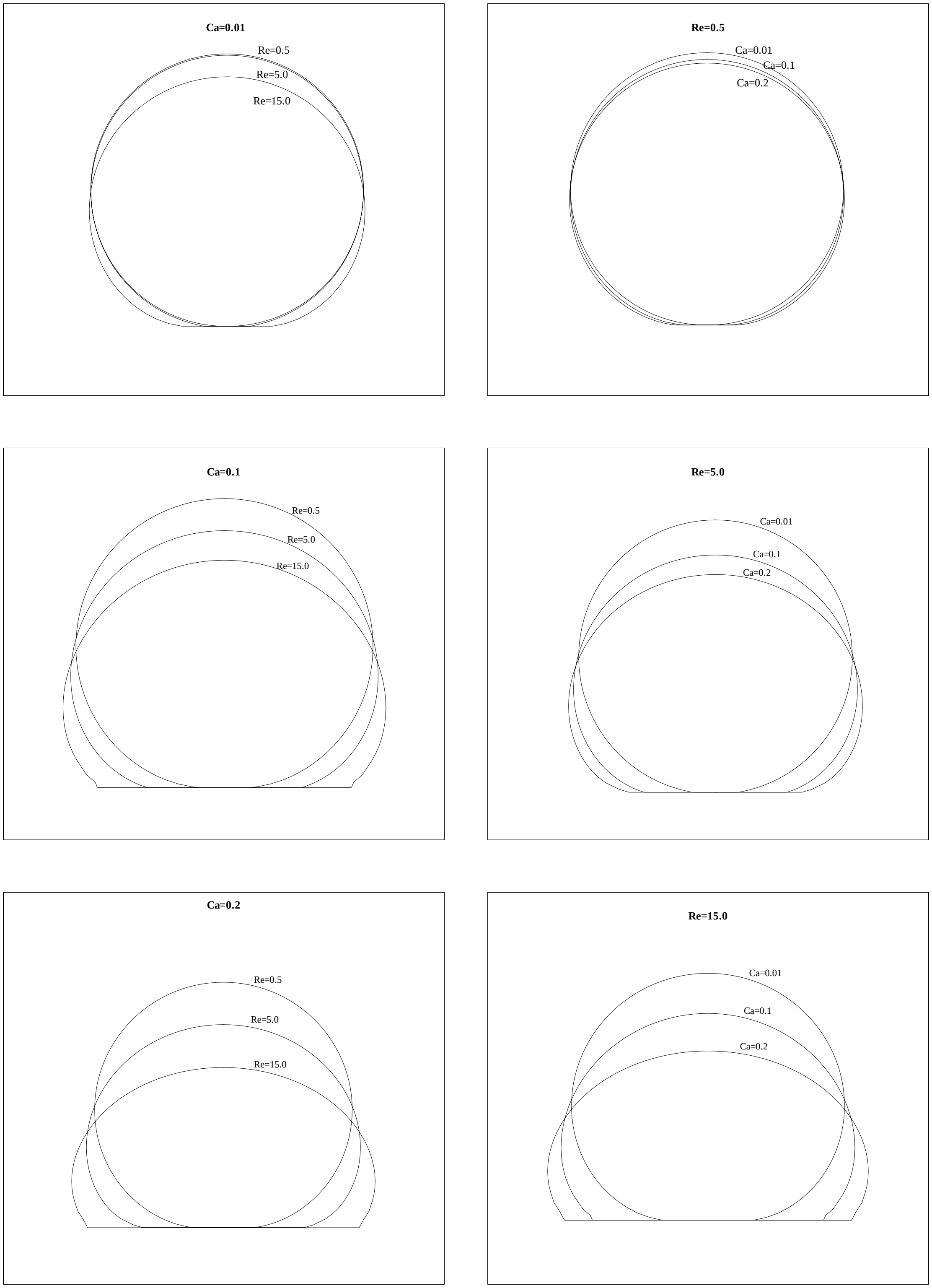

Figure 5.22: Settling shapes (profiles after a long time) for oscillating droplets (spreading on a solid surface).

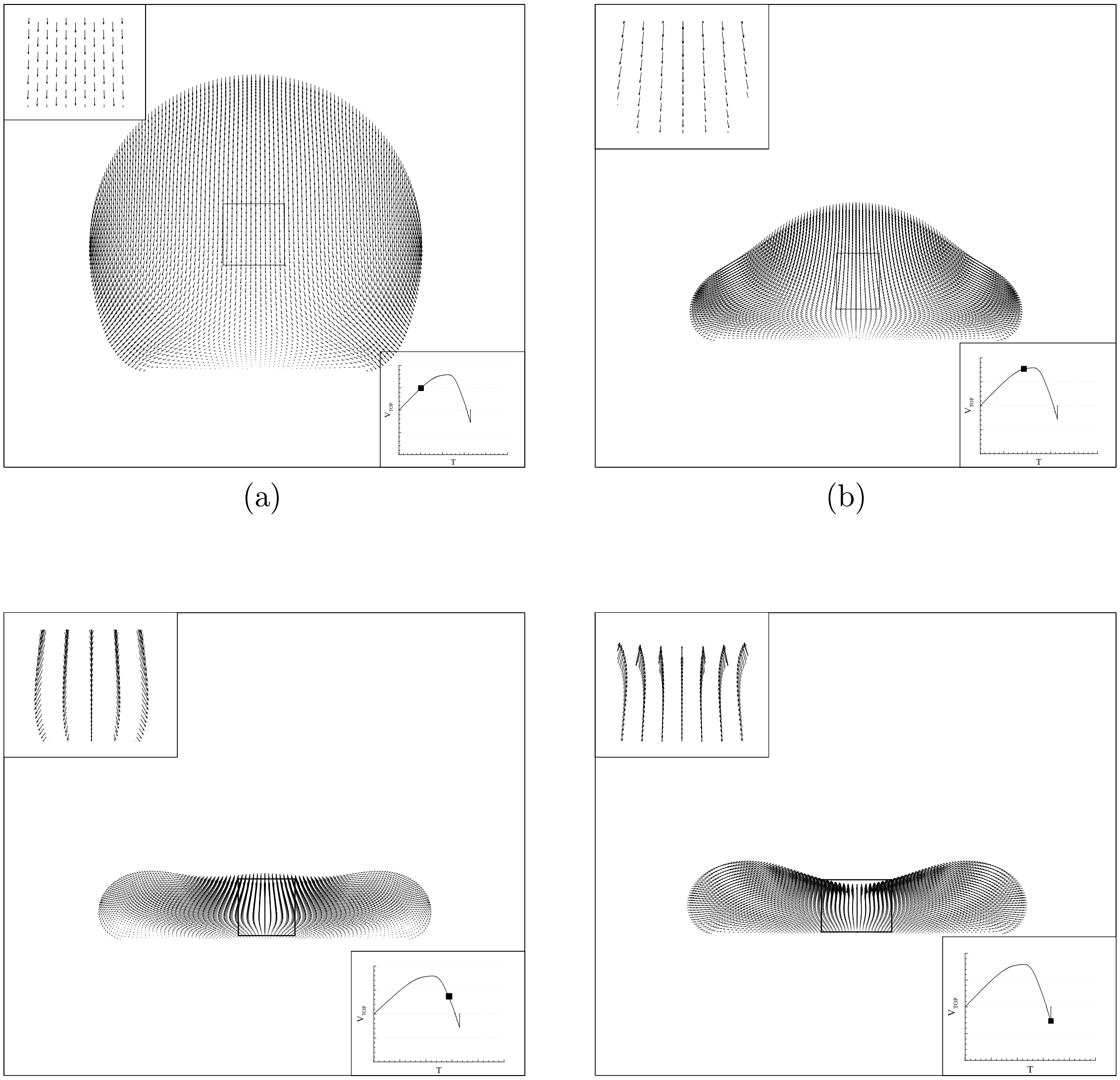

(a) (b)

(c) (d)

Figure 5.23: Typical behavior of a splashing droplet (spreading on a solid surface), with $Ca = 0.2$ & $Re = 30.0$ at progressive instances of (non-dimensional) time : (a) t=1.0, (b) t=2.0, (c) t=2.8 and (d) t=3.29. The inset in the top corner shows an enlarged view of the velocity field which corresponds to the hollow rectangle (in the middle of the droplet) while the inset in the bottom corner shows the variation of the top point velocity.

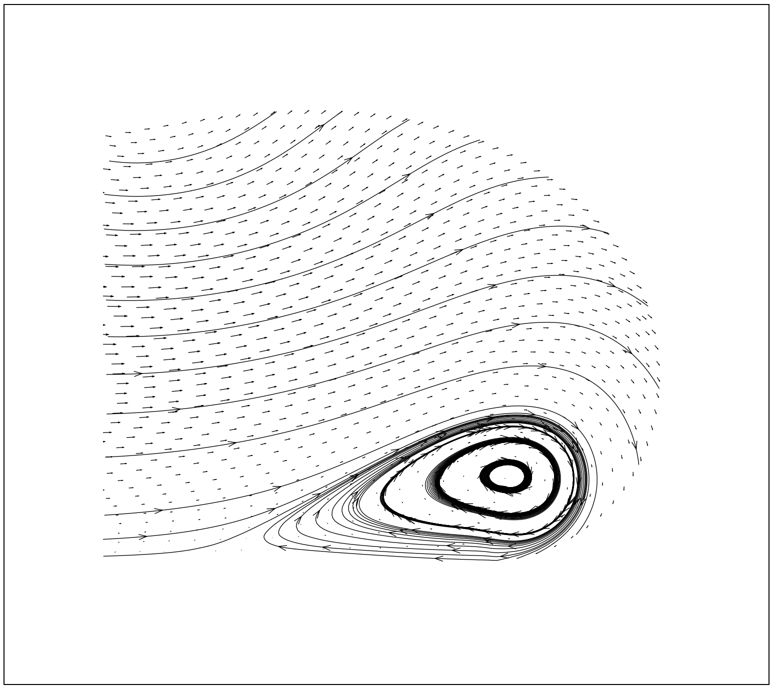

Figure 5.24: Recirculation induced near the contact point, for the case of a splashing droplet, at an instant before splashing (t=2.8); $Ca = 0.2$ & $Re = 30.0$.

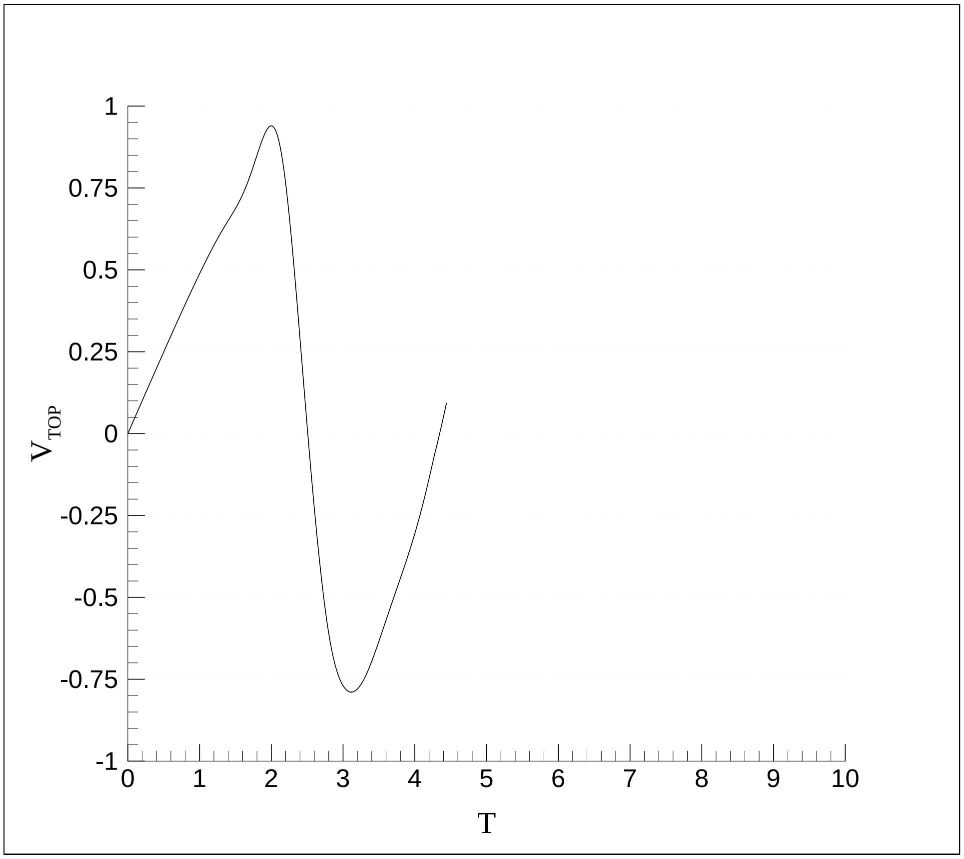

Figure 5.25: Time dependence of the velocity of the top point, for a special case of the splashing droplet : $Ca = 0.1$ & $Re = 30.0$.

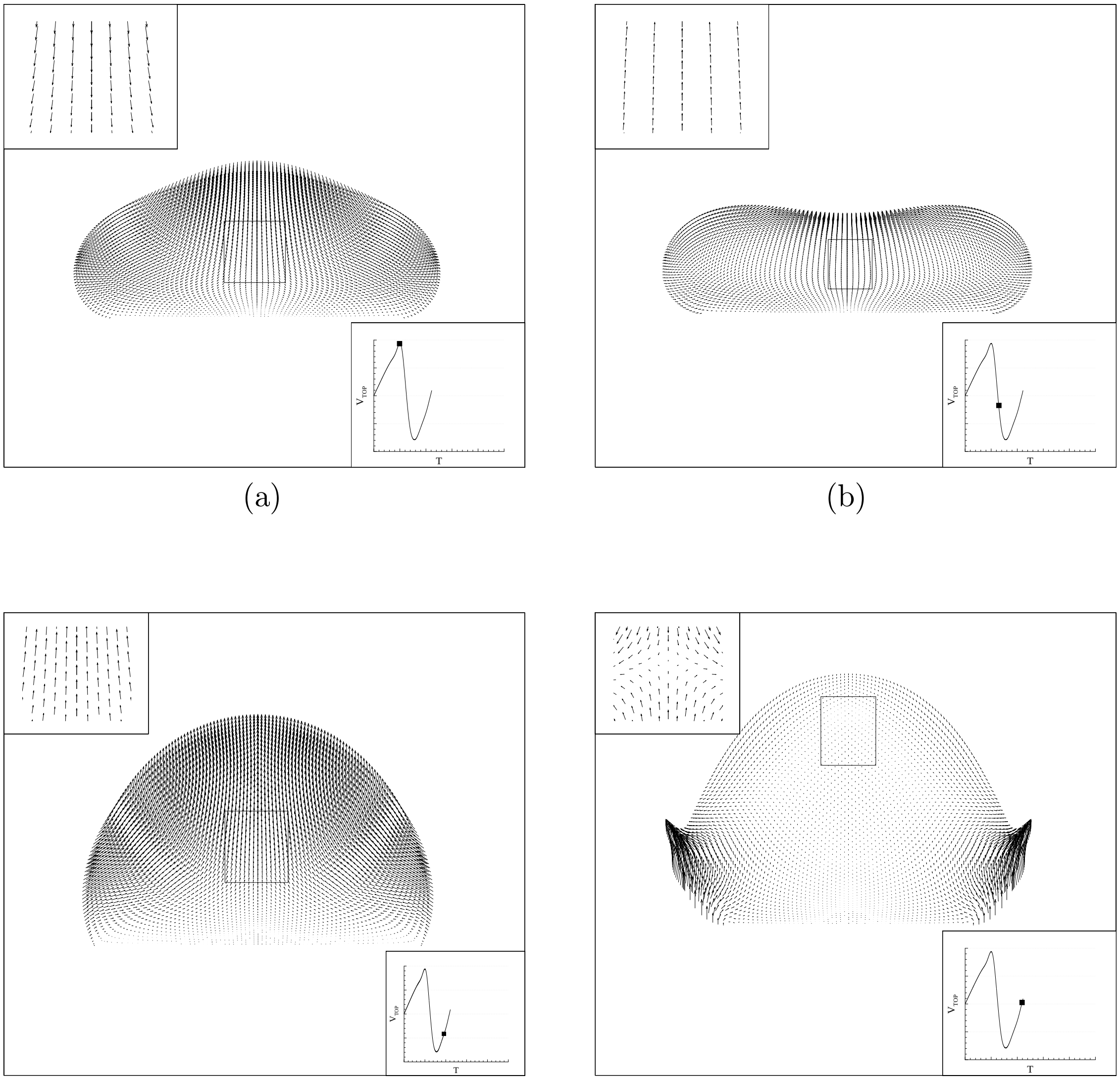

(a) (b)

(c) (d)

Figure 5.26: The formation of a crown (as a special case of a splashing droplet), with $Ca = 0.1$ & $Re = 30.0$ at progressive instances of (non-dimensional) time : (a) t=2.0, (b) t=2.6, (c) t=3.7991 and (d) t=4.39631. The inset in the top corner shows an enlarged view of the velocity field which corresponds to the hollow rectangle (in the middle of the droplet) while the inset in the bottom corner shows the variation of the top point velocity.

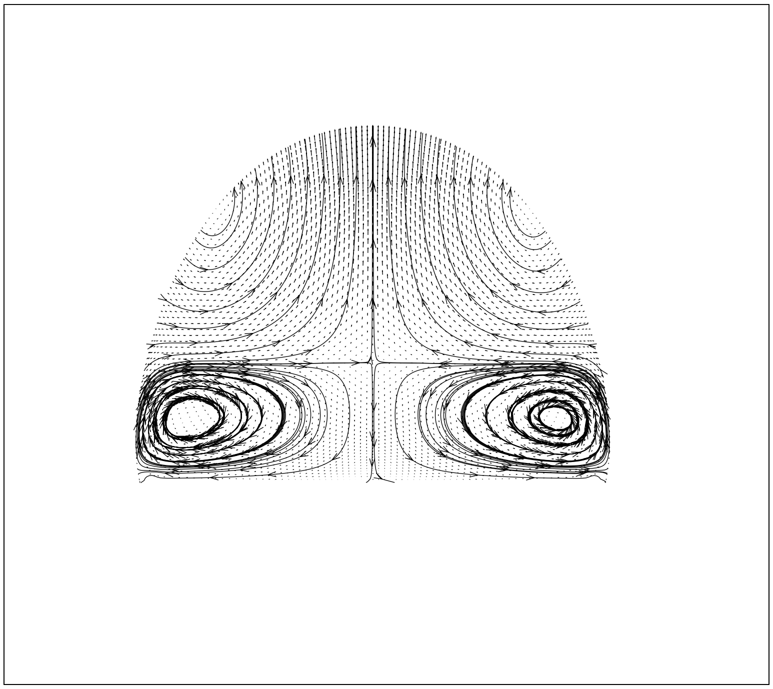

Figure 5.27: Recirculation pattern in the case of the crown, at an instant (t=4.1991) before droplet splashing; $Ca = 0.1$ & $Re = 30.0$.

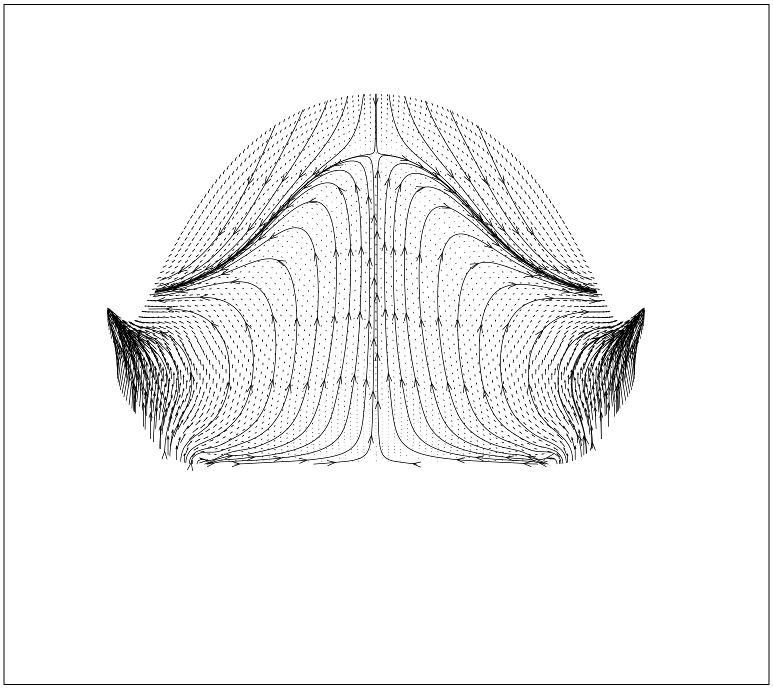

Figure 5.28: Streamtrace pattern for the crown at the instant of splashing (t=4.39631); $Ca = 0.1$ & $Re = 30.0$.

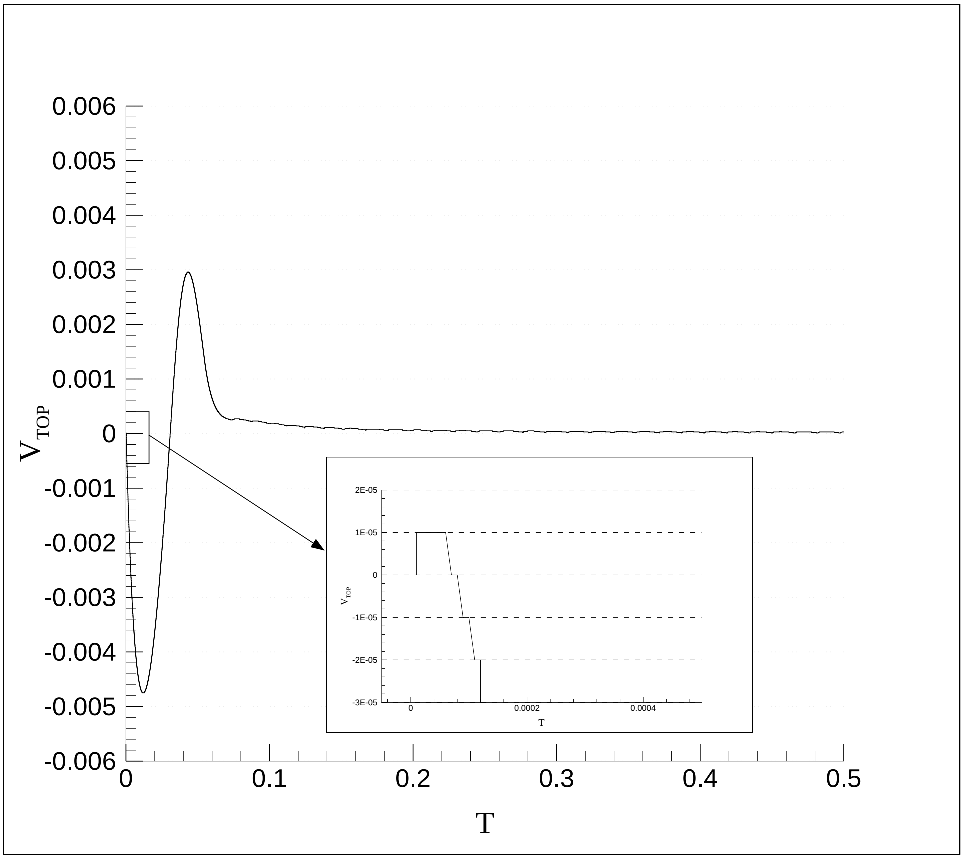

Figure 5.29: Behavior of the top point of a droplet spreading under reduced gravity conditions : $Ca = 0.1$ & $Re = 0.0005$.

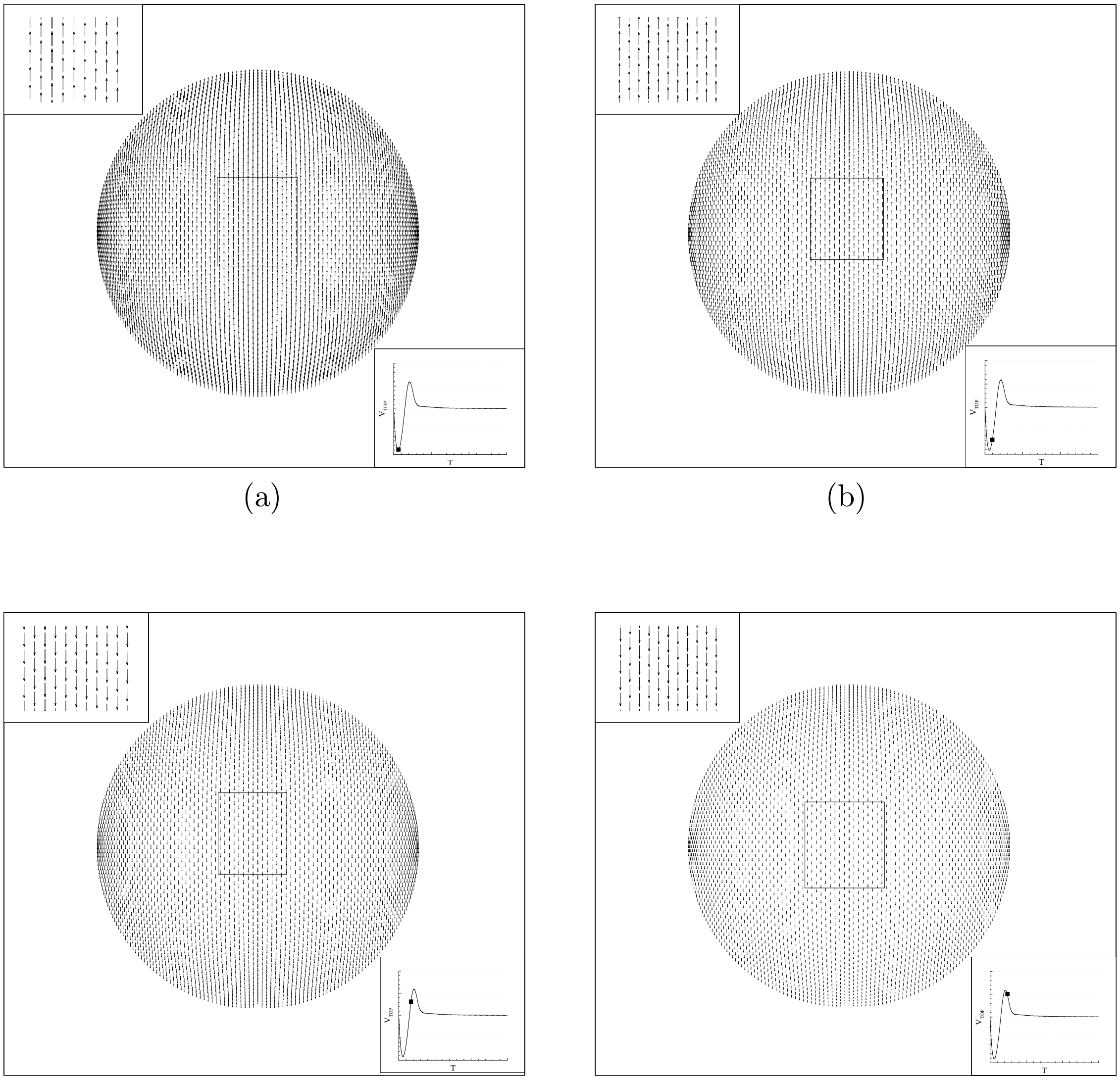

(a) (b)

(c) (d)

Figure 5.30: Typical behavior of a droplet spreading under reduced gravity conditions, with $Ca = 0.1$ & $Re = 0.0005$ at progressive instances of (non-dimensional) time : (a) t=0.01, (b) t=0.02, (c) t=0.04 and (d) t=0.05. The inset in the top corner shows an enlarged view of the velocity field which corresponds to the hollow rectangle (in the middle of the droplet) while the inset in the bottom corner shows the variation of the top point velocity.

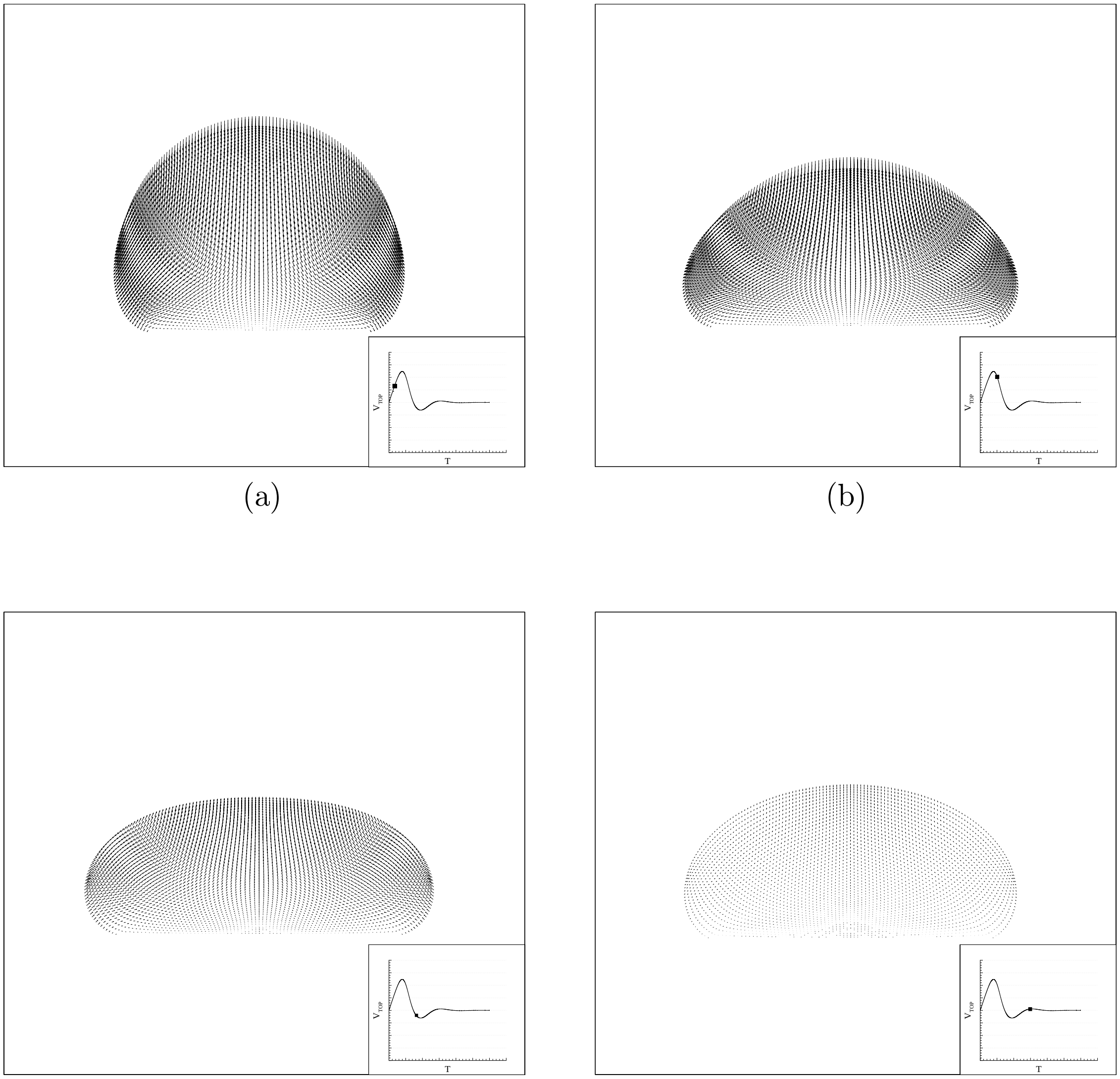

(a) (b)

(c) (d)

Figure 5.31: The spreading of the droplet in an oscillatory mode with a no-slip ($\beta = 0$) boundary condition at the contact point, with $Ca = 1.0$ & $Re = 5.0$, at progressive instances of (non-dimensional) time : (a) t=1.4, (b) t=2.0, (c) t=3.8 and (d) t=6.2. The inset in the bottom corner shows the variation of the top point velocity.

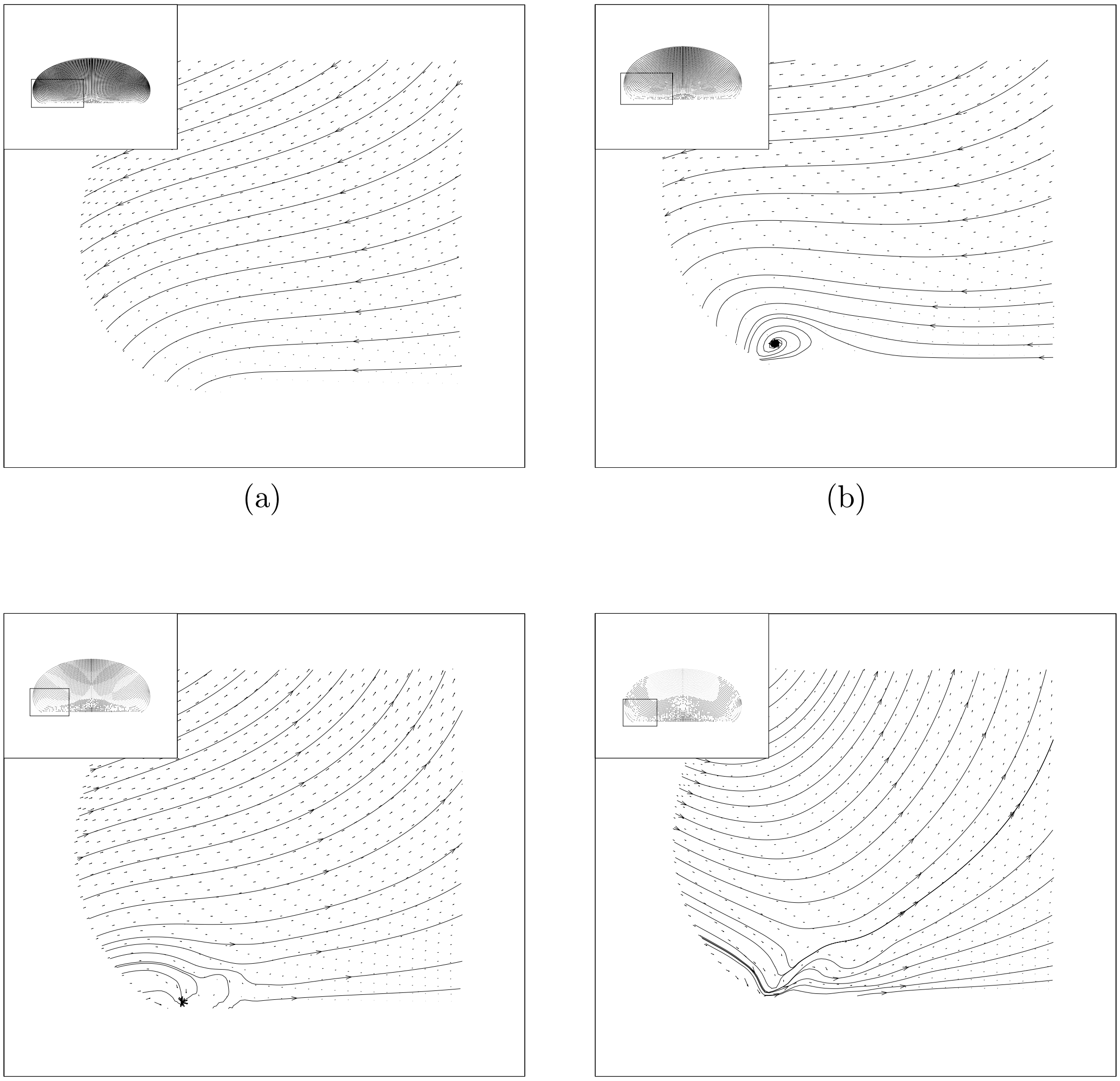

(a) (b) (c) (d)

Figure 5.32: The spreading of the droplet in an oscillatory mode with finite slip ($\beta = 0.1$) of the contact point, with $Ca = 1.0$, $Re = 5.0$ & $\theta_s = 160^\circ$, at progressive instances of (non-dimensional) time : (a) t=2.5, (b) t=7.5, (c) t=9.5 and (d) t=13.0.

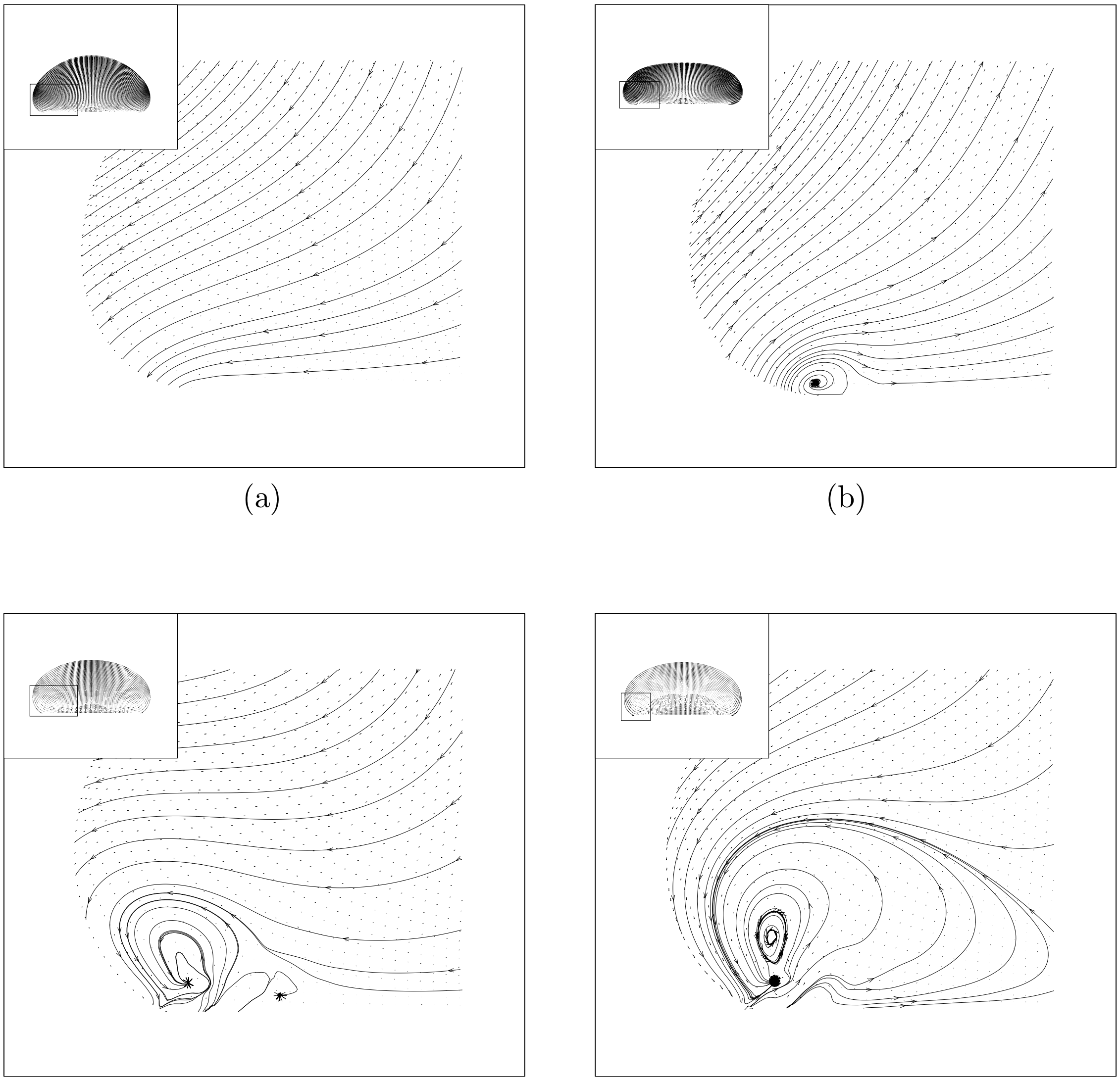

(a) (b)

(c) (d)

Figure 5.33: The spreading of the droplet in an oscillatory mode with finite slip ($\beta = 1.0$) of the contact point, with $Ca = 1.0$, $Re = 5.0$ & $\theta_s = 160°$, at progressive instances of (non-dimensional) time : (a) t=2.0, (b) t=3.0, (c) t=7.5 and (d) t=11.5.

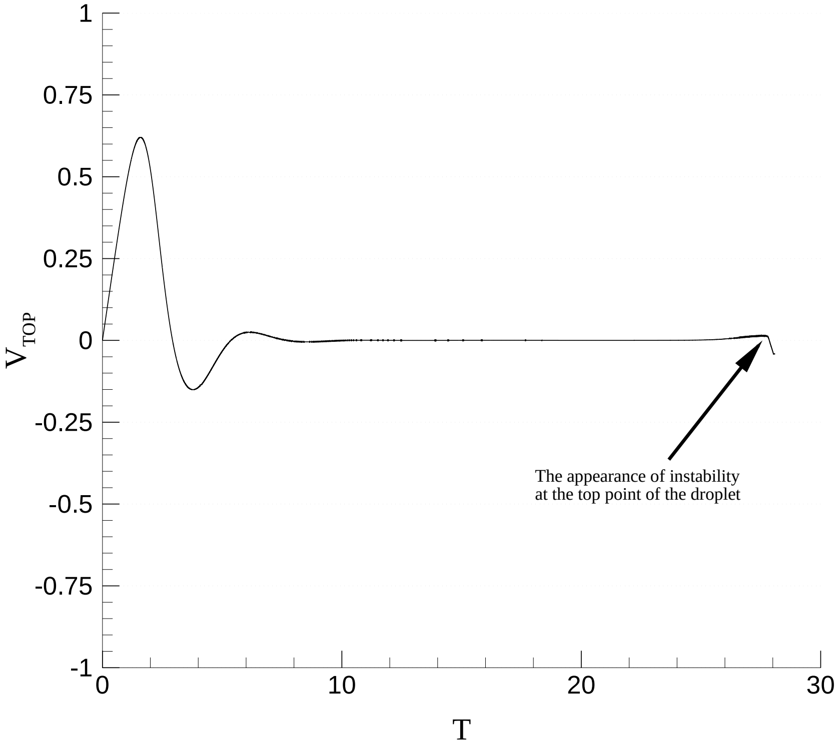

Figure 5.34: Variation of the velocity of the top point with time, for an oscillating droplet with $\beta = 1.0$: $Ca = 1.0$, $Re = 5.0$ & $\theta_s = 160°$.

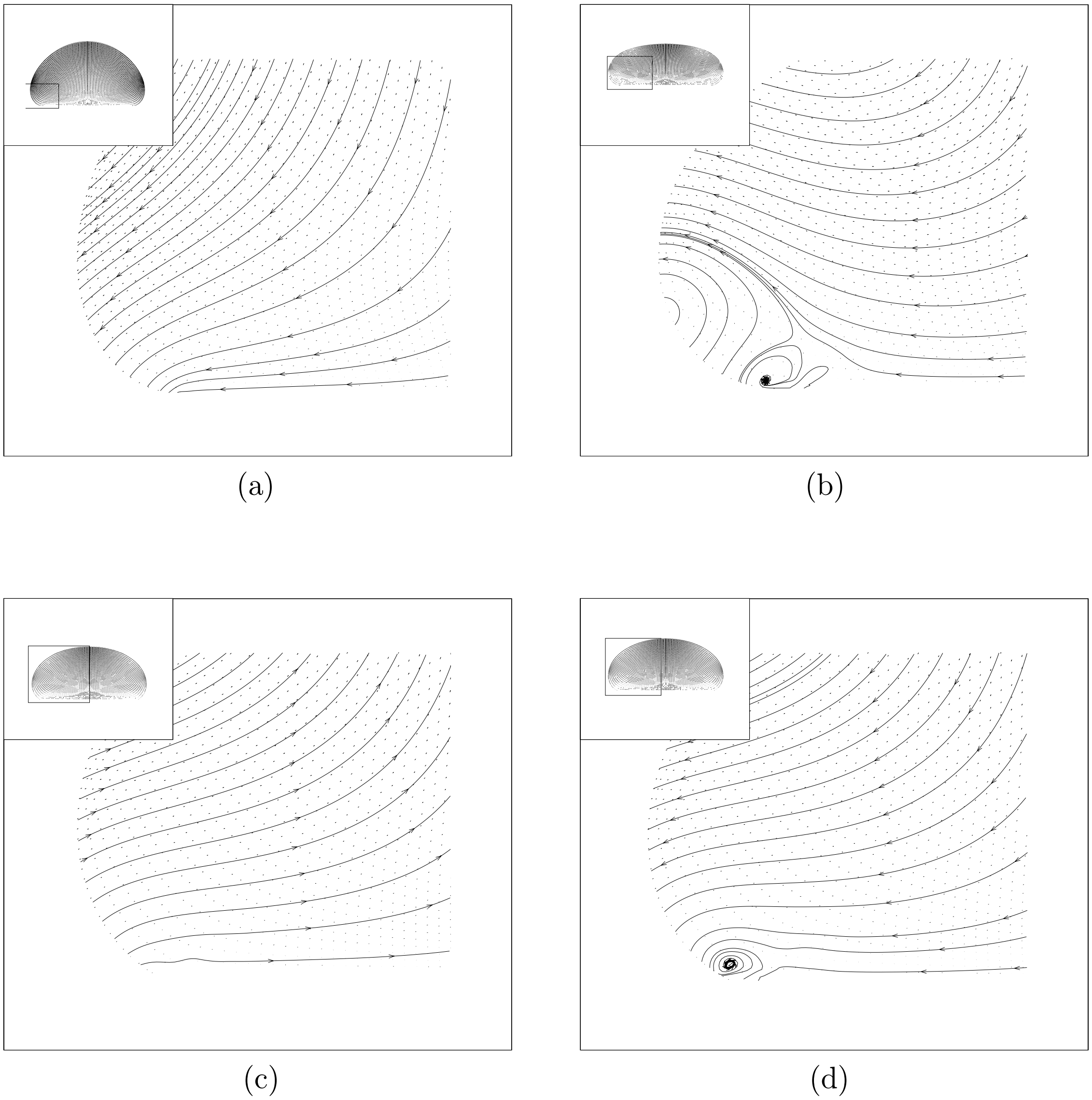
(a) (b) (c) (d)

Figure 5.35: The spreading of the droplet in an oscillatory mode with finite slip ($\beta = 0.5$) of the contact point, with $Ca = 1.0$, $Re = 5.0$ & $\theta_s = 160°$, at progressive instances of (non-dimensional) time : (a) t=3.5, (b) t=5.5, (c) t=9.5 and (d) t=14.5.

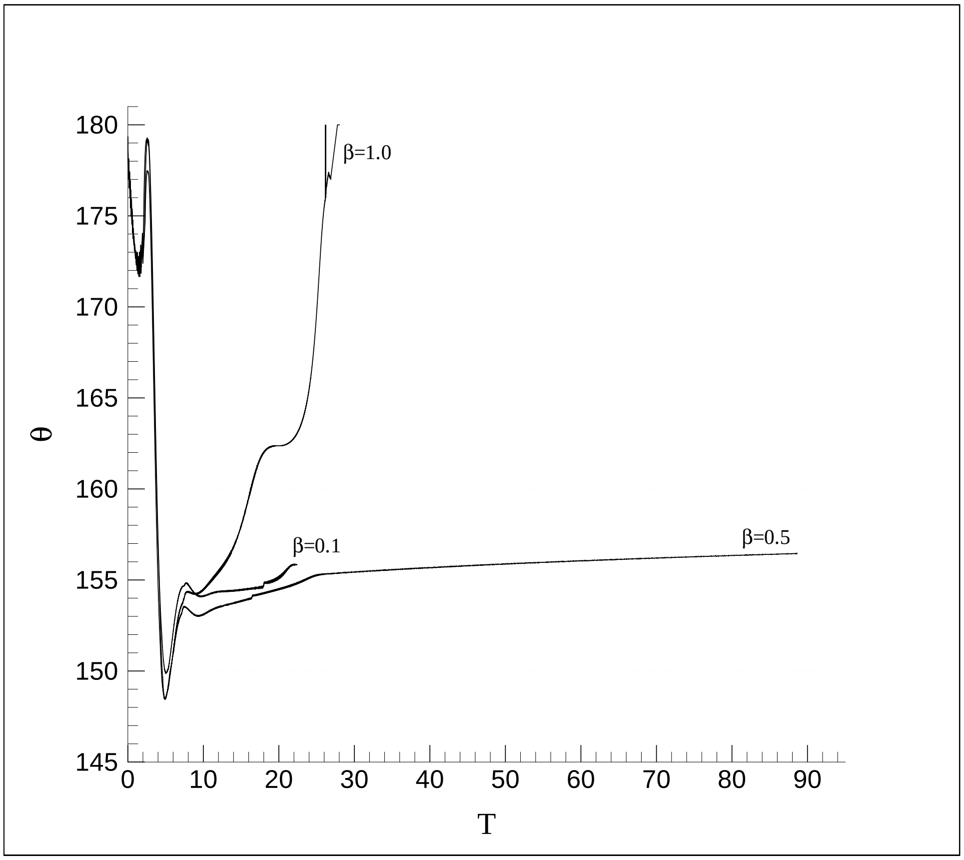

Figure 5.36: Variation of the dynamic contact angle, θ, with time, for an oscillating droplet with $\beta = 0.1$, $\beta = 1.0$ and $\beta = 0.5$, as indicated, with $Ca = 1.0$, $Re = 5.0$ & $\theta_s = 160°$.

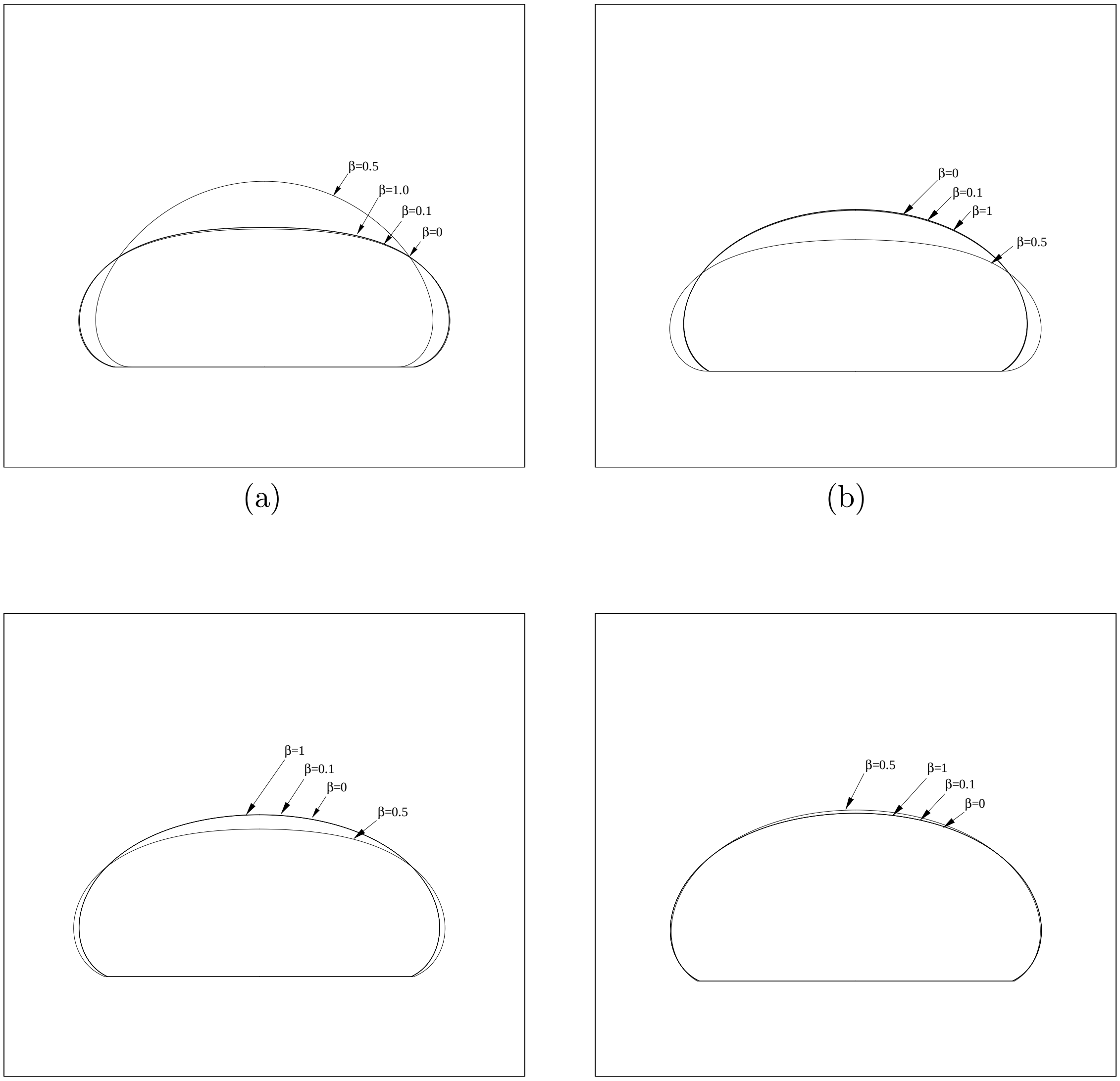

(a) (b) (c) (d)

Figure 5.37: Comparison of droplet shapes, for different values of β (0, 0.1, 0.5 & 1.0), for a droplet with $Ca = 1.0$ & $Re = 5.0$, at different (non-dimensional) times : (a) t=3.5, (b) t=5.5, (c) t=7.5 and (d) t=11.5.

Chapter 6

Conclusions and Recommendations for Future Work

The spreading of a viscous droplet on a plane solid surface is a very interesting study with many applications in the field of science and engineering. For example, several manufacturing processes require insight into the dynamics of such droplets to understand and possibly control the phenomenon to achieve difficult fabrication of miniature mechanical components. In addition to the physical advantages of the study, chemical, biological and surface-related characteristics can be better investigated and expressed. Experimental investigations of droplets can be difficult to perform at such small length scales. In such a situation, a valid computational model is invaluable in providing a convenient and inexpensive tool for the understanding and modeling of droplet behavior and useful related applications. The purpose of the present work was to develop such a versatile and helpful capability. The results that were obtained agree closely with physical observations and expected variations.

For instance, the three behaviors noticed here, for a droplet spreading on a solid surface were among those experimentally observed by Matson, Rolland and Flemings in 1998 [4] of an aluminium-copper alloy onto a thermally conditioned substrate. The distribution of the ranges of these behaviors is also comparable.

6.1 Conclusions

A discrete numerical model was created using an accurate and efficient Finite Element analysis, which aided the study of the phenomena of droplet spreading under different controlling conditions. Results were obtained for the cases of

- Spreading of two droplets after an initial, low inertia collision,
- Spreading of a droplet on a solid surface with no slip of the contact point,
- Spreading of a droplet on a solid surface with finite slip of the contact point.

In addition to the above external conditions, the resulting behavior of the droplet depended on the relative magnitudes of the gravity acting on the droplet, the viscosity of the fluid within and the surface tension holding the drop together. The spreading dynamics would presumably depend also on the temperature of the fluid and the solid surface and phase change, if any. The conclusions which can be drawn from the observations made in the previous chapter can be grouped based on the cases mentioned above.

Two droplet spreading :

- The study of the hypothetical case of two droplets spreading on each other with gravity forcing *both* towards the contact line, served in illustrating the effect of the physical quantities on the motion of the contact point. In this case, without the interference of an external surface, the contact point moves solely under the direct influence of viscosity and surface tension and the induced effect of gravity.

- In this situation, two distinct manners of spreading were observed : (a) stable and (b) unstable. In the former mode, the droplets oscillate, while retaining their near-spherical shape and eventually attain a stable state, close to equilibrium. In the latter mode, the spreading becomes unstable as the droplets undergo very high deformation and eventually disintegrate.
- The manner in which the droplet spreads depends on the relative strengths of surface tension, viscous and gravity forces acting on the droplet. These physical quantities have been quantified in terms of the capillary and Reynolds numbers. As the Reynolds number increases, or the capillary number decreases, the droplet gradually changes behavior from stable to unstable spreading. The profiles and velocity fields were observed and compared, and the results confirmed the expected trends.
- An important difference observed in the behavior of the droplet, in contrast to the spreading on a solid surface, is the motion of *all* points on the contact line. In the case discussed below, the only point that moves is the forward-most, or the contact point.

Droplet spreading on solid surface, with no slip :

- In this case, with the inclusion of the external solid surface, the dynamics of spreading are distinctly different. An interesting observation is a *third* manner of droplet spreading which was not observed in the case discussed above. The droplet spreads in one of the following three manners : (i) stable (ii) oscillatory and (iii) splashing. In the first manner, the droplet spreads towards the surface and quickly reaches equilibrium. In the second, the droplet oscillates for a while before gradually attaining a state of very slow motion (near-equilibrium). In the third mode, the droplet deforms much more than in the previous modes and eventually disintegrates, splashing on the solid surface.

- Like in the previous case, the behavior of the droplet depends on the capillary and Reynolds case. In the same way, as the Reynolds number increases, or the capillary number decreases, the droplet changes behavior from stable to oscillatory and then on to splashing. Here too, the trends of the velocity field of the fluid inside and the external profile agree closely with expectation.
- Due to the reversal in the direction of the velocity of the fluid in the droplet, recirculation is observed near the contact point, the intensity of which depends again, on the relative strengths of the forces acting on the droplet. In several cases, this recirculation relates to the disintegration or instability in the droplet.
- As an interesting case of the splashing behavior of the droplet, the classical crown formation was observed for a certain combination of Reynolds and capillary numbers. The recirculation in this case is very evident and the possible cause of splashing, as the fluid forces itself out the droplet side, briefly building the drop into the shape of a crown.
- A fourth mode of spreading is observed, in which, the effect of capillarity being stronger than gravity, the droplet rebounds from the solid surface and achieves higher velocities *away* from the surface. This case simulates the case of droplet spreading under microgravity conditions and is an interesting mode

of spreading, which can lead to very unusual trends in velocity and droplet shapes.

Droplet spreading on solid surface with finite slip :

- In this case, the contact point was assumed to slip on the solid surface, such that the slip velocity relates to the contact angle through a power law. It was observed that the amount of slip was very crucial for both the stability of the droplet and the rate at which it attains a constant static angle. The slip velocity was assumed to be quantified by an empirical, slip coefficient, β and some values were investigated.

- It was observed that the stability of droplet spreading was very sensitive to the value of the slip coefficient. While a value of $\beta = 0.1$ proved to be too small, causing very slow changes in the dynamics, $\beta = 1.0$ was so high that it adversely affected the stability of the droplet. An intermediate value of $\beta = 0.5$ appeared to be reasonable in terms of droplet stability and its attaining of the static contact angle. The exact value of this coefficient, however, needs to be determined experimentally and it is very likely that it depends on the fluid and surface properties of the solid.

6.2 Recommendations for Future Work

With advancing technology and ever progressing frontiers in the world of computation, expansion is always possible. Every piece of work has scope for improvement and advancement and this thesis is no exception. Even though the model was used for several cases of study, with very reasonable results, it can be made more versatile and useful in more ways. The following are some suggestions for future work :

- Investigation of a wider range of Reynolds and capillary numbers, can lead to discovery of interesting phenomena such as the droplet spreading under microgravity conditions. Also, the boundary between the different behaviors can be established more precisely.

- Similarly, a more extensive study of the effect of varying slip coefficient will prove useful in quantifying the slip velocity of the contact point. Possible experimentation can help in proving or refuting assumptions and giving us an insight into the manner of slipping of the contact point.

- As mentioned before, this study was made for isothermal droplet spreading. Investigation of the dynamics of spreading with varying temperatures and possible phase changes will definitely lead to a more comprehensive and complete study of the phenomenon.

- A faster solver or solution algorithm, if applied, would help make verification and comparison against existing data more efficient.

Bibliography

[1] P. G. de Gennes. Wetting : statics and dynamics. *Reviews of Modern Physics*, 57(3, part 1):827–863, July 1985.

[2] P. J. Haley and M. J. Miksis. The effect of the contact line on droplet spreading. *Journal of Fluid Mechanics*, 223:57–81, 1991.

[3] C. Huh and L. E. Scriven. Hydrodynamic model of steady movement of a solid/liquid/fluid contact line. *Journal of Colloid and Interface Science*, 35(1):57–81, January 1971.

[4] M. Rolland D. M. Matson and M. C. Flemings. Impingement behavior of a spray cast aluminum alloy. *TMS Annual Meeting, San Antonio, TX*, February 1998.

[5] D. Poulikakos J. Fukai, Z. Zhao et al. Modeling of the deformation of a liquid droplet impinging upon a flat surface. *Physics of Fluids*, 5(11):2588–2599, November 1993.

[6] H. Lamb. On the oscillations of a viscous spheroid. *Proceedings of the London Mathematical Soceity*, 13:51–66, 1881.

[7] G. Trapaga and J. Szekely. Mathematical modeling of the isothermal impingement of liquid droplets in spray processes. *Metallurgical Transactions B*, 22B:901–913, 1991.

[8] J.J. Valencia G. Trapaga, E. F. Matthys and J. Szekely. Fluid flow, heat transfer and solidification of molten metal droplets impinging on substrates : comparison of numerical and experimental results. *Metallurgical Transactions B*, 23B:701–717, 1992.

[9] G. Trapaga R. Westhoff and J. Szekely. Plasma-particle interactions in plasma spraying systems. *Metallurgical Transactions B*, 23B:683–693, 1992.

[10] Z. Zhao J. Fukai, D. Poulikakos et al. Wetting effects on the spreading of a liquid droplet colliding with a flat surface : Experiment and modeling. *Physics of Fluids*, 7(2):236–247, February 1995.

[11] L. M. Hocking and A. D. Rivers. The spreading of a drop by capillary action. *Journal of Fluid Mechanics*, 121:425–442, 1982.

[12] H. P. Greenspan. On the motion of a small viscous droplet that wets a surface. *Journal of Fluid Mechanics*, 84, part 1:125–143, 1978.

[13] E. B. Dussan and S. H. Davis. On the motion of a fluid-fluid interface along a solid surface. *Journal of Fluid Mechanics*, 65, part 1:71–95, 1974.

[14] P. Ehrhard and S. H. Davis. Non-isothermal spreading of liquid drops on horizontal plates. *Journal of Fluid Mechanics*, 229:365–388, 1991.

[15] L. M. Hocking. Rival contact-angle models and the spreading of drops. *Journal of Fluid Mechanics*, 239:671–681, 1992.

[16] S. Chandrasekhar. The oscillations of a viscous liquid globe. *Proceedings of the London Mathematical Soceity*, 9:141–149, 1959.

[17] K. N. Christodoulou and L. E. Scriven. Discretization of free surface flows and other moving boundary problems. *Journal of Computational Physics*, 99:39–55, 1992.

[18] N. Mourougou-Candoni, B. Prunet-Foch amd F. Legay, M. Vignes-Adler, and K. Wong. Influence of dynamic surface tension on the spreading of surfactant solution droplets impacting onto a low-surface-energy solid substrate. *Journal of Colloid and Interface Science*, 192:129–141, 1997.

[19] M. Vignes-Adler B. Prunet-Foch, F.Legay and C. Delmotte. Impacting emulsion drop on a steel place : influence of the solid substrate. *Journal of Colloid and Interface Science*, 199:151–168, 1998.

[20] J. Han and G. Tryggvason. Secondary breakup of axisymmetric liquid drops. I. Acceleration by a constant body force. *Physics of Fluids*, 11(12):3650–3667, December 1999.

[21] N. G. Hadjicostantinou. Combining atomistic and continuum simulations of contact-line motion. *Physical Review*, 59(2):2475–2478, February 1999.

[22] Y. Wu and E. J. Lavernia. Interaction mechanisms between ceramic particles and atomized metallic droplets. *Metallurgical Transactions*, 23A:2923–2937, October 1992.

[23] A. Prosperetti and H. N. Oguz. The impact of drops on liquid surfaces and the underwater noise of rain. *Annual Review of Fluid Mechanics*, 25:577–602, 1993.

[24] S. Schiaffino and A. A. Sonin. Formation and stability of liquid and molten beads on a solid surface. *Journal of Fluid Mechanics*, 343:95–110, 1997.

[25] F. Gao and A. A. Sonin. Precise deposition of molten microdrops : the physics of digital microfabrication. *Proceedings of the Royal soceity of London*, 444:533–554, 1994.

[26] J. Eggers. Nonlinear dynamics and breakup of free-surface flows. *Reviews of Modern Physics*, 69(3):865–929, July 1997.

[27] S. W. Sloan. A FORTRAN program for profile and wavefront reduction. *International Journal for Numerical Methods in Engineering*, 28:2651–2679, 1980.

[28] S. W. Sloan. A fast algorithm for constructing Delaunay triangulations in the plane. *Advances in Engineering Software*, 9(1):34–55, 1987.

[29] B. Ramaswamy. Numerical simulation of unsteady viscous free surface flow. *Journal of Computational Physics*, 90:396–430, 1990.

[30] A. Ahmed and A. N. Alexandrou. Processing of semi-solid materials using a shear-thickening Bingham fluid model. *Proceedings of the 1994 ASME Fluids Engineering Division Summer Meeting, ASME, New York, FED*, 179:83–87, 1994.

[31] H. E. Edgerton. *Stopping time : The Photographs of Harold Edgerton.* Harry N. Abrams, Iincorporated, New York, 1987.